4D FLOW DURING PREGNANCY AND AFTER PRETERM BIRTH

by

Jacob A. Macdonald

A dissertation submitted in partial fulfillment of

the requirements for the degree of

Doctor of Philosophy

(Medical Physics)

at the

UNIVERSITY OF WISCONSIN-MADISON

2018

Date of the final oral examination: 08/14/2018

The dissertation is approved by the following members of the Final Oral Committee:

Oliver Wieben, Associate Professor, Medical Physics
Sean B. Fain, Professor, Medical Physics
Kevin M. Johnson, Assistant Professor, Medical Physics
Christopher J. Francois, Associate Professor, Radiology
William G. Schrage, Professor, Kinesiology

© Copyright by Jacob A. Macdonald 2018

All Rights Reserved

4D FLOW DURING PREGNANCY AND AFTER PRETERM BIRTH

Jacob A. Macdonald

Under the supervision of Associate Professor Oliver Wieben

At the University of Wisconsin-Madison

Abstract

4D flow MRI is a powerful imaging technique that allows for the quantification and visualization of blood flow in a three-dimensional vector space over time. With accelerated acquisitions, 4D flow MRI can be performed over large imaging volumes with sub-millimeter resolution in clinically feasible scan times. Such accurate characterization of blood flow patterns is not possible *in vivo* with other imaging modalities. As a result of the utility of these sequences, the last decade has seen the widespread adoption of 4D flow MRI in research settings and increased utility in clinical roles. Typical applications of 4D flow MRI include cardiac, cranial, renal, and hepatic disease. In these anatomical regions, physiologic motion is predictable and well-characterized and vessels-of-interest are typically large relative to the sequence spatial resolution, allowing for quantification of complex flow dynamics.

While 4D flow MRI has proven its value in these settings, there are a variety of previously unexplored applications in which it could represent marked improvement over current clinical techniques. The aim of this dissertation was the development of innovative 4D flow MRI methodology to pioneer comprehensive *in vivo* hemodynamic assessment in two challenging applications: (1) maternal and fetal 4D flow imaging during pregnancy and (2) exercise cardiovascular MR (CMR) with 4D flow imaging during strenuous exercise challenges in preterm adolescents and young adults.

Many pregnancy complications are associated with vascular maladaptation to pregnancy, and thus, the ability to quantify flow in the uteroplacental and fetal vasculature during pregnancy could be a powerful tool for identifying complications in at-risk populations before outward symptoms manifest. Doppler

ultrasound is used clinically for this role but has poor sensitivity early in gestation. The feasibility of 4D flow measurements is demonstrated in a rhesus macaque model, paving the way for future feasibility studies in human subjects.

With regards to the second application, the ability to quantify complex cardiac flow during exercise with MRI is of special interest when studying child and young adult populations with suspected cardiac abnormalities. Exercise challenges are routinely used with ultrasound to elucidate differences in physiological responses between normal subjects and those with pathologies which might be difficult to differentiate at resting conditions. However, exercise studies in the MR bore are challenging and rarely performed. The viability of 4D flow quantification during exercise in adolescents and young adults is demonstrated in this dissertation, including the methodology developments on the unique hardware and software required to overcome challenges associated with exercise CMR. The value of 4D flow exercise CMR is then shown in a small cohort of adolescent and adult subjects born prematurely, a population that may be at an increased risk for cardiovascular disease later in life.

Overall, the techniques implemented in this dissertation offer enhanced capabilities to quantify and characterize the impact of irregular pregnancies on flow over the current clinical standard of Doppler ultrasound, both *in utero* and later in life. These techniques may translate to improved diagnostic and prognostic potential throughout life in affected subjects.

Acknowledgements

The work presented in this dissertation would not have been possible without the support from an extensive group of colleagues, family, and friends.

First of all, I would like to thank my advisor, Dr. Oliver Wieben. When I was performing my interviews for graduate school, I knew I wanted to pursue MRI research but was certain of very little beyond that. When I finally interviewed with Oliver, like so many before me, I was immediately entranced by the beautiful 4D flow images he showed me that he and his group had created. His research felt like a perfect fit for me, as it combined my interest in MRI with fluid dynamics – one of my favorite course subjects in my undergraduate education, and his excitement on the work was infectious. He was gracious enough to invite me to join his group, despite the fact that I was dealing with an unfortunate bout of food poisoning during my interview, and the rest is history. He has been a fantastic mentor throughout the years, giving me guidance and establishing critical collaborations for my work within the hospital, while also allowing me the freedom to take the research in directions I found interesting. His knowledge of phase contrast MRI is second-to-none, and he was always ready with his door open to share it with me to overcome particularly tricky challenges. Without his mentorship, I would surely be a fraction of the researcher I am today.

I would also like to thank my parents, Jane and George Macdonald. They have now selflessly supported me throughout nearly a decade of post-secondary education, and never once questioned if I was going to ever stop going to school and get a real job. They were always the people most interested in the work I was performing, asking for weekly updates, even though I am sure they rarely understood most of what I was talking about. They were always willing to come for a weekend visit to Madison, whether it was to see a Badgers football game or go hiking at Devil's Lake. Their unending support through these last few years means the world to me.

I could not have achieved any of this without the support of my amazing wife, Erin. She has been my constant companion in both MRI research and life since our undergraduate education. She has always been available to talk through a research problem, eat lunch together, or go for a walk together to de-stress

throughout this whole process. She has been the best traveling companion I could hope for to many ISMRM conferences (and post-conference travel) in locations such as Singapore, Hawaii, and Paris. Outside of work, I have enjoyed the opportunity to experience Wisconsin (and became Green Bay Packers fans in the process) with her. Regardless of where life takes us in the future, Madison will always hold a special place in our hearts, as we were fortunate enough to get married here during our education.

Thank you to all the friends I have made along the way, whether they were members of our intramural soccer team, the MRI softball team, or our beer-league volleyball team. Participating on those teams was always a highlight of the summer and fall every year (even if it took a few years to get that first win in softball). A special thank you to Kai Ludwig and David Mummy, who began their graduate education in MRI alongside Erin and me. It was a true pleasure to move through the experiences of graduate school alongside you guys. I will always fondly remember those nights of drinking Wayne Gretzky's finest and playing Love Letter in Toronto.

I would also like to thank my lab mates, past and present, for everything they have contributed to this work. I would like to acknowledge the past members of the flow groups, Ashley Anderson, Mike Loecher, and Eric Schrauben, for their willingness to show me the ropes and answer any stupid questions I may have had about the basics of MRI. I am also appreciative to all current members of the lab, Leonardo Rivera-Rivera, Carson Hoffman, Phil Corrado, Grant Roberts, and Dan Seiter. Thank you for lending me a hand with projects whenever I asked, never complaining when I unceremoniously dumped dozens of PC VIPR cases on your desk for analysis, and always being available for a conversation about whatever sports team played last night. A special thanks to Carson for all of his food that I ate over the years.

Finally, thank you to everyone else who has contributed to this work in any way, big or small. This work was possible only because of such contributions and support, and I am truly grateful for everything.

Table of Contents

List of Tables

List of Figures

Chapter 1: Introduction

Magnetic resonance imaging (MRI) is a powerful modality for diagnostic medical imaging. Through exploitation of the magnetic moments inherent to hydrogen atoms abundant in the human body, MR images are capable of showing exquisite contrast between soft tissues, a feat not possible with other imaging modalities, such as computed tomography (CT), ultrasound (US), or positron emission tomography (PET). In addition to standard anatomical images, MRI is capable of quantifying valuable information on physiology and function, such as diffusion and perfusion [1], mechanical stiffness [2], and blood flow [3]. As a result of these capabilities, improved hardware performance, and growing concerns about repeatedly exposing patients to ionizing radiation, a fundamental trait of CT and PET examinations, MRI has experienced rapid adoption for both clinical and research purposes over the last few decades. However, continuing challenges for widespread use of MRI have included high cost relative to other imaging modalities, relatively long scan times resulting in increased sensitivity to patient motion, and decreased patient comfort due to the claustrophobic scanner bore.

Blood flow quantification with phase contrast (PC) MRI is one quantitative technique, in particular, that has proven to have a valuable role in clinical settings. The ability to characterize total blood flow to and from an organ can be one of the most fundamental indicators of organ health. Traditionally, Doppler US has been used to estimate blood flow during pregnancy and for a variety of conditions including blood clots, arterial occlusions, and congenital heart disease [4], but there are a few limitations with this modality. Doppler US can be highly user-dependent, is prone to inaccuracies when probing deeper anatomy or intracranial vessels due to signal attenuation, and estimates flow by fitting average velocity to pre-established flow models, which can introduce systemic errors into measurements. PC MRI, however, is not susceptible to these shortcomings and has been well-validated against clinical gold-standard metrics for flow. The most common implementation of PC MRI in the clinic is a two-dimensional (2D) PC cine acquisition, where a 2D scan plane is aligned orthogonal to the vessel of interest and only the through-plane velocity components are measured throughout the cardiac cycle with an ECG gated acquisition over

multiple heartbeats. This allows for accurate quantification of blood flow in vessels with laminar flow, where the flow only has a single prominent component.

4D flow MRI [5] is an extension of 2D PC MRI that simultaneously encodes velocity in all three spatial dimensions via a volumetric acquisition with sub-millimeter spatial resolution. This allows for the quantification and characterization of more complex flow fields, such as those encountered in the ventricles or vessels with tortuous paths. The time-resolved velocity information can also be used to derive hemodynamic parameters such as kinetic energy, wall shear stress, and pressure gradients [6]. Due to the wide range of hemodynamic information that can be derived from a single scan, 4D flow techniques have become more prominent in investigational studies and are becoming available as product sequences through major MRI vendors. These sequences are now well-established for cardiac, cranial, and hepatic imaging, regions of the body that feature predictable motion and vessels significantly larger than the sequence spatial resolution. The viability of these sequences, however, remains challenging and not fully understood in the presence of motion that cannot be adequately characterized by cardiac or respiratory gating or for smaller vessels on the order of the sequence spatial resolution.

The aim of the work presented in this dissertation was the development of innovative 4D flow MRI methodology to facilitate hemodynamic assessments during early-life development. Two specific applications were investigated which presented both different clinical value and technical challenges. First, the feasibility of using 4D flow MRI during pregnancy to quantify total uteroplacental blood flow and fetal blood flow was assessed. Imaging during pregnancy is challenging given the very small diameters of the vessels-of-interest and unpredictable fetal movement that cannot be accurately modeled. The 4D flow technique described within overcame prior barriers precluding reliable flow quantification in these vessels with MRI. This work included a repeatability analysis for flow measurements in the maternal uteroplacental vessels, comparisons of PC angiograms to contrast-enhanced angiograms, and feasibility of quantifying fetal blood flow. The second focus of this dissertation was the development of first-of-its-kind cardiac 4D flow imaging during exercise for examinations in preterm adolescents and young adults. Exercise imaging is particularly challenging with MRI due to the drastically increased subject motion and reduced reliability

in gating. This work included testing the viability of pre-existing product pulse sequences following exercise, implementing a high-power MR-compatible exercise device never before used on GE hardware, designing novel post-processing algorithms to improve gating robustness, and validating 4D flow MRI during exercise in control and preterm populations. Overall, this dissertation sought to implement 4D flow MRI as a valuable tool for assessing the impacts of irregular pregnancy through different stages of life. The remaining chapters of this dissertation are organized as follows:

Chapter 2: Principles of Phase Contrast MRI provides a brief overview on the underlying physics of phase contrast MRI techniques, which can be used to quantify blood flow *in vivo*. This chapter begins with coverage of basic MR physics and techniques, including signal formation, measurement, and reconstruction. Further detail is provided on physical principles unique to motion sensitive phase contrast MRI, including the utilization of bipolar gradients. The fundamentals of 4D flow MRI, a 3D, time-resolved implementation of PC MRI, are discussed. Finally, there is a short review on alternative clinical techniques for flow quantification and their application to subject populations relevant to this thesis.

Chapter 3: Feasibility of 4D Flow MRI during Pregnancy explores the feasibility of using 4D flow MRI to quantify total uteroplacental flow to the placenta in healthy, pregnant rhesus macaque monkeys. Test-retest, inter-observer, and intra-observer variability was quantified for all flow measurements. Reference high-resolution, ferumoxytol-enhanced angiograms were acquired to assess the vessel conspicuity in the PC angiograms derived from the 4D flow data. Feasibility of quantifying flow in the umbilical cord and fetus was assessed as well. The material in this chapter was presented in poster presentations at IFPA 2016 [7], SRI 2017 [8], and ISMRM 2017 [9,10], an oral presentation at SMRA 2016 [11], and has been accepted for publication in the Journal of Magnetic Resonance Imaging [12].

Chapter 4: Initial Experience with MRI Exercise Studies reviews initial attempts at MRI exercise imaging with existing equipment and pulse sequences. Patients with pulmonary hypertension are one group that could benefit from enhanced diagnostic and prognostic capabilities with exercise imaging. In a small cohort of these subjects and comparable healthy controls, exercise was performed in the MRI scanner bore with a custom-made, MR-compatible stepper designed and constructed in the engineering department.

Cardiac imaging was performed immediately following exercise with standard 2D PC and balanced steady-state free precession (bSSFP) product sequences. The suitability of this equipment and these pulse sequences for exercise CMR was assessed. The material in this chapter was presented in a poster presentation at ISMRM 2015 [13], oral presentations at SCMR 2015 [14] and ISMRM 2016 [15], and is currently under consideration for publication.

Chapter 5: Implementation of High Power MR-compatible Exercise Equipment covers the work performed to allow a commercial MR-compatible stepper to be reliably used for high-power exercise challenges in our institution's scanners. This involved redesign of the stepper base, improvements to the calibration software, and hardware modifications to allow for more accurate measurements of achieved exercise power.

Chapter 6: Feasibility of 4D Flow MRI during Exercise presents results from a study examining the feasibility of 4D flow MRI during high-power exercise challenges with the commercial exercise stepper discussed in Chapter 5. Flow was measured in the aorta and main pulmonary artery, while kinetic energy was assessed in both the right and left ventricles. Feasibility was assessed in both young adults and adolescents. A novel algorithm to correct gating tracks corrupted by exercise motion is presented. The material in this chapter was presented in poster presentations at SCMR 2017 [16] and ISMRM 2018 [17] and is currently under consideration for publication.

Chapter 7: Exercise CMR in Preterm Children and Adults extends the 4D flow MRI techniques implemented and validated in Chapter 6 to a subject population born prematurely. This population has an increased risk for long-term cardiac dysfunction but the mechanisms for such are not well understood. Alongside the standard flow analysis described above, a thorough quantitative and qualitative assessment of diastolic filling is performed. The material in this chapter was presented in oral presentations at ISMRM 2017 [18] and 2018 [19].

Chapter 8: Summary and Recommendations reviews the novel research presented in this dissertation. Recommendations for future work are provided to continue building on the foundations laid herein for innovative 4D flow MRI exams during pregnancy and exercise.

Chapter 2: Principles of Phase Contrast MRI

This chapter introduces the basic physical principles of MRI and phase contrast MRI. The background presented here is not meant to be an exhaustive treatment of the subject, but simply an introduction into the physics principles that guided the work in this dissertation. Readers interested in a more comprehensive treatment are directed towards the following references [20–23].

2.1 Magnetic Resonance Imaging Principles

2.1.1 Spin and Magnetization

All atoms can be characterized by an inherent property known as spin, a form of angular momentum encountered in quantum mechanics. Charged particles with non-zero spin will generate a magnetic dipole moment. Such magnetic moments are extraordinarily widespread in the human body, as hydrogen atoms (single protons with ½ spin) are abundant in biological tissue such as muscle, fat, and blood. MRI fundamentally relies on the excitation and relaxation of hydrogen atoms in these tissues to produce the measurable signals used to generate images. Henceforth, the word "spin" will be used interchangeably to refer to the behavior of the single proton in hydrogen atoms in the body. While the complex particle interactions inherent to MRI can be most completely explained through a quantum mechanical treatment of the subject [24], a classical treatment is sufficient to understand most basic MR principles. Thus, the remainder of this chapter will focus on the classical approach.

When a spin is placed in the static magnetic field found in an MRI scanner, commonly referred to as the $\boldsymbol{B_0}$ field, its magnetic moment will precess around the main magnetic field at a frequency known as the Larmor frequency

$$\boldsymbol{\omega} = \gamma \boldsymbol{B_0} \qquad \textit{Eq. 2-1}$$

where $\boldsymbol{\omega}$ is the Larmor frequency, also referred to as the precession frequency, γ is the gyromagnetic ratio (42.6 MHz/T for hydrogen), and $\boldsymbol{B_0}$ is the magnetic field strength (typically 1.5 or 3.0 T for most current clinical scanners). Spins placed in a static magnetic field will also experience Zeeman splitting of energy levels, resulting in two distinct energy states in the case of hydrogen. These can be approximated as the

magnetic moments aligned with the magnetic field (low energy state) or anti-aligned with the field (high energy state) and are colloquially referred to as spin-up and spin-down states, respectively. The distribution of spins between these two energy states is described by the Boltzmann distribution

$$\frac{N_{up}}{N_{down}} = e^{-\frac{\Delta E}{kT}} \qquad \textit{Eq. 2-2}$$

where N_{up} and N_{down} are the number of spins in the spin-up and spin-down states respectively, ΔE is the difference in energy between the two states, k is the Boltzmann constant (1.381 x 10^{-23} J/K), and T is the temperature. At room temperature and typical MRI field strengths, the spin excess for the spin-up state is only a few spins per million. MRI, however, benefits from the massive amount of hydrogen atoms present in the human body, allowing for a measurable net magnetization vector aligned with the main magnetic field of the scanner. Hereon, this review will describe the effects of MRI imaging on this net magnetization vector, rather than the individual spins that compose this vector.

2.1.2 Excitation, Relaxation, and Decay

If a second magnetic field, often referred to as the $\boldsymbol{B_1}$ field, is temporarily applied orthogonal to the $\boldsymbol{B_0}$ field and net magnetization vector, the equilibrium described by the Boltzmann distribution will be perturbed as many spins are excited to the higher energy state. This is achieved by a radiofrequency (RF) pulse. In a classical treatment, this is represented by the net magnetization being "tipped" down from the longitudinal plane (parallel to $\boldsymbol{B_0}$) towards the transverse plane. As this magnetization continues to precess around the $\boldsymbol{B_0}$ field at the Larmor frequency as it is tipped, the trajectory of the magnetization can be imagined as a spiral down to the transverse plane, as shown in Figure 2-1a. For simplicity, MRI physics often instead deals with a rotating reference frame at the Larmor frequency [25]. As shown in Figure 2-1b, with this treatment, the magnetization can be imagined as tipping directly into the transverse plane. This behavior is described by the rotating frame Bloch equation, where $\boldsymbol{M}$ is the net magnetization vector:

$$\frac{d\boldsymbol{M}}{dt} = \boldsymbol{M} \times \gamma \boldsymbol{B_1} \qquad \textit{Eq. 2-3}$$

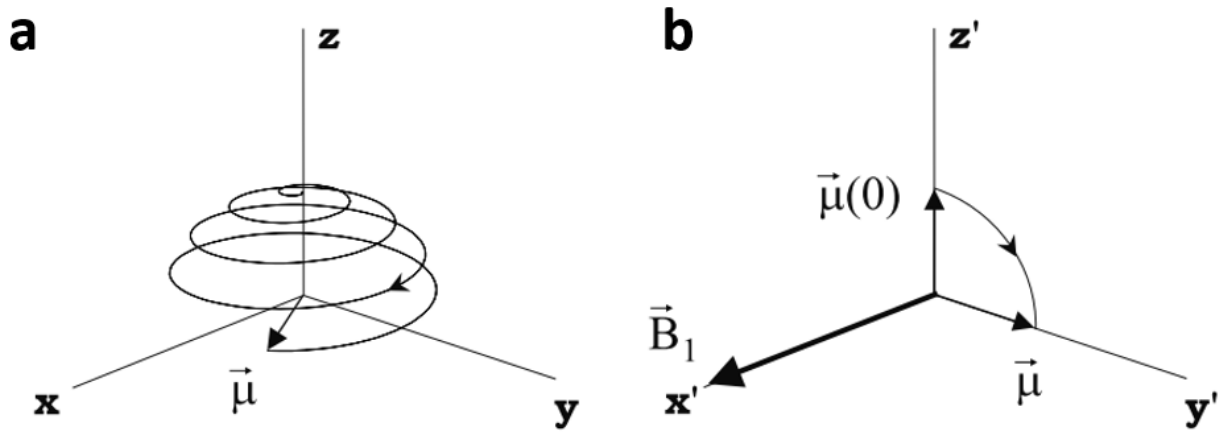

Figure 2-1: (a) Net magnetization vector behavior when excited by an orthogonal magnetic field on the x axis. The magnetization is tipped towards the transverse plane while still precessing around the $\boldsymbol{B_0}$ *field, resulting in the spiral trajectory shown. (b) When a rotating reference frame at the Larmor frequency is used, the magnetization can be imagined as tipping directly into the transverse plane. Image courtesy of Haacke et al* [20].

For the remainder of this section, a rotating reference frame at the Larmor frequency of hydrogen will be assumed.

Immediately following the end of the $\boldsymbol{B_1}$ field application, this excited state will recover towards thermal equilibrium in a process known as T_1 or spin-lattice relaxation. The regrowth of the longitudinal magnetization, M_z, is described by the following equation [25]:

$$M_z(t) = M_0\left(1 - e^{-\frac{t}{T_1}}\right) \qquad \textit{Eq. 2-4}$$

where M_0 is the original longitudinal magnetization magnitude, t is the time following excitation, and T_1 is a tissue-dependent time constant describing the time required for 63% of the excited magnetization to be recover to the longitudinal plane. Sample magnetization recovery curves for tissues with short T_1 and long T_1 are shown in in Figure 2-2a, alongside depictions of the longitudinal magnetization recovery.

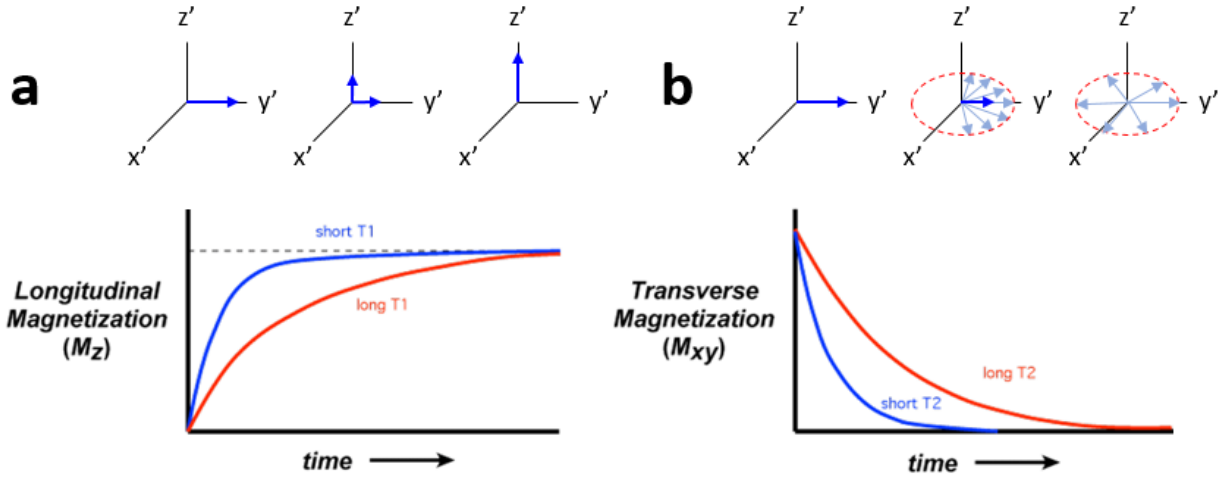

Figure 2-2: (a) Longitudinal magnetization recovery curves for tissues with short T_1 and long T_1. Shown above the curves is a simplified depiction of excited transverse magnetization transitioning back to longitudinal magnetization. (b) Transverse magnetization decay for tissues with short T_2 and long T_2. The loss of spin coherence resulting in decreased bulk magnetization is depicted above the curves. Magnetization curves courtesy of Allen Elster [23].

Alongside regrowth of the longitudinal magnetization, there is additional decay of the transverse magnetization vector magnitude, M_{xy}, from what is known as T_2 or spin-spin decay. This signal decay occurs when the excited spins do not have the same precession frequency due to different chemical compositions, atomic environments, or other factors. As a result, spin coherence is lost over time as some spins rotate faster or slower relative to the Larmor frequency, and the net magnetization vector in the transverse vector shrinks, as depicted in Figure 2-2b. This transverse magnetization decay can be characterized with the following equation [25]:

$$M_{xy}(t) = M_0 e^{-\frac{t}{T_2}} \qquad \textit{Eq. 2-5}$$

where M_0 is the original longitudinal magnetization magnitude, t is the time following excitation, and T_2 is a tissue-dependent time constant describing the time required for the transverse magnetization to fall to 37% of its original value. It should be noted that T_2 decay is an idealized scenario that is never fully observed during MRI imaging. Intravoxel magnetic field changes from sources such as $\boldsymbol{B_0}$ inhomogeneity, magnetic susceptibility differences, and other factors result in more rapid transverse decay than described by Eq. 2-

5. This increased dephasing is characterized by the T_2* time constant, which is always shorter than T_2 for the same tissue.

T_1 and T_2* are critical parameters in describing the signal measured during an MRI scan. To acquire data during imaging, a receiver coil is placed so that it is sensitive to flux orthogonal to the $\boldsymbol{B_0}$ field. When spins are excited and the transverse magnetization precesses around the $\boldsymbol{B_0}$ field, a signal, known as a free induction decay, is induced as shown in Figure 2-3 and described by Eq. 2-6.

$$MR\ Signal = |M_{xy}|e^{i\omega t}e^{-\frac{t}{T_2^*}} \qquad \textit{Eq. 2-6}$$

T_1 is an important parameter, as the rate of regrowth determines how much magnetization is available to be excited in successive excitations. T_2*, on the other hand, defines the envelope function for the decay of previously excited signal. It is important to note that Eq. 2-6 includes a phase component ($e^{i\omega t}$, where $\phi=\omega t$) which describes the precession of the transverse magnetization relative to the receiver coil and is the fundamental basis for phase contrast MRI, which will be explored in more detail later in this review.

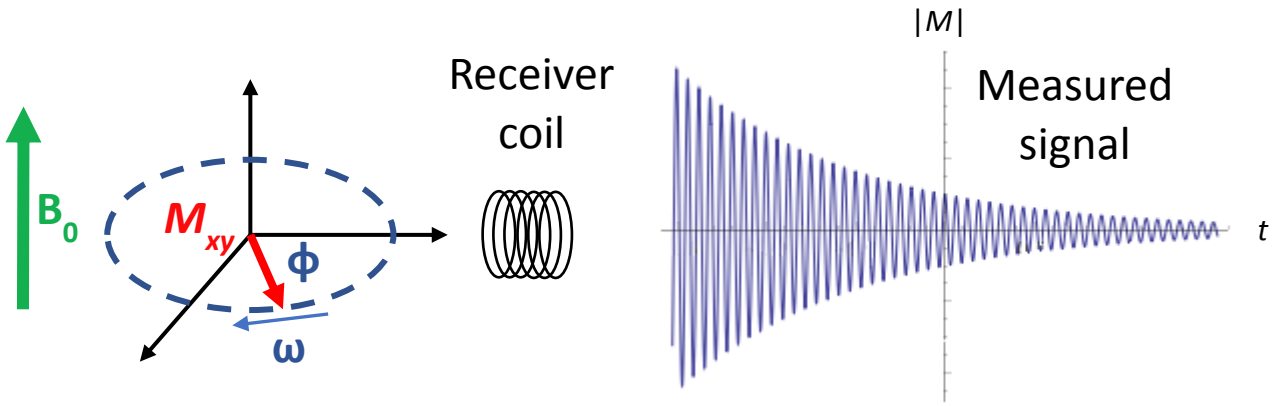

Figure 2-3: Depiction of how signal is measured during an MRI exam. The signal includes decreasing magnitude over time due to T_2 decay (loss of spin coherence and regrowth of longitudinal magnetization) and a phase term (from the magnetization rotating relative to the receiver coil).*

2.1.3 Spatial Encoding

The sequences used in this dissertation are gradient echo sequences [26], which are typically faster than

spin echo sequences [27]. Hence, the following review of signal encoding will focus on gradient echo signal generation. The MR signal described above cannot be used to reconstruct useful images unless the measured signal can be spatially localized. This is typically performed through the clever use of low-strength (relative to the $\boldsymbol{B_0}$ field), spatially-varying magnetic fields known as gradient fields.

The RF pulses used for excitation are typically non-selective, so additional steps must be taken to ensure they only excite the slice (for 2D imaging) or volume (for 3D imaging) of interest. This is achieved by applying a slice-select gradient, denoted G_z, along the direction of the $\boldsymbol{B_0}$ field during excitation [28]. Due to this gradient, the observed magnetic fields, and thus Larmor frequency, for identical tissues will linearly vary along the direction of the gradient. As a result, when an RF pulse is applied, only the tissues with Larmor frequencies within the bandwidth of the pulse will be excited, allowing for selective excitation. This phenomenon is visualized in Figure 2-4. From this figure, it is apparent that there is a direct correlation between transmit bandwidth, gradient strength, and slice thickness. This relationship can be quantified in Eq. 2-7

$$\Delta z = \frac{\Delta\omega}{\gamma G_z} \qquad \textit{Eq. 2-7}$$

where Δz is the slice thickness and $\Delta\omega$ is the transmit bandwidth.

A similar principle is exploited for in-plane spatial encoding [28]. If a magnetic field gradient is applied during signal acquisition, spins will precess at different frequencies dependent on their position along the gradient axis. Thus, the recorded signal will include a superposition of signals at a range of frequencies, which, through image reconstruction, can be demodulated and assigned to the corresponding spatial location along the gradient axis. The direction of frequency encoding is typically called the readout direction and often corresponds to the x axis with traditional MR techniques.

Conventional MRI acquisitions use a Cartesian trajectory to sample data in a raster pattern. This sampling pattern requires a second method for in-plane spatial encoding, as simultaneous frequency encoding along two axes will lead to redundant characteristic frequencies at different spatial locations.

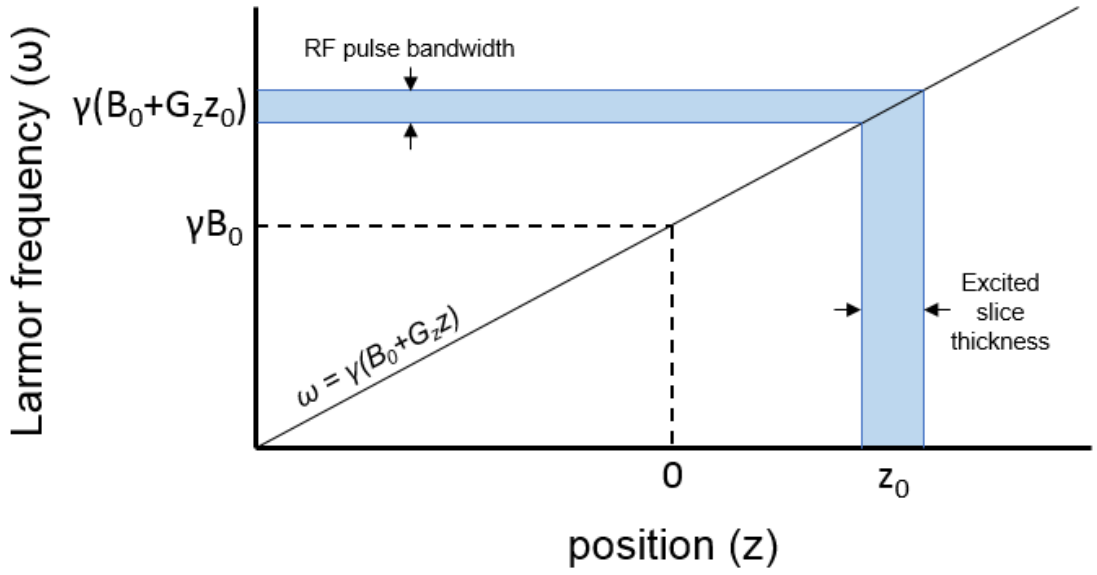

Figure 2-4: Selective excitation with a slice-select gradient and tailored RF pulse. The slice select gradient creates a dependence on position in the gradient for Larmor precession rate. As a result, when excitation is carried out with an RF pulse, only locations containing spins precessing at rates within the transmit bandwidth are affected.

Therefore, a technique called phase encoding [28], is used to encode spatial information along the orthogonal (y) axis. With phase encoding, a magnetic field gradient (phase encoding gradient) is played for a finite amount of time between spin excitation and data acquisition. This results in a linear phase accumulation amongst spins corresponding to their position along the phase encoding gradient axis. Due to the non-uniqueness of phase information, however, phase encoding requires multiple acquisitions to discern phase contributions from separate voxels along the same readout axis.

Rather than the more common Cartesian trajectory, however, the work presented here prominently features sequences with radial trajectories [29]. Radial trajectories do not incorporate phase encoding, but instead modulate the frequency encoding gradient across along both the x and y axes to rotate the readout axis and cover a circular field of view. Each spoke of such an acquisition is called a projection, a throwback to early reconstruction approaches for radial trajectories that used backprojection [30]. A comparison of Cartesian and radial trajectories is shown in Figure 2-5. Radial trajectories support high degrees of

undersampling, as undersampling artifacts manifest as relatively benign, low-signal streaking on images, as demonstrated in Figure 2-6 [31]. In addition to this, radial trajectories feature many other desirable characteristics including increased robustness to motion, isotropic spatial resolution, and good support for reconstructions with varying temporal resolutions [29,31].

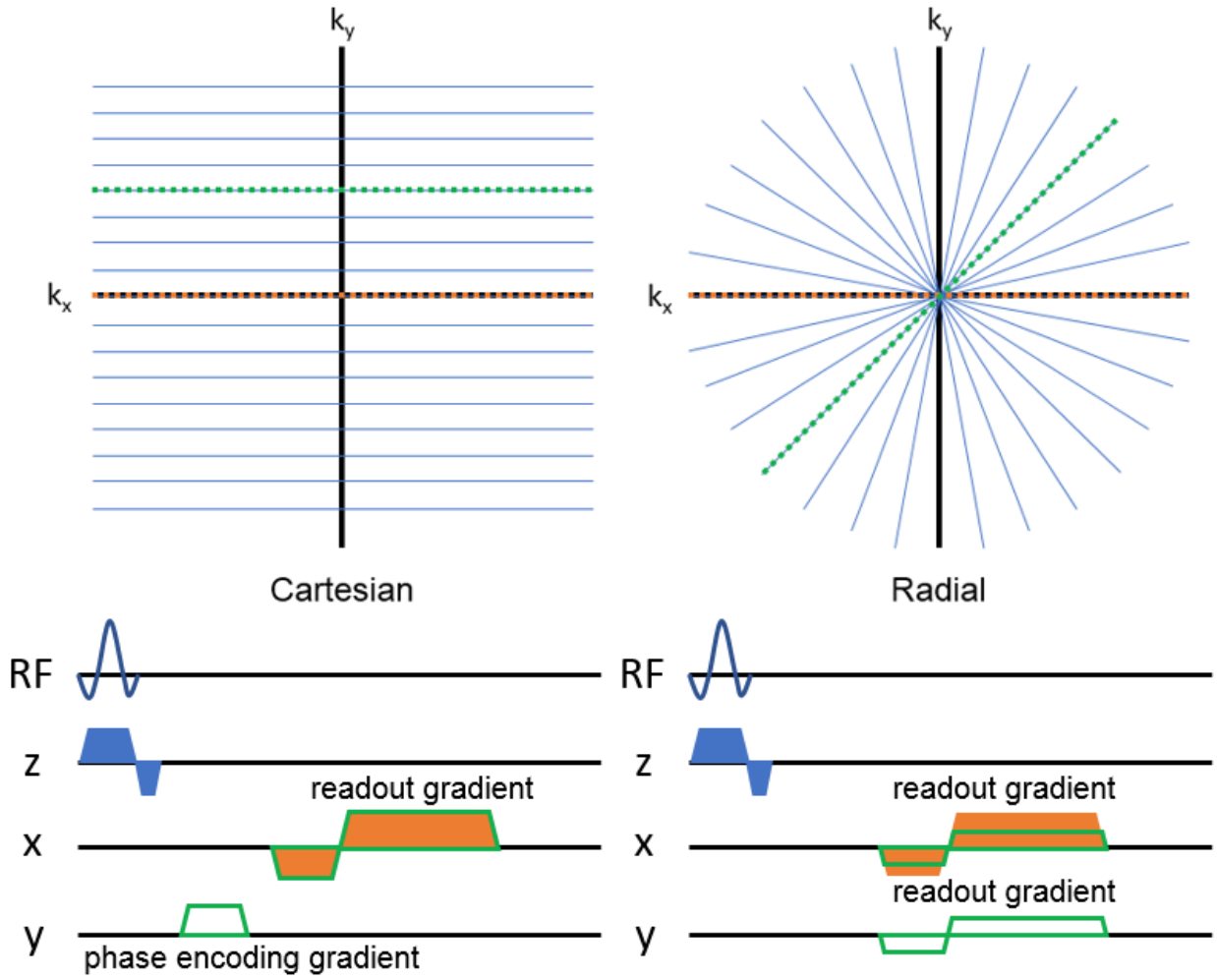

Figure 2-5: Comparison of Cartesian and radial trajectories and the differences in spatial encoding gradients required to achieve these trajectories. Gradients are color-coded to correspond to the readout they must be played for. As shown, Cartesian techniques play the same readout gradient for each readout, but must play an additional phase encoding gradient to encode data not along the k_x axis. On the other hand, radial trajectories do not require phase encoding, but instead modulate the readout gradient across the x and y axes to rotate the readout.

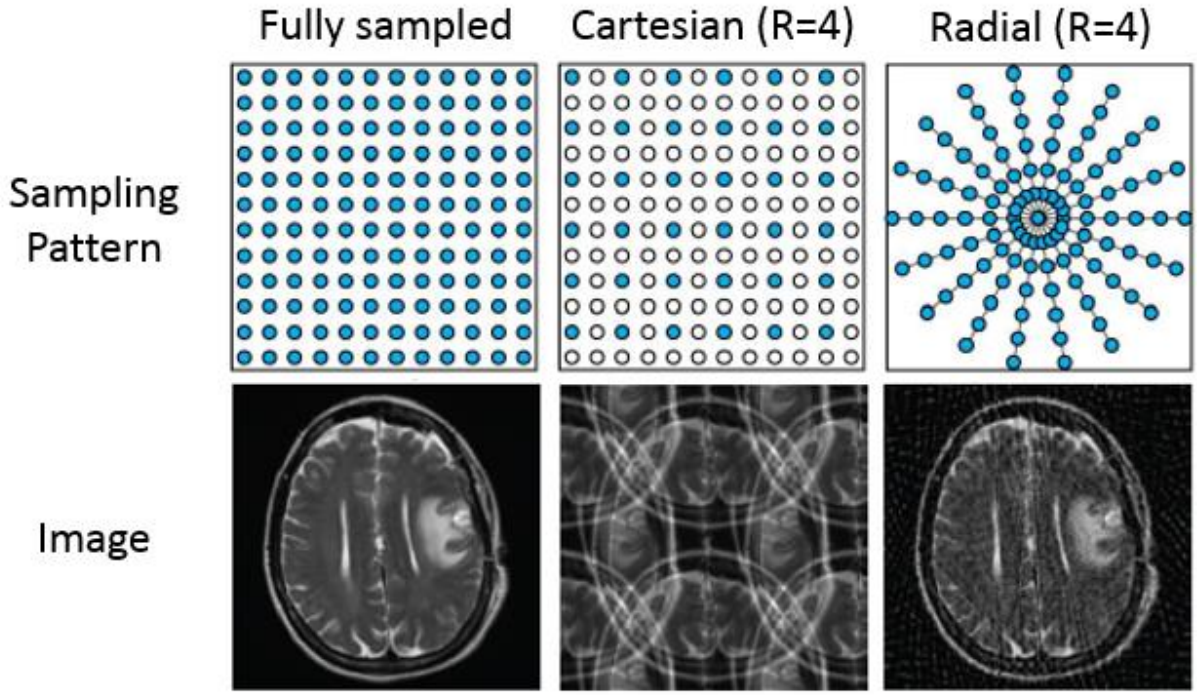

Figure 2-6: Effect of sampling pattern on undersampling. Cartesian images with four-fold undersampling demonstrate significant aliasing artifacts obscuring the true anatomy. Comparable radial undersampling shows blurring from streaking artifacts but maintains its feature resolution.

2.1.4 Image Reconstruction

The spatially-encoded MR signal described by Eq. 2-6 is demodulated into a complex value signal detailing magnitude and phase at a variety of spatial frequencies. This spatial frequency domain in which MR data is acquired is referred to as k-space [32]. Each pixel in k-space does not translate 1-to-1 with the corresponding pixel in the reconstructed image, but instead contains magnitude and phase information on a specific spatial frequency for every pixel in the final image. Pixels near the center of k-space contain low spatial frequency image content and account for much of the final image's contrast, while pixels at the periphery hold high spatial frequency content and generate fine detail in the image. When working with a Cartesian acquisition, image reconstruction is straightforward, as a Fourier transform will convert the k-space data (frequency domain) to the desired image (spatial domain). Such a transform pair is shown in Figure 2-7. With radial trajectories, a Fourier transform cannot be directly applied, as there is no support

for this transform in a polar coordinate system. Instead, a radon transform is used or the radial projection data is converted to a Cartesian grid by convolving each data point with a specialized gridding kernel and evaluating the resulting values at each point on the desired grid [33]. From there, the standard Fourier transform can be performed to reconstruct an image.

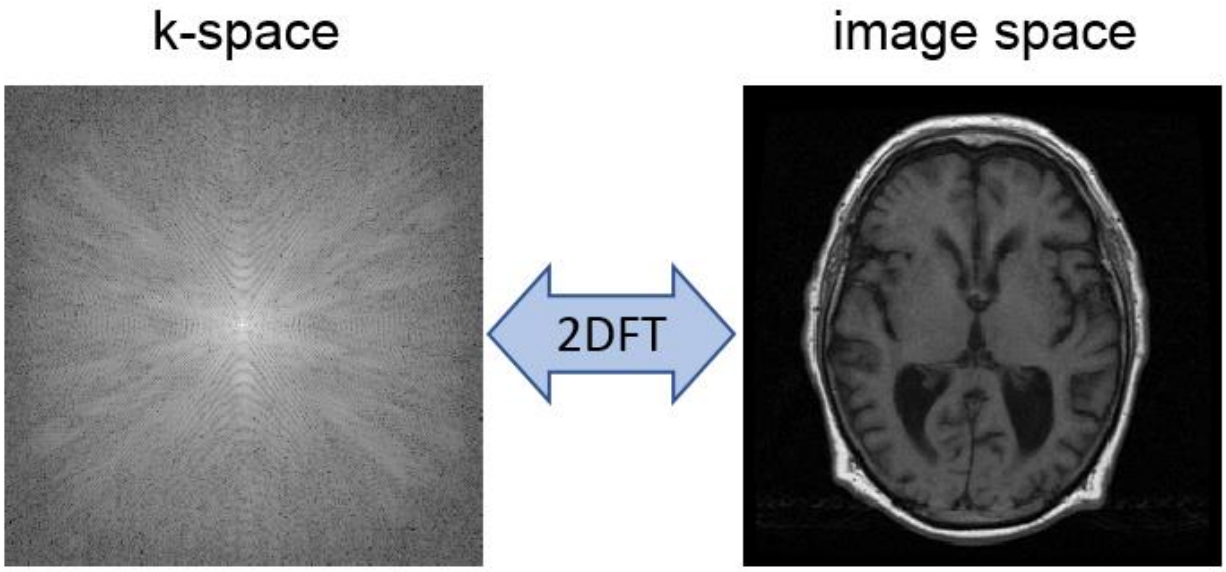

Figure 2-7: Example of k-space data transformed into an anatomical image with a 2D Fourier transform.

2.2 Phase Contrast MRI

As the Fourier transform is a complex-valued function, the resulting image is also complex with each pixel containing magnitude and phase information. Phase contributions have many sources, including sources in the image (magnetic susceptibility), physiology (motion, temperature, etc.), and hardware imperfections (magnetic field inhomogeneity, gradient field nonlinearity) [34]. Often this information is discarded and for anatomical images only the image magnitude is presented (as in Figure 2-7). With phase contrast MRI techniques, however, this inherent phase information is exploited to provide information on blood velocity [3,35,36].

When a spin is in a spatially-varying gradient field, its resonant offset frequency (with respect to

Eq. 2-1) is given by

$$\Delta\boldsymbol{\omega}(r,t) = \gamma(\Delta\boldsymbol{B_0} + \boldsymbol{r}(t)\boldsymbol{G}(t)) \qquad \textit{Eq. 2-8}$$

where $\Delta\boldsymbol{\omega}$ is the frequency offset, $\Delta\boldsymbol{B_0}$ describes variations in the $\boldsymbol{B_0}$ field from magnetic field inhomogeneity, $\boldsymbol{r}(t)$ is a spin's position in time, and $\boldsymbol{G}(t)$ is the gradient field strength a spin observes in time. Given that total phase accumulation in this context is the sum of incremental frequency changes over time with respect to spins at the Larmor frequency, phase accrual by a spin can be expressed as

$$\varphi(r,t) = \int \Delta\boldsymbol{\omega}(r,t)dt = \varphi_0 + \gamma\boldsymbol{r_0}\int \boldsymbol{G}(t)dt + \gamma\boldsymbol{v}\int \boldsymbol{G}(t)tdt \qquad \textit{Eq. 2-9}$$

where $\varphi(r,t)$ is the accrued phase, $\boldsymbol{r_0}$ is the position along the gradient axis for a stationary spin, and $\boldsymbol{v}$ is the velocity component of a moving spin along the gradient axis. Thus, the first term on the right-side of Eq. 2-9 describes phase accrual from background sources, the second term describes phase accrued when a spin is stationary in a gradient field, and the third term accounts for phase accrued by a spin moving through the gradient field. This representation assumes no higher order motion terms (i.e. acceleration, jerk). With PC MRI, the phase accrual from this third term is the point of special interest, as it can be shown that

$$\varphi_{moving} = \gamma\boldsymbol{v}\int \boldsymbol{G}(t)tdt = \gamma\boldsymbol{v}\boldsymbol{m_1} \qquad \textit{Eq. 2-10}$$

where $\boldsymbol{m_1}$ is referred to as the first gradient moment. This can be rearranged to

$$\boldsymbol{v} = \frac{\varphi_{moving}}{\gamma\boldsymbol{m_1}} \qquad \textit{Eq. 2-11}$$

demonstrating that if this phase accrual from moving spins can be measured, the velocity can be determined, which is the fundamental basis for velocity-encoding with PC MRI.

In real applications, however, there is confounding phase information as each voxel also contains phase contributions from background contributions and stationary spins, as described in Eq. 2-9. The use of bipolar gradients, where a gradient of equal strength but opposite polarity is immediately played following the first gradient, can be used encode additional phase into moving spins only. These gradients are played before the readout gradients. Figure 2-8 provides a pictorial representation of how these gradients encode phase in moving spins. Essentially, when exposed to both lobes of the bipolar gradient, static spins

experience equal-but-opposite gradient field strengths, resulting in no net phase accrual from the gradient. Moving spins, however, are constantly exposed to varying field strengths as they move through the gradient field, resulting in a net phase accrual. It should be noted that this application of bipolar gradients assumes spins are moving through the bipolar gradient field at a constant velocity.

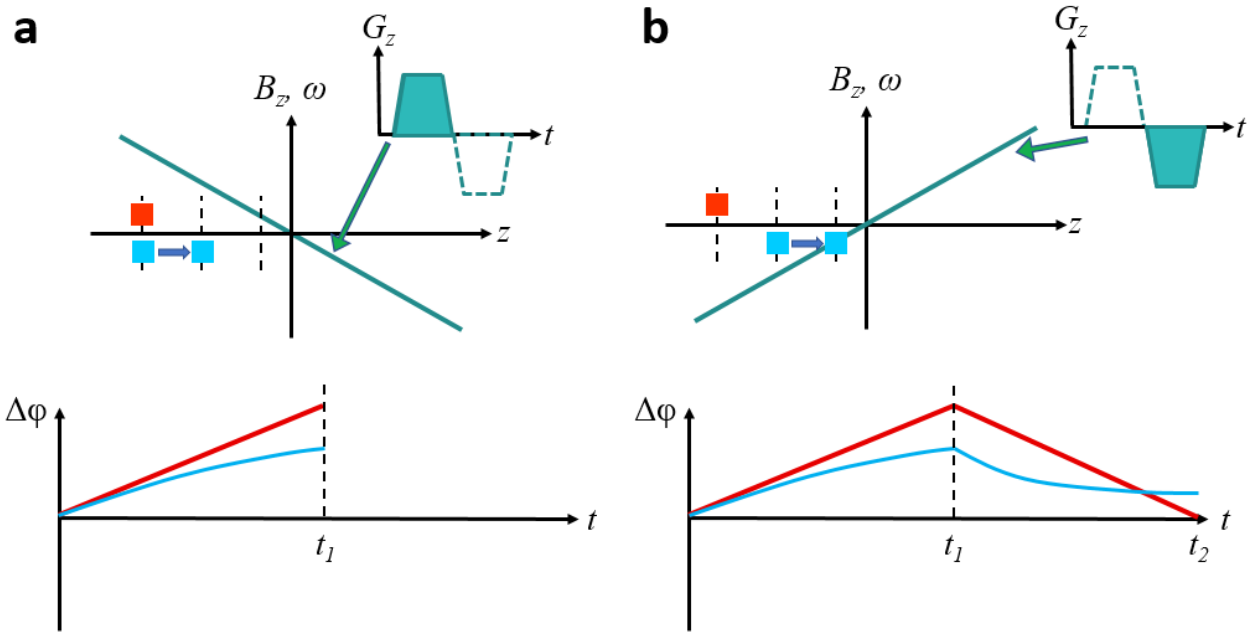

Figure 2-8: Use of bipolar velocity-encoding gradients (green) to encode phase on moving spins (blue), while providing no additional phase to stationary spins (red). (a) When the first lobe of the bipolar gradient is played, both static and moving spins begin to accrue phase. The moving spin, however, accrues less phase, as it sees continually weaker gradient fields as it moves. (b) When the opposite bipolar lobe is played, the static spins return to zero net accrued phase, as they see a gradient field of equal magnitude, but opposite polarity. The moving spins, however, are left with a net phase as they continue to experience weaker gradient fields.

Although bipolar gradients of this design do not introduce phase to static spins, all voxels have additional background phase because of other effects including magnetic susceptibility at tissue interfaces, magnetic field inhomogeneity, gradient delays, and other hardware imperfections. The additional phase from these background sources should be similar from scan-to-scan. Thus, this phase is removed by performing a second acquisition with identical imaging parameters except for the motion encoding gradients, thereby generating the same background phase which can then be subtracted from the motion

encoded image. As phase accrual encoded to moving spins must be preserved following this subtraction, there are two methods that are typically performed for the second acquisition: (1) a flow-compensated acquisition, resulting in no phase accrual in moving spins and (2) a second velocity-encoded acquisition with bipolar gradients of reversed polarity, resulting in phase accrual of opposite sign in moving spins. With these steps performed, remaining phase should be only from moving spins. Following image reconstruction, as described above, each voxel in the resulting image will contain phase proportional to the average velocity in that voxel. The exact relationship between this phase and velocity is given by

$$v_{voxel} = \frac{\varphi_{voxel}}{\pi} venc \qquad \textit{Eq. 2-12}$$

The *venc*, or velocity encoding setting, is a parameter that characterizes the maximum velocity that can be encoded in the image without ambiguity. This limitation is a result of phase only spanning from $-\pi$ to π. The *venc* is set prior to scanning and is defined as

$$venc = \frac{\pi}{\gamma \Delta \boldsymbol{m_1}} \qquad \textit{Eq. 2-13}$$

where $\Delta\mathbf{m_1}$ is the difference in gradient moments between the two velocity-encoded acquisitions. In images where the spin velocity is greater than the *venc*, the measured phase wraps around on the unit circle and velocity aliasing is present in the reconstructed images.

Phase contrast images are typically presented as magnitude images (Figure 2-9a), which include angiographic information, and phase images (Figure 2-9b), which serve as velocity maps when converted with Eq. 2-12. If a region-of-interest (ROI) is drawn around a vessel, the through-plane velocity can be integrated across this region, providing an accurate estimate of blood flow through the vessel. If data is acquired alongside ECG gating which records the point in the cardiac cycle at which each readout is recorded, readouts from multiple heart beats can be prospectively or retrospectively sorted and averaged to reconstruct multiple, high-quality cardiac image frames for a single heartbeat. Such acquisitions are referred to as cine acquisitions [37]. This data is usually acquired across a 10-15 s breath hold, reducing signal loss from respiratory motion during imaging. This allows for further analysis of changes in flow behavior across the entire cardiac cycle, as shown in Figure 2-9.

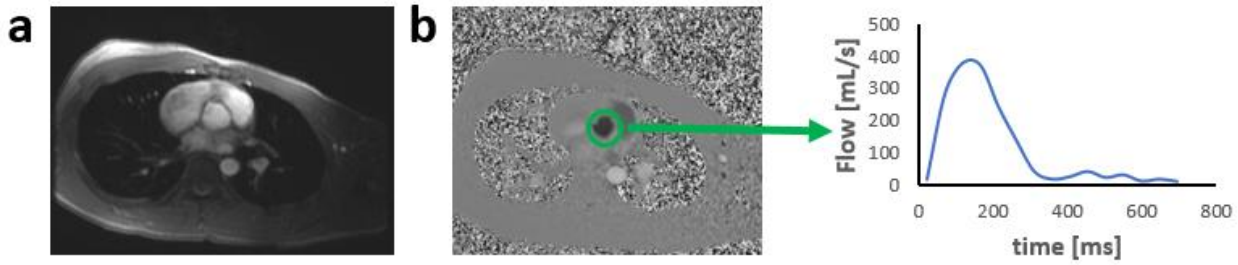

Figure 2-9: A representative pair of (a) magnitude and (b) phase images from an axial 2D cine PC MR series in the chest. Time-resolved flow measurements can be performed on the phase images by integrating velocity across a region of interest (ascending aorta in this example) for all time frames in the cardiac cycle.

Common hemodynamic parameters of interest that can be derived from vessels segmented as described above include peak systolic velocity, mean velocity, peak flow, mean flow, and total flow across a single cardiac cycle. Vessel geometry can also be assessed through measurements of vessel diameter and cross-sectional area. Other less common measurements from 2D PC acquisitions include approximations of vessel wall stiffness from relative area change or pulse wave velocity calculation [38] and estimations of pressure gradients through the use of a modified Bernoulli equation [35].

2.3 4D Flow MRI

PC MRI acquisitions are most commonly 2D cine scans which quantify through-plane flow, as described in the previous section. These techniques can be extended, however, to provide time-resolved velocity information for all three spatial directions over a volumetric acquisition, known as 4D Flow MRI [5,6]. Most simply, for each readout, this is achieved by acquiring individual acquisitions with a bipolar velocity-encoding gradient along each principal spatial axis, alongside a flow-nulled reference acquisition. This is referred to as 4-point referenced velocity-encoding and is the most straightforward extension of the 1-directional encoding described previously. Other common 4D flow encoding strategies include 4-point balanced and 5-point balanced [39], which are thoroughly described in the suggested reference. Due to the

increased number of velocity encoding acquisitions for each readout direction, along with the increased number of readouts required to adequately sample a 3D volume within the Nyquist limit, 4D flow acquisitions are generally lengthy scans, often on the order of 10 minutes or longer. This makes the breath holds used to suppress respiratory motion with 2D PC techniques infeasible. Instead, double-gated approaches are often utilized, where a respiratory gating waveform from a flexible belt placed around the subject's abdomen is recorded, alongside standard ECG gating [40]. This allows for a comfortable, free-breathing acquisition with rejection of data points acquired during moments of the respiratory cycle with significant motion during data reconstruction.

Post processing of 4D flow MRI data allows for the creation of robust PC angiograms from complex difference data. Reconstructed image data can be loaded into specialized post-processing packages to improve vessel selectivity through signal thresholding and region-growing algorithms. These vessel masks can then be visualized as 3D angiograms, as shown in Figure 2-10a. In dedicated software, 2D measurement planes can be manually placed orthogonal to vessels of interest in the angiogram mask (Figure 2-10b). To estimate flow through the vessel, the vessel is segmented with a user-drawn ROI and velocity is integrated through the region (Figure 2-10c). This retrospective approach to measure flow through vessels is a notable advantage compared to 2D PC, as it allows for more accurate measurement plane placement in the presence of small, tortuous, or moving vessels after the scan is completed.

4D flow MRI also allows for many powerful representations of time-resolved flow fields not possible with 2D PC techniques. The change in 3D velocity fields over time can be used to create streamline and pathline visualizations, as shown in Figure 2-11. Such depictions allow for qualitative assessment of complex flow not well-described by traditional hemodynamic parameters. Supplemental parameters such as vorticity, helicity, kinetic energy, wall shear stress, and pressure gradients can also be determined from knowledge of the three velocity components [5].

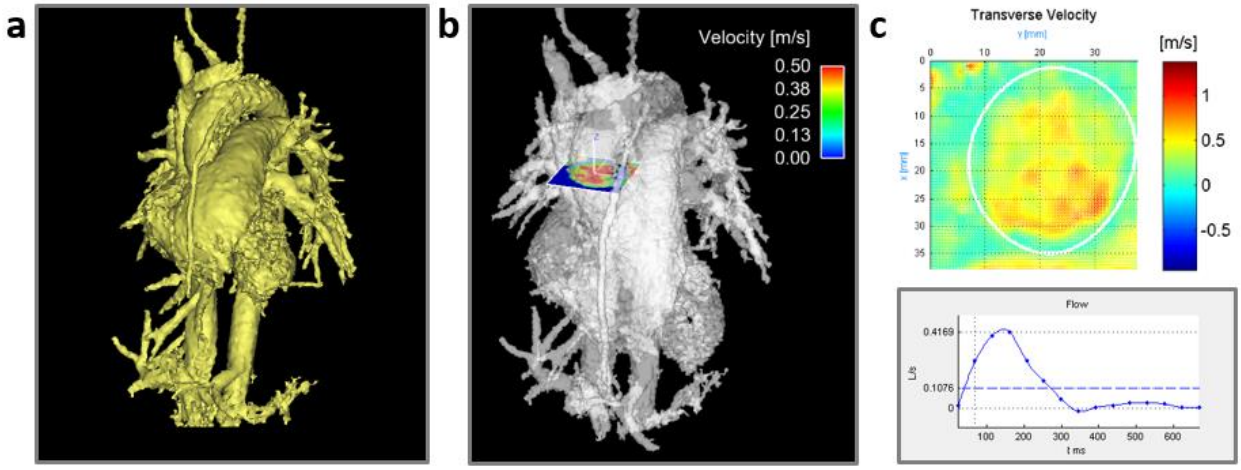

Figure 2-10: 4D flow post-processing pipeline. (a) Representative 3D cardiac angiogram derived from reconstructed complex difference 4D flow data and displayed as surface shaded display and volume rendered display. (b) 2D measurement planes are positioned relative to vessels-of-interest in 3D on the angiogram mask. (c) ROIs are drawn by the user to segment the vessel boundaries on these measurement planes, allowing for time resolved flow measurements by integrating velocity across the vessel area.

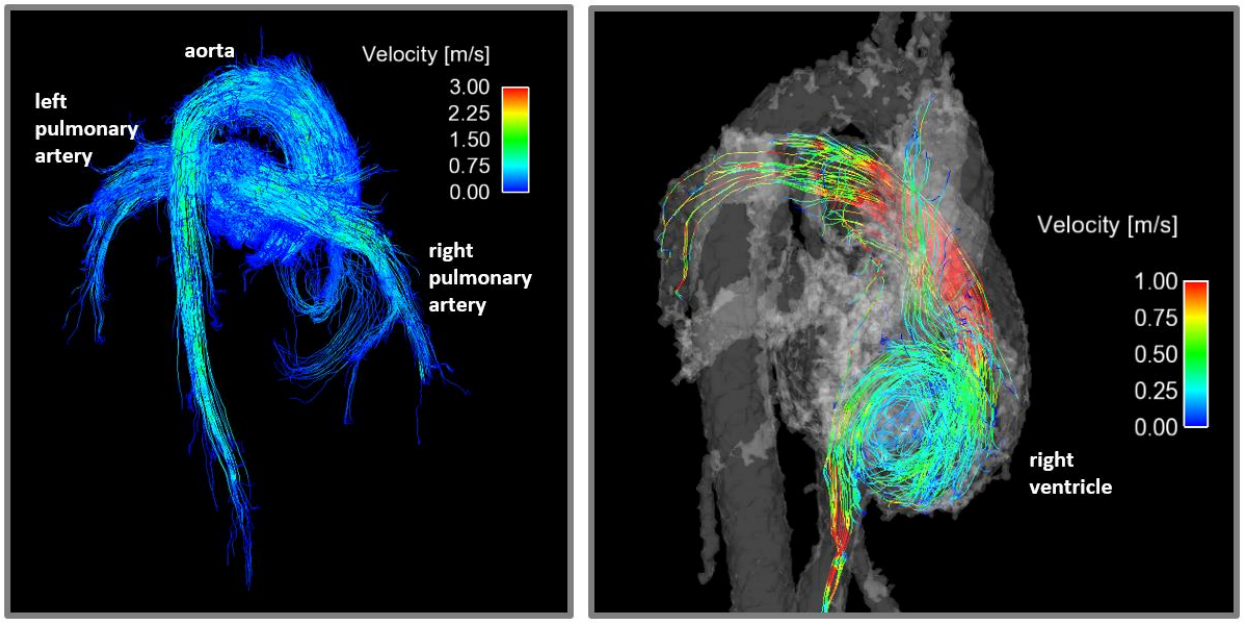

Figure 2-11: Streamline visualizations of systolic flow in the aorta and pulmonary arteries (left) and a diastolic filling vortex in the right ventricle (right).

2.3.1 PC VIPR

Most 4D flow sequences utilize Cartesian trajectories, which require time-consuming phase encoding in

two spatial directions. To maintain clinically feasible scan times, these sequences must employ limited imaging volumes or acceleration techniques such as parallel imaging or spatiotemporal undersampling [41,42]. A unique 4D flow technique called Phase Contrast Vastly-undersampled Isotropic Projection Imaging (PC VIPR) was developed here at the University of Wisconsin – Madison [43,44] which exploits a highly-undersampled radial trajectory to allow for both improved spatial and temporal resolution per unit scan time when compared to Cartesian techniques. This approach also allows for larger volume acquisitions in similar scan times and provides increased robustness to motion artifacts. The k-space trajectory of this sequence is shown in Figure 2-12.

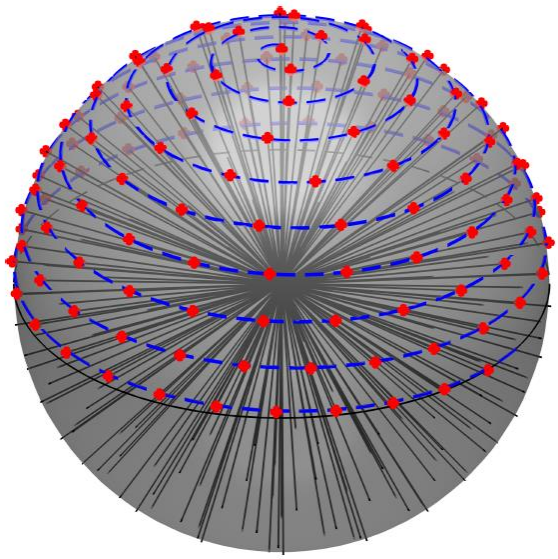

Figure 2-12: PC VIPR utilizes a highly-undersampled 3D radial trajectory to cover k-space. The radial trajectory is designed so spokes are evenly distributed throughout the volume of a sphere. Image courtesy Ashley Anderson.

2.4 Current Applications of PC MRI

2.4.1 Clinical

Phase contrast MRI is used to assess a variety of cardiovascular diseases in clinical settings. The most common applications include calculations of stroke volume (SV) and cardiac output (CO), as measured in

the ascending aorta (AAo) or main pulmonary artery (MPA), to assess basic cardiac function. In patients with aortic coarctation or vascular stenosis, PC MRI can be used to calculate increased blood velocities and estimate the pressure drop across the vessel narrowing [45]. PC MRI is also utilized to assist in diagnosis of aortic dissection and identification of false lumens [46]. In patients with cerebrovascular disease, such techniques are used to assess the effects of atherosclerotic disease and characterize flow in arteriovenous malformations [47]. In addition to these applications, PC MRI acquisitions are routinely used to quantify shunt flows, regurgitant flows, and collateral flows [45]. The flow visualization capabilities of 4D flow MRI have proved valuable in the clinic to assess flow directionality in regions with complex flow, such as the liver [48], kidneys [49], and hearts of patients with congenital heart disease [50]. Such analysis has become feasible for clinical workflow with the introduction of commercial software packages for clinical 4D flow analysis, such as Arterys (Arterys Inc.) and CVI^{42} (Circle Cardiovascular Imaging Inc.).

2.4.2 Research

There are a variety of research applications of PC MRI currently under investigation that hold promise to improve the clinical utility of these sequences in the near future. Real-time 2D PC sequences that do not require cardiac or respiratory gating have been investigated to improve patient comfort, reconstruction robustness, and allow for characterization of beat-to-beat variations in flow [51]. 4D flow techniques are currently being used to assess potential of many new biomarkers in a variety of diseases for assessing cardiovascular health. These include wall shear stress [52], pulse wave velocity [53], and kinetic energy [54], among others. The improved characterization of velocity fields inherent to 4D flow should allow for more accurate calculation of such parameters, improving prognostic and diagnostic capabilities. In addition to assessing the value of these parameters, there is significant work towards improved understanding of complex flow dynamics, such as the highly vortical, 3D flow found in the ventricles. Recent advances have seen the introduction of tools to identify residual volumes of blood in the ventricles following systole [55] and characterize complex vortical flow during diastolic filling [56]. Such investigations have been previously impossible with 2D techniques, such as 2D PC and Doppler ultrasound. Alongside these

technical innovations, 4D flow MRI is also being applied to a wide range of novel applications, including uteroplacental and fetal imaging [12] and virtual surgery [57].

2.5 Alternative Clinical Techniques

Flow quantification in clinical settings is often performed with Doppler ultrasound (US) [58]. This technique can approximate blood velocities *in vivo* by calculating the Doppler shift induced on a reflected US beam by moving blood. The measured average velocity and vessel diameter can then be fit to pre-established models of cross-sectional area and vascular velocity profiles to estimate flow in the vessel. Doppler US is the most commonly used modality for flow imaging in the clinic given its portability, fast exam speed, and relatively low exam cost when compared to MRI. Given its utility, this modality is prominently used in clinical applications relevant to the work presented in this dissertation: flow measurements in the uteroplacental and fetal vasculature during pregnancy and heart during exercise examinations.

2.5.1 Doppler US during Pregnancy

Doppler US is routinely used to assess flow in the uteroplacental and fetal vasculature to detect early indications of pregnancy complications. Hemodynamics in the uterine arteries, umbilical vessels, and fetal aorta are of special interest. Abnormal uteroplacental flow is detected through velocity waveform analysis by grading of the presence of a pre-diastolic notch in flow waveforms and quantitative measures of the resistive index (RI) and pulsatility index (PI) [59,60]. Measures of vascular resistance in the fetal umbilical arteries are used to approximate fetal-placental resistance in high-risk pregnancies [61]. PI measurements in the fetal aorta can also be used to identify potential hypoxia or fetal growth restriction [62].

However, there are inherent limitations with US in this application. Inaccuracies in the models for vessel cross-sections and velocity profiles described above can introduce systematic errors into blood flow estimates [63] and hence, vessels with complex geometry and pulsatile flow such as uteroplacental and fetal vessels are ill-suited for Doppler flow measurements, and complementary measures such as RI and PI are used instead. RI and PI, however, have limited prognostic abilities for preeclampsia and fetal growth

restriction, with low sensitivity early in gestation. Finally, due to beam attenuation in the body, image quality while assessing the umbilical arteries and fetal vessels depends on the positioning of the fetus and transducer placement (which in turn is dependent on the skill of the sonographer). These limitations are further exacerbated in obese patients, a significant subject population in North America.

2.5.2 Exercise Stress Echocardiography

Exercise stress tests can reveal important diagnostic information beyond that seen with tests performed at a resting heart rate [64]. Clinically, exercise tests are commonly performed with a treadmill or stationary bicycle and imaged with echocardiography for cardiac function and flow measurements [65]. These tests target elevating the subject's heart rate to a pre-designated level defined in one of several possible ways: a pre-defined exercise power protocol (such as the well-established Bruce protocol [66]) – possibly until the subject reaches their maximum exercise capacity and can no longer continue, a target heart rate, or a selected rate of oxygen consumption [67]. Clinical measures of interest in stress echocardiography tests include ventricular volumes [68], myocardial wall motion abnormalities in coronary artery disease [69], and velocity measurements for evaluating the severity of valvular dysfunction [70]. This technique has been standardized and well-validated for left-heart analysis.

These techniques are limited in some patient populations, however. Echo imaging of the right ventricle (RV) is less reliable given the anterior position of the ventricle in the chest (resulting in greater beam attenuation and signal loss) and its complex geometric shape [71]. This is a notable limitation in diagnosing and monitoring patients who suffer from right-heart diseases, such as pulmonary hypertension, or whole-heart conditions, such as congenital heart defects. On top of this, the 2D flow approximated by Doppler US is not adequate to fully characterize the complex 3D flow patterns found in the ventricles.

The remainder of this dissertation will focus on the development and implementation of 4D flow techniques described in this chapter to overcome the limitations of clinical Doppler US in these applications.

Chapter 3: Feasibility of 4D Flow MRI during Pregnancy[a]

3.1 Background

3.1.1 Placenta Physiology

Many pregnancy complications are associated with poor uteroplacental vascular adaptation to placental and fetal growth. Compromised uteroplacental blood flow and placental perfusion has been linked to fetal growth restriction (FGR) [72,73], preeclampsia, preterm birth, and stillbirth [74–76]. Non-invasive assessment of uteroplacental blood flow and function could play an important role in detecting insufficient blood flow to the placenta and guide decision making to reduce adverse effects, particularly if used in early stages of pregnancy before clinical manifestation of adverse pathophysiology [77]. For example, there is strong clinical evidence that low-dose aspirin can reduce the risk of FGR and preeclampsia in women with reduced blood flow [78], and intensified monitoring of these pregnancies can allow for appropriately timed delivery.

As shown in Figure 3-1, most of the maternal oxygenated blood enters the placenta through the left and right uterine arteries (UtA) with additional contributions through the left and right uterine branches of the ovarian arteries (ovarian stem arteries (OSA)) [79,80]. Hence, comprehensive characterization of total uteroplacental blood flow requires measurements in these arteries or their corresponding veins. On the fetal side, two umbilical arteries carry deoxygenated, nutrient-depleted blood from the fetus to the placenta, and oxygenated, nutrient-rich blood is returned from the placenta to the growing fetus through the umbilical vein.

---

[a]This chapter includes content from: Macdonald JA, Corrado PA, Nguyen SM, Johnson KM, Francois CJ, Magness RR, Shah DM, Golos TG, Wieben O. Uteroplacental and Fetal 4D Flow MRI in the Pregnant Rhesus Macaque. Journal of Magnetic Resonance Imaging. 2018. doi: 10.1002/jmri.26206

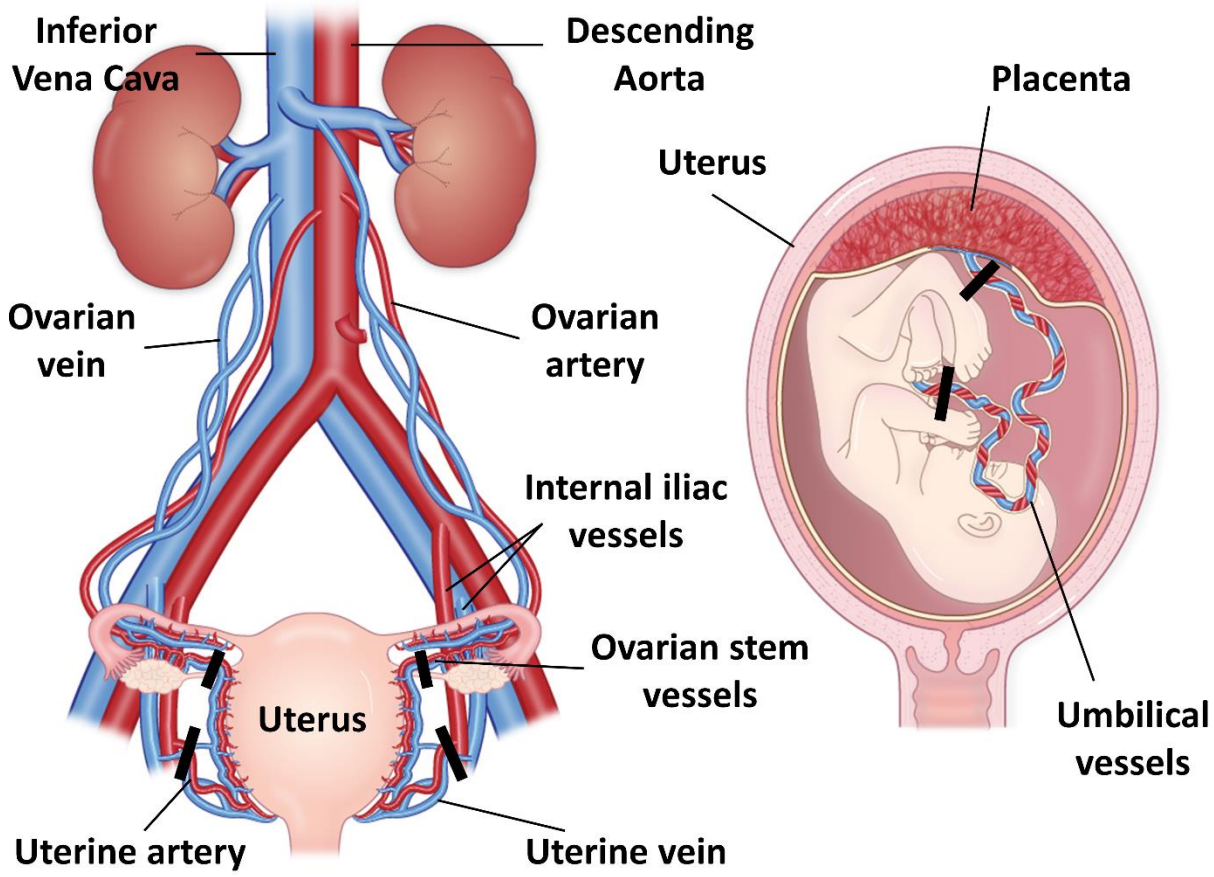

Figure 3-1: Vascular anatomy of the human placenta. Most of the maternal arterial blood in the placenta is supplied by the uterine arteries with additional contributions from the ovarian stem arteries. Corresponding veins run alongside these vessels and transport deoxygenated blood from the placenta. The arteries feed the spiral veins, which drain into an intervillous space in the placenta where nutrients and oxygen can be transferred to and from the fetal circulation through two umbilical arteries and one umbilical vein in the umbilical cord. Measurement planes required to quantify total uteroplacental and fetal-placental flow are marked by black bars. The human placenta features a single placental disc.

3.1.2 Flow Quantification during Pregnancy

Hemodynamics in the UtAs, umbilical vessels, and fetal aorta are routinely assessed with Doppler ultrasound (US). US offers high temporal resolution and is widely availability in prenatal care. As previously mentioned in Chapter 2, however, US is ill-suited for characterizing complex flow in the tortuous uteroplacental vasculature, and as a result, has poor sensitivity for standard clinical parameters early in gestation. Doppler US is also typically unable to visualize contributions from the OSAs, and thus cannot determine total uteroplacental blood flow in humans. These factors make accurate diagnosis of early

pregnancy complications with this modality challenging.

MRI is arguably well-suited to probe placental function and health during pregnancy as it can potentially quantify uteroplacental flow, perfusion [81], and tissue oxygenation [82]. Currently, MRI is not used for screening maternal or fetal health during pregnancy and is limited to surgical indications, such as suspected appendicitis [83], due to higher costs and the lack of definitive safety studies [84,85]. With validated protocols and dedicated safety studies, however, MRI flow analysis could improve early identification of pregnancy complications and enable and monitor therapeutic interventions in high-risk populations.

Previous studies have attempted flow measurements in uteroplacental vessels with 2D PC MRI [36]. One such 2D PC feasibility study aimed to measure total uteroplacental blood flow but encountered difficulties in prescribing scan planes orthogonal to the small and torturous UtAs and OSAs from MR angiograms [86]. Another compared 2D PC and Doppler US flow estimates in the UtAs with good agreement in early 3rd trimester when the uteroplacental vessels had remodeled and dilated [87]. However, the ovarian branches were not included and detection of abnormalities at this stage in pregnancy are too late for optimal therapeutic intervention.

4D flow MRI [5] has shown potential for assessing vascular anatomy and hemodynamics in complex vascular territories, such as congenital heart disease [88] and intracranial arteriovenous malformations [89]. The inherently provided PC MR Angiograms (PC MRA) can be used to visualize the vascular anatomy in 3D and orient measurement planes orthogonal to vessels of interest in post-processing rather than during scanning. Capturing the UtAs and OSAs in a single scan requires a large imaging volume and, therefore, long acquisition times with traditional Cartesian encoding. This is problematic because of the possibility of motion artifacts from maternal breathing, fetal cardiac motion, fetal movements, and the pulsatility of the fetal and maternal cardiovascular systems. While maternal breathing and cardiac pulsatility can be mitigated through respiratory and cardiac gating, fetal motion and fetal cardiac pulsatility are challenging to control.

Herein we propose the use of PC VIPR, a 4D flow method based on 3D radial undersampling, to

overcome these obstacles in clinically feasible scan times [43,44]. The undersampled radial trajectory allows for large volumetric coverage with high, isotropic spatial resolution. In the context of pregnancy, this permits abdominal imaging encompassing the maternal great vessels, uteroplacental vessels, placenta, and fetus in a single acquisition. Both arterial and venous flow can be measured to characterize blood supply and return pathways. The inherent oversampling of the center of k-space with a radial trajectory also provides an increased robustness to motion [29] and has been validated in regions affected by respiratory motion including cardiac, liver, and renal artery studies [48–50].

3.1.3 Study Motivation

The goal of this study was to assess the feasibility and repeatability of flow measurements in the uteroplacental and fetal vasculature from a single PC VIPR acquisition, laying the groundwork for studies in human subjects. A rhesus macaque model was chosen as it allowed for scans early in pregnancy, multi-day repeatability assessment, and the use of an iron-based contrast agent for reference angiograms. The rhesus macaque features a villous organization of the placenta, extravillous trophoblast invasion with resulting remodeling of the decidual spiral arteries, and a first trimester decidual leukocyte population very similar to humans [90,91]. We hypothesize PC VIPR will prove capable of quantifying total uteroplacental flow by the early 2nd trimester and fetal flow by late 2nd trimester.

3.2 Methods

3.2.1 Animal Population

This study was approved by our institutional animal care and use committee (IACUC). Fifteen healthy, pregnant rhesus macaques received MRI examinations. The gestational ages ranged from late 1st trimester to early 3rd trimester, based on an average term of 166 days in the rhesus macaque [92]. Table 3-1 gives the gestational age and maternal weight for each rhesus macaque on the first day of imaging. Animals undergoing MRI were pre-medicated with ketamine (10 mg/kg body weight) and general anesthesia was maintained during the course of the procedure with isoflurane gas (1.5% isoflurane/O_2) using an endotracheal tube. Sedation of the pregnant mother resulted in the sedation of the fetus as well. Following

imaging, animals were monitored regularly until fully recovered from anesthesia.

3.2.2 MRI Acquisition and Reconstruction

The rhesus macaques were imaged in a right-lateral position on a 3.0 T scanner (Discovery 750, GE Healthcare, Waukesha, WI) with a 32-channel phased array torso coil. The animals were placed in a holder which ensured consistent positioning of the subjects and supported the anterior coil off of their body. 4D flow imaging of the abdomen was performed with a respiratory-gated, radially-undersampled PC VIPR [43,44] acquisition with the following scan parameters: TR/TE=6.1/2.6 ms, FA=8°, VENC=60 cm/s, axial excitation slab length=16 cm, FOV=16x16x16 cm, matrix size=192x192x192, acquired isotropic spatial resolution=0.83 mm; scan duration=10.2 min. Eleven of fifteen rhesus macaques received PC VIPR scans on consecutive days. A subset of five of these monkeys also received two PC VIPR scans on each day of imaging (a total of 13 same-day pairs). The remaining four animals received a single PC VIPR scan on one day, as summarized in Table 3-1.

Rhesus	Weight [kg]	Gestational Age [days][1]	Day-to-day Repeatability	Same-day Repeatability[2]	Single PC VIPR	Ferumoxytol
1	9.70	51	✓	✓✓		
2	8.42	66			✓	
3	8.55	69			✓	
4	9.90	91	✓			✓
5	9.77	92	✓			✓
6	8.56	92	✓			✓
7	8.56	96	✓	✓✓✓		✓
8	7.63	98	✓			✓
9	10.02	98	✓	✓✓		✓
10	9.06	99	✓	✓✓✓		✓
11	7.00	102	✓			✓
12	7.09	103	✓	✓✓✓		✓
13	10.04	106	✓			✓
14	10.58	106			✓	
15	9.97	112			✓	

[1]Average gestational term is the rhesus macaque is 166 days.

[2]Multiple check marks indicate multiple comparisons (on different days) in a monkey.

Table 3-1: Gestational ages and maternal weights for imaged rhesus macaque monkeys. The last four columns indicate which MRI scans each monkey received, while the horizontal dashed lines subdivide the rhesus macaques by trimester of gestation.

Images were reconstructed offline using the signal from an abdominal belt to include only data during expiration (50% efficiency). Reconstructions incorporated corrections for background phase offsets from gradient distortions and concomitant gradients, using polynomial based fitting of background tissue. Time-averaged PC MRAs were created by combining the magnitude and velocity data with complex difference processing [93]. Segmentation of the uteroplacental vessels (UtA/uterine veins (UtV), OSA/ovarian veins (OV)) and fetal vessels (umbilical arteries/vein, fetal aorta, fetal inferior vena cava (IVC)) was performed through signal thresholding and region-growing using MIMICS (Version 17.0, Materialize, Leuven, Belgium). This mask was imported into Ensight (Version 10.0, CEI Inc., Apex, NC) where 2D measurement planes could be manually oriented with respect to a 3D rendering of the segmented vessels, allowing for accurate plane placement in the presence of tortuous vasculature. Time-averaged flow was measured at the uteroplacental vessel midpoints by integrating through-plane velocity components over the segmented vessel areas. Flow measurements in the umbilical vessels were performed at the maternal and fetal ends of the cord (Figure 3-1), and fetal great vessel measurements were performed proximal to the heart.

Ten of the rhesus macaques imaged on consecutive days received a ferumoxytol injection on the second day of imaging, allowing for the creation of high-resolution, contrast-enhanced angiograms. Ferumoxytol-enhanced angiograms were acquired with a T1-weighted, spoiled gradient echo, 3D ultrashort echo time (UTE) sequence with a center-out radial trajectory [94] before and after an injection of 4 mg/kg ferumoxytol (Feraheme, AMAG Pharmaceuticals, Waltham, WI) diluted 5:1 with saline and infused intravenously over 20 s. The UTE sequence had the following scan parameters: TR/TE=4.4/0.1 ms, FA=10°, FOV=18x18x18 cm^3, matrix size=360x360x360, acquired isotropic spatial resolution=0.5 mm, scan time=5.9 min. Complex subtraction processing was employed to create an angiogram with suppressed background signal. The ferumoxytol-enhanced angiograms were visualized and segmented in MIMICS.

3.2.3 Image Analysis

To assess the relative quality of the PC MRA, the conspicuity of uteroplacental and fetal vasculature was

scored in the ferumoxytol-enhanced angiogram and PC MRA for each monkey that received both scans in the same imaging session. Scoring was performed independently by two radiologists (17 and 18 years experience) using the following scale: 1=not visible, 2=partially visible, 3=fully visible. In addition to comparing the scores for each vessel between the two MRA techniques, the impact of gestational age on vessel conspicuity in the PC MRA was examined.

Day-to-day repeatability of PC VIPR measurements was assessed in the 11 monkeys imaged on consecutive days. Same-day repeatability was characterized for the 13 cases where two PC VIPR scans were performed in the same imaging session. Repeatability was assessed by calculating percentage change in flow and cross-sectional area at the midpoints of the visible uteroplacental vessels between scans. Furthermore, for all animals, inter-observer and intra-observer variability in uteroplacental flow was assessed. Inter-observer variability was assessed by comparing flow measurements from a second observer blinded to the measurement plane placements and results of the original observer. To assess intra-observer variability, the original observer repeated all uteroplacental flow measurements in each monkey. The observers had 5 and 2 years of experience in 4D flow post-processing, respectively.

Feasibility of using PC VIPR to assess uteroplacental flow was further assessed with a conservation of mass analysis, where in-flow to the uterus was compared against out-flow. When possible, fetal flow consistency was also assessed by measuring percentage change in flow in the fetal IVC to the ascending aorta. Flow consistency in the umbilical cord was assessed by comparing flow in the two umbilical arteries and the umbilical vein at the fetal end and placental ends of the cord.

3.2.4 Statistical Analysis

Continuous variables are reported as mean ± standard deviation. The significance of differences in image scoring between the PC MRA and ferumoxytol-enhanced angiograms for each vessel were compared using a Wilcoxon rank-sum test. Differences in inter-observer scoring for each case were assessed with paired t-tests. Bland-Altman analysis was employed to evaluate the mean difference (d) and 95% limits of agreement (LoA) for same-day and consecutive-day scans, inter-observer variability analysis, and intra-

observability variability analysis. Correlation in the repeatability studies was assessed via a linear regression analysis of the repeated flow measurements and calculation of the Pearson correlation coefficient (r). All tests used a threshold of α=0.05 for statistical significance.

3.3 Results

3.3.1 Qualitative Assessment

PC VIPR angiograms were successfully reconstructed in all rhesus macaques. Figure 3-2 shows PC MRAs of representative rhesus macaques in the late 1st trimester, early 2nd trimester, and early 3rd trimester of pregnancy. Radiologist scoring of the MRAs confirmed clear visualization of the UtAs and OVs as early as the end of the 1st trimester, with enhanced visualization of other uteroplacental and fetal vessels by late 2nd trimester. Radiologist scoring (right/left UtA=2.8±0.6/2.9±0.4; right/left OV=2.9±0.2/2.8±0.4) confirmed the UtAs and OVs were fully visible in almost all cases. Notably absent from most segmentations were the UtVs and OSAs, which received lower scores (right/left UtV=1.9±0.2/1.8±0.4; right/left OSA=1.6±0.6/1.5±0.6). These vessels were only fully observed in one rhesus macaque each. The fetal and umbilical vessels were visible in most cases (umbilical/fetal vessels=2.5±0.7/2.5±0.7).

A representative segmentation of the fetal and umbilical vessels in the early 3rd trimester of gestation is shown in Figure 3-3. Figure 3-4 shows a comparison of segmented PC angiograms in one of the rhesus macaques that received multiple scans on back-to-back days. Angiograms acquired on the same day appeared to be almost identical, while angiograms from back-to-back days showed notable differences in the position of the fetus and the trajectory of the OVs.

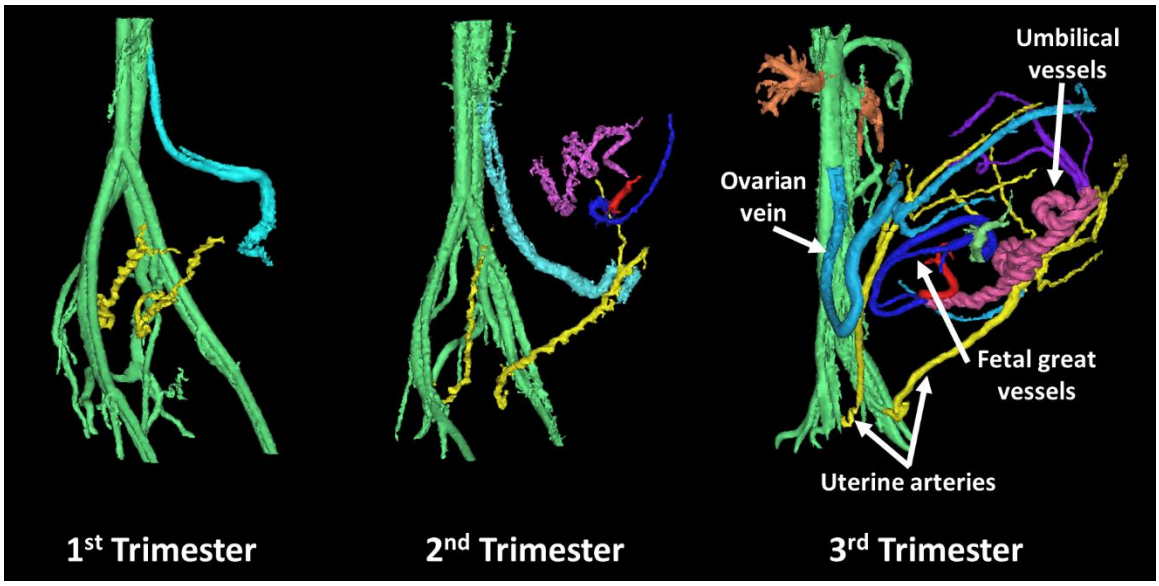

Figure 3-2: Representative PC MRA of three separate healthy pregnant rhesus macaques at different trimesters of gestation. The main arterial blood supply to the placenta appeared to be the uterine arteries (yellow), while the main venous return was through the ovarian veins (light blue). Uterine veins and ovarian stem arteries were not apparent. While fetal vessels (dark blue and red) were most notable around the 3rd trimester, the main uteroplacental vessels were seen as early as late 1st trimester.

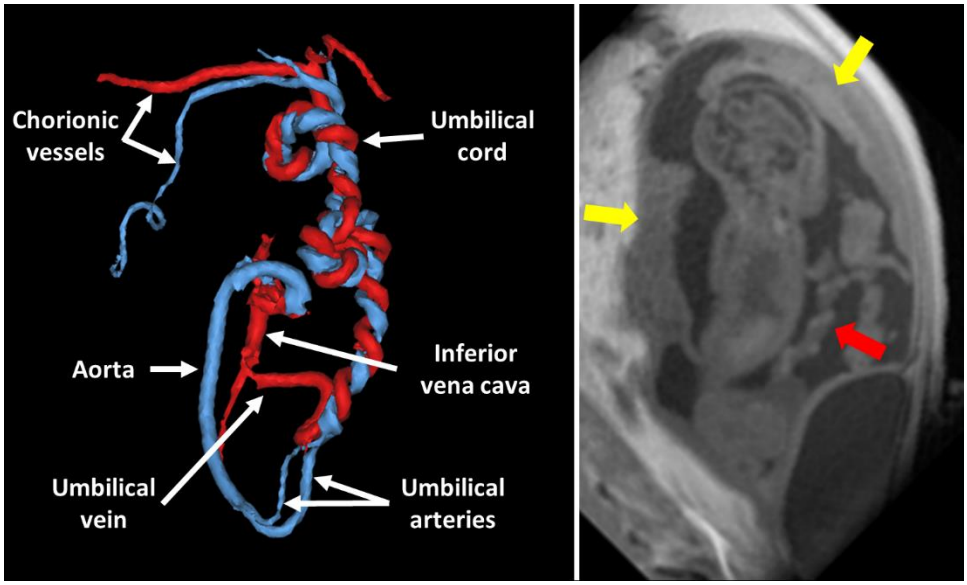

Figure 3-3: Segmented PC angiogram of the fetal and umbilical vasculature in the early 3rd trimester of pregnancy. The umbilical cord can be seen unbundling into one umbilical vein (red) and two umbilical arteries (blue), one of which forms the aortic arch, in the fetus. A corresponding slice from the PC VIPR magnitude images is shown at the right with the yellow arrows denoting placenta discs and the red arrow showing the umbilical cord.

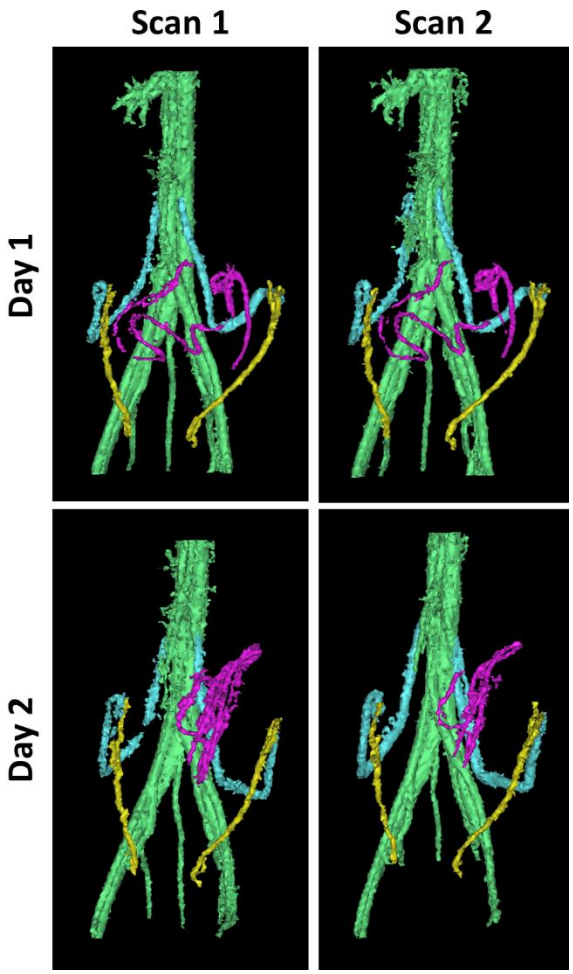

Figure 3-4: PC angiograms in a single monkey across two days. Two angiograms were acquired on each day. The uterine arteries (yellow) showed minimal motion between days, while the ovarian veins (light blue) and the fetal and umbilical vessels (purple) showed more noticeable changes in position on subsequent days. Same day scans showed similar positioning of all vessels.

High-resolution ferumoxytol-enhanced angiograms were successfully reconstructed in 9 out of 10 rhesus macaques that received contrast. One reconstruction failed due to motion of the mother between the pre- and post-contrast acquisitions. Figure 3-5 shows a representative comparison of a ferumoxytol-enhanced angiogram and the corresponding PC angiogram from the same imaging session. Like the PC MRA, the ferumoxytol-enhanced angiograms had excellent visualization of the UtAs and OVs (right/left UtA=2.8±0.4/2.8±0.4; right/left OV=2.9±0.2/2.9±0.2). These angiograms displayed enhanced vessel detail and smaller diameter vessels, allowing for slight improvements in visualization of the UtVs and OSAs

(right/left UtV=2.1±0.5/2.2±0.6; right/left OSA=2.1±0.9/1.7±0.5). The average increased visibility in these vessels, however, was not statistically significant. Contrast uptake in the intervillous space allowed for display of the placenta in the reconstructed volume rendering, but fetal and umbilical vasculature was not apparent in any of the ferumoxytol-enhanced angiograms, as expected (umbilical/fetal vessels=1±0/1±0).

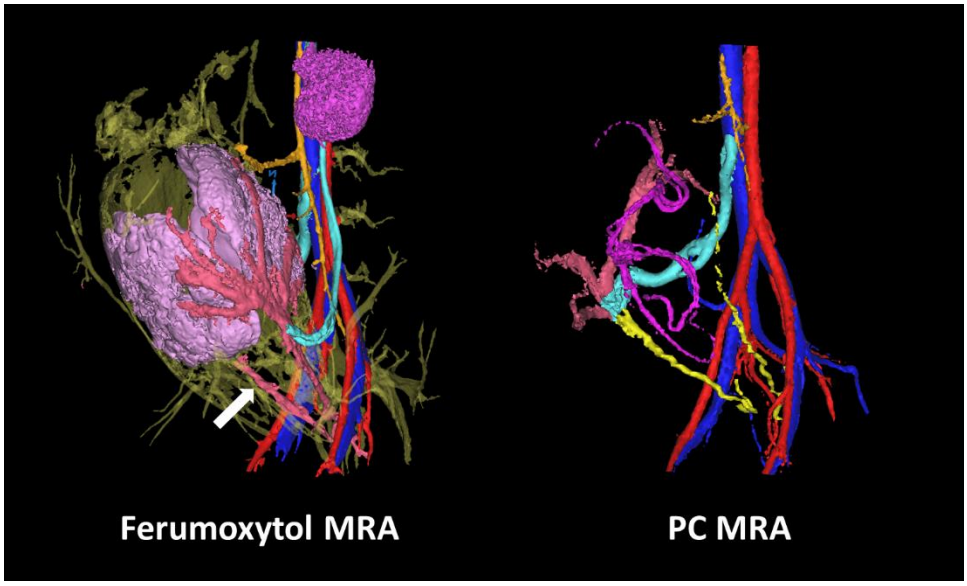

Figure 3-5: Comparison between ferumoxytol-enhanced angiogram (left) and PC angiogram (right) in the same rhesus macaque on the same day. The color scheme of the uteroplacental and fetal vessels is the same as in Figure 4, except in the ferumoxytol-enhanced angiogram where the uterine arteries and veins, which appear fused together, are a light red (white arrow).

Assessment of inter-observer vessel scoring showed excellent agreement in scoring of the UtAs, OVs, and fetal vasculature. Statistically significant differences in scoring were detected for the UtVs and OSAs in the PC MRA and UtVs in the ferumoxytol-enhanced angiograms.

3.3.2 Quantitative Assessment

Since the UtAs and OVs were seen in all rhesus macaques, flow in these vessels was assessed for the same-day and day-to-day repeatability studies. For the same-day repeatability study, both the left and right UtAs were visualized in all scans. The flow measurements in these vessels showed an average relative change of 15% in the left UtA and 11% in the right UtA (d=1.8 mL/min; LoA=-8.5 to 12.0 mL/min; r=0.88).

Nineteen of twenty-six measurements showed relative changes less than 15%, with the largest change being 31%. For the day-to-day repeatability measures, 21 of 22 individual UtAs were visualized. These measurements showed an average change in flow between days of 25% in the left UtA and 19% in the right UtA (d=-0.3 mL/min; LoA=-21.5 to 20.8 mL/min; r=0.53). Only 10 of 22 measurements showed changes less than 15%, with the largest relative change being 52%. Across all UtAs, an average change in cross-sectional area of 16% was observed between same-day scans, while a comparable change of 17% was seen between consecutive-day scans.

The inter-observer and intra-observer repeatability analysis in the UtAs revealed similar measurement distributions to the same-day repeatability analysis. Inter-observer analysis showed an average difference in flow of 16% in the left UtA and 24% in the right UtA (d=0.6 mL/min; LoA=-14.1 to 13.0 mL/min; r=0.75). Intra-observer analysis showed a slightly improved relative difference of 14% in both the right and left UtA (d=0 mL/min; LoA=-12.2 to 12.2 mL/min; r=0.79). Bland-Altman analysis of all four repeatability metrics for the UtAs is presented in Figure 3-6.

Similar results were observed in the OVs. For the same-day PC VIPR acquisitions, both the left and right OVs were successfully visualized in 11 of 13 scans, with a single vein observed in the other two scans. In these cases, measurements varied an average of 17% in the left OV and 10% in the right OV between scans (d=2.2 mL/min; LoA=-11.9 to 16.4 mL/min; r=0.94). Seventeen of twenty-four venous flow measurements varied less than 15% between scans. For the day-to-day repeatability measurements, both OVs were only apparent in four of the rhesus macaques, with the other seven expressing a single, dominant vein (6 right, 1 left). Flow in the left OV varied an average of 23%, while a similar variation of 24% was measured in the right OV (d=-2.4 mL/min; LoA=-34.3 to 29.4 mL/min; r=0.80). Only six of fifteen venous flow measurements varied less than 15% between scans. Cross-sectional area measurements at the OV midpoints changed 18% on average for same-day scans and 24% for consecutive day scans.

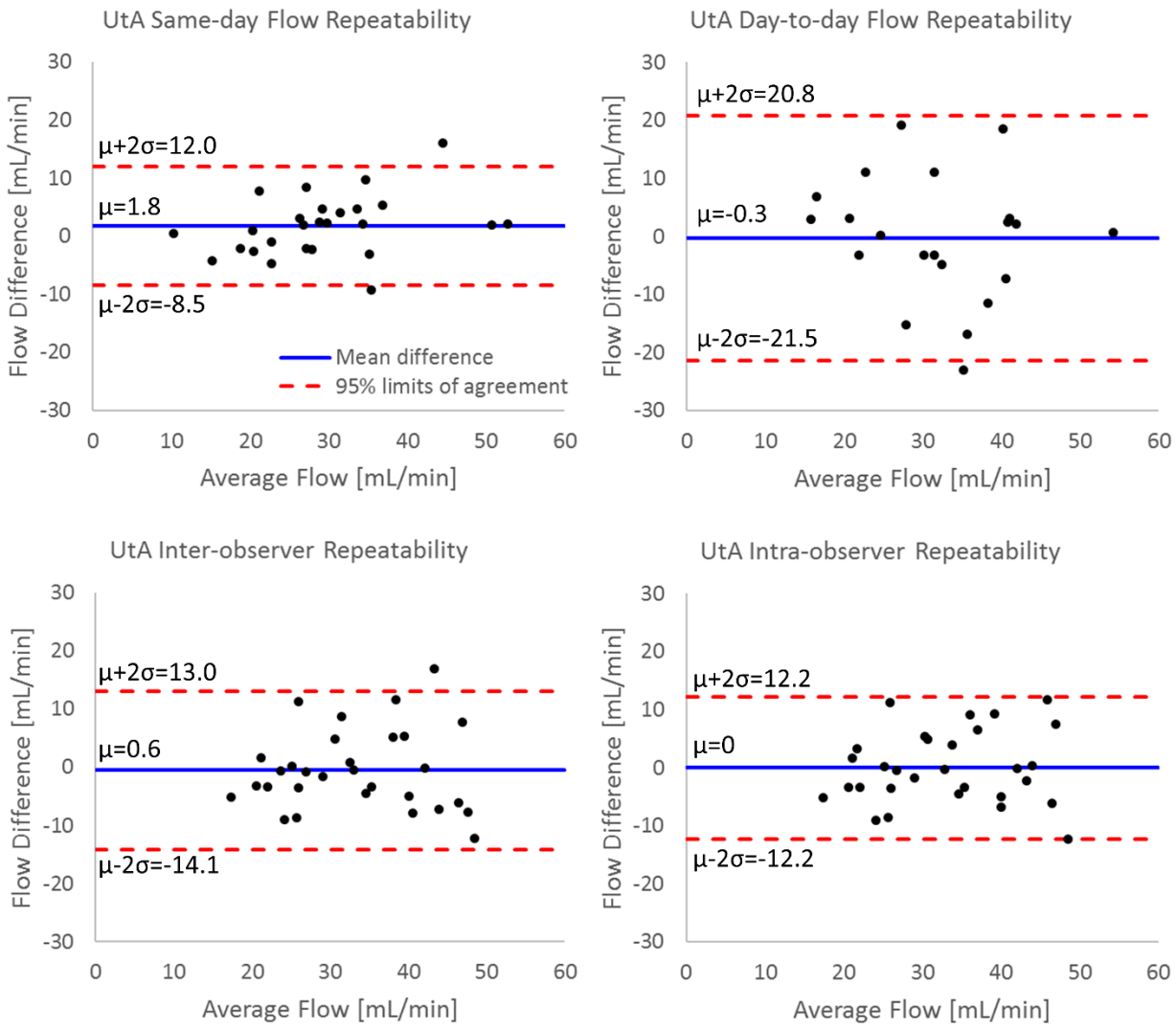

Figure 3-6: Bland-Altman analysis of flow measurements in the uterine arteries from PC VIPR acquisitions. Repeatability results are presented for repeated scans (test-retest) on the same day and consecutive days, inter-observer analysis, and intra-observer analysis.

Inter-observer measurements showed a relative difference of 24% in left OV flow and 12% in the right OV (d=1.6 mL/min; LoA=-24.1 to 27.3 mL/min; r=0.85). Intra-observer measurements were improved with relative differences in flow of 13% in the left OV and 8% in the right OV (d=1.6 mL/min; LoA=-21.0 to 24.3 mL/min; r=0.89). The Bland-Altman analysis of all four repeatability metrics for the OVs is presented in Figure 3-7.

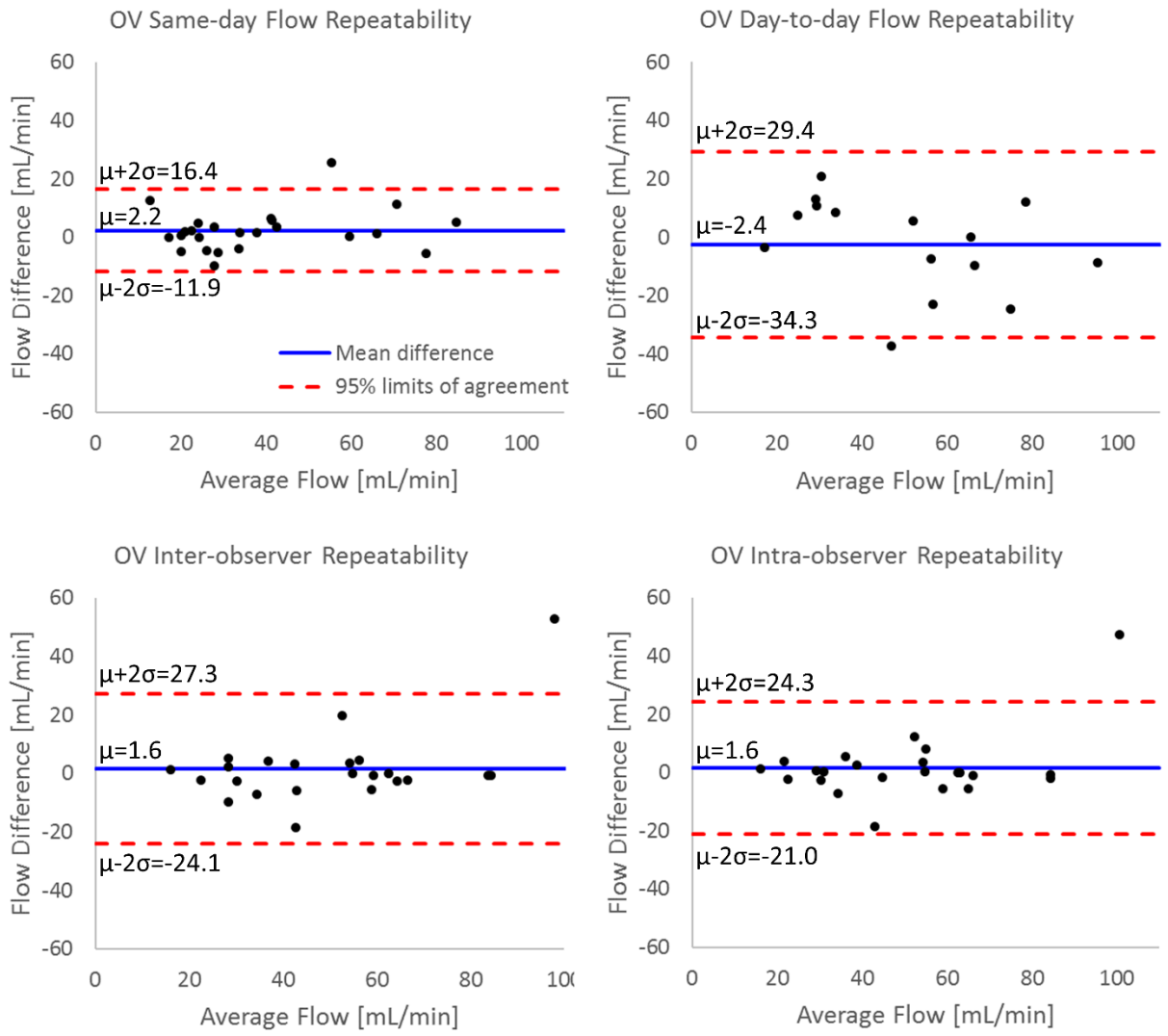

Figure 3-7: Bland-Altman analysis of flow measurements in the ovarian veins from PC VIPR acquisitions. Repeatability results are presented for repeated scans (test-retest) on the same day and consecutive days, inter-observer analysis, and intra-observer analysis.

In the singular cases in which they were fully resolved, flow in the left UtV was measured to be over 20 times less than in the associated UtA and flow in the OSA was approximately 10 times lower than the neighboring OV. Both the UtV and OSA demonstrated cross-sectional areas roughly 25% of their counterparts.

Table 3-2 gives the time-averaged flow values in each monkey in the UtAs and OVs and the difference in blood flow to and from the uterus and placenta as estimated from these vessels. Although

these comparisons were unable to account for smaller flow contributions from the OSAs, UtVs, and other collateral vessels, only an average difference of 15% was observed between placental in-flow and out-flow. Flow in the left and right UtA appeared to be relatively balanced, with similar flow measured in both vessels, while the venous return was more asymmetric, with monkeys displaying a tendency to have a dominant OV. The dominant vein was the right OV in 11/15 monkeys.

With respect to the fetal vasculature, PC VIPR acquisitions typically showed the fetal aorta and IVC by mid-2nd trimester and the full umbilical cord by the end of the 2nd trimester. Flow measurements were possible in the fetal aorta and IVC in 10/15 monkeys, while umbilical flow measurements were acquired in 6/15. The fetal great vessels showed consistency in blood flow, with an average difference in flow between the aorta and IVC of 8%. Reduced consistency was observed in the umbilical vessels, as flow measurements varied on average by 12% in the umbilical arteries and 18% in the umbilical vein between the two ends of the cord.

Rhesus	RUtA[1] [mL/min]	LUtA[2] [mL/min]	ROV[3] [mL/min]	LOV[4] [mL/min]	Difference[5]	Change[6] [%]
1	31.5	34.5	66.6	0	-0.6	0.9
2	31.9	33.8	37.6	19.6	8.5	13.0
3	43.4	40.1	76.8	0	6.7	8.0
4	27.5	20.0	50.9	0	-3.4	6.6
5	20.3	29.9	0	54.6	-4.4	8.1
6	33.0	28.2	84.6	0	-23.4	27.7
7	43.2	27.0	61.8	52.2	-43.8	38.4
8	43.8	44.4	28.8	46.2	13.2	15.0
9	22.3	36.9	33.4	30.8	-5.1	7.9
10	23.7	28.6	85.2	0	-32.9	38.6
11	20.3	30.0	63.0	0	-12.7	20.2
12	42.1	49.5	45.7	67.8	-21.8	19.2
13	54.6	37.0	62.6	38.0	-8.9	8.9
14	19.9	42.5	52.6	15.5	-5.6	8.2
15	27.8	25.1	23.8	31.7	-2.6	4.7
Average	**32.4±10.8**	**33.8±8.0**	**51.6±23.9**	**23.8±23.9**	**-9.1±15.6**	**15.0±11.7**

1. Right uterine artery; 2. Left uterine artery; 3. Right ovarian vein; 4. Left ovarian vein; 5. Difference = (RUtA+LUtA) - (ROV+LOV); 6. Change = |Difference / (RUtA+LUtA) * 100|

Table 3-2: Time-averaged blood flow as measured at the midpoint of the uterine arteries and ovarian veins.

3.4 Discussion

4D flow MRI with PC VIPR was capable of characterizing blood flow to and from the placenta and fetus in one acquisition with good spatial resolution in a clinically feasible scan time. The imaging volume of the PC VIPR acquisition encompassed the maternal descending aorta and IVC, uteroplacental vessels, fetal vessels, uterus, and placenta. This technique proved to be a reliable method of visualizing the UtAs and OVs as soon as late 1st trimester of gestation. On the other hand, the UtVs and OSAs, characterized by smaller diameters and slower flow, could not be fully detected by the early-3rd trimester of gestation, with the exception of one rhesus macaque with a fully resolved left UtV and one with a fully resolved right OSA. In these cases, the low relative flow contributions to the uterus in these vessels were consistent with that reported in the rhesus macaque elsewhere [95]. These results suggest that the primary inflow pathway of blood to the uterus in the rhesus macaque is through the UtAs and the OVs are the primary venous return, rather than blood draining through the vein corresponding to the artery with which it entered the uterus. This was further reinforced by the close agreement observed in flow measurements into the uterus through the UtAs and from the uterus via the OVs with the consistency analysis. Thus, the absence of the UtVs and OSAs in the PC VIPR images was likely from low flow, and therefore low signal, and vessel diameters the same order as the sequence spatial resolution, resulting in further signal loss from partial volume effects.

The ferumoxytol-enhanced angiograms supported this hypothesis, as the UtVs absent in the PC MRAs were more consistently visible due to enhanced spatial resolution and SNR. These angiograms also allowed consistent visualization of both OVs for all cases, whereas one was sometimes undetected with the PC MRA due to slower flow. Even with improved spatial resolution of this sequence, however, the OSAs were not well-visualized, suggesting they are unlikely to be reliably visualized with PC MRA given their small size in the rhesus macaque. The contrast-enhanced angiograms were not able to characterize fetal vasculature, as measurable amounts of contrast agent did not appear to cross the maternal-fetal interface. Overall, the ferumoxytol-enhanced angiograms proved to be more consistent than the PC angiograms in visualizing small-diameter and slow-flow uteroplacental vessels. Ferumoxytol-enhanced angiograms also

proved to be more susceptible to motion artifacts, however, as any motion between the pre- and post-contrast scans would corrupt the image subtraction in the reconstruction. The comparison of these two angiography techniques confirmed that PC VIPR was adequate for visualizing and characterizing the main pathways of placental in-flow and out-flow in the rhesus macaque, as undetected vessels were those with minimal flow contributions.

For the vessel conspicuity scoring, one radiologist had significantly more success in identifying the UtVs and OSAs in both the PC MRA and the ferumoxytol MRA. This can likely be attributed to this observer's higher experience level in reading uterine MRAs in pregnant subjects and highlights the challenges in detecting these two vessel pairs. While this observer was able to more consistently detect the UtVs and OSAs, their conspicuity was still noticeably lower than in the corresponding arteries and veins.

In both the UtAs and OVs, the repeatability studies showed good correlation and acceptable relative differences in flow measurements from multiple scans acquired on the same day, as well as in inter-observer and intra-observer comparisons. The ranges of the limits of agreement for these comparisons, however, were the same magnitude as the flow measured in these vessels. This is significant, as in order to consistently detect differences in flow induced by abnormal pregnancy, induced systemic differences in flow must exceed the limits of agreement for healthy subjects. Thus, these early results suggest this technique offers sensitivity to only significant changes in uteroplacental flow in the rhesus macaque animal model. Sensitivity to differences between groups may improve by measuring uteroplacental flow normalized by maternal cardiac output or placental volume to better describe supply inefficiencies. This was not performed in this study due to aliasing in the maternal descending aorta and the time-consuming nature of placenta segmentation from PC VIPR magnitude images. Increased sample sized may also improve statistics and reduce the limits of agreement.

Increased variability was observed between consecutive day scans. The source of the larger disagreement in flow on consecutive days did not appear to be due to technical limitations of PC VIPR, but rather movement of the fetus between scans. For same-day scans, the fetus was sedated for the entirety of the imaging session, preventing significant motion between acquisitions. With scans on back-to-back days,

however, the fetus was free to reposition itself in the time between scans. Pressure from the fetus on the placenta and uterine wall could cause blood in the uterine and ovarian vessels to redirect along a path of least resistance, altering blood flow dynamics based on fetal position. This is consistent with the noticeable decrease in measurement correlation between these scans. These results suggested that it may be difficult to discern if longitudinal changes in the flow are from changes in physiology throughout pregnancy or other factors, such as fetal position. A more robust metric would be to assess total UtA flow, rather than flow in the individual UtAs. This measurement would still be sensitive to physiologic factors such as diurnal flow variations, altered hydration levels, and varying anesthesia exposure between scans, which must be accounted for when designing longitudinal studies.

Improved repeatability was observed in the right-side vessels relative to the left-side, for both same-day and day-to-day comparisons. This was likely a result of the anterior coil being supported off of the rhesus macaque's body. The increased distance of the left-sided vessels to the nearest receiver coil, along with the increased room for respiratory motion on the left side, likely reduced measurement repeatability in these vessels.

While flow through the UtAs was relatively balanced in both the right and left UtAs, this was not the case in the OVs. Each rhesus macaque demonstrated a dominant OV, which carried the majority of blood from the uterus. While 11 of 15 rhesus macaques displayed dominance in their right OV, four monkeys showed a dominant left OV. This suggested the disparity in flow was more than a gravitational effect of the rhesus macaques being imaged in a right-lateral position. We hypothesize that the placentation site influences the flow loads in the two OVs. Unlike humans, who feature a placenta with a single disc, the rhesus macaque has two discs - one of which, the primary disc, is usually larger than the other, the secondary disc. It is possible that while uterine in-flow may initially be distributed relatively equally through the UtAs, some blood may be shunted through the uterine wall to supply the larger placental disc, as there is generally good anastomosis between the two sides. This could contribute to the imbalanced return blood flow.

Good agreement was also observed in vessel cross-sectional area measurements for both same-day and consecutive day measurements in the UtAs and OVs. The UtAs showed slightly better repeatability

than the OVs. This is consistent with prior findings in the cranial vasculature and is likely due to the differences in vessel wall distensibility in arteries and veins such that vein diameters and flow distribution is more sensitive to hydration levels, posture, and other factors [96]. These properties could be observed in the comparisons of PC MRAs across days in a single monkey, where the trajectory of the OVs showed noticeable changes with the motion of the fetus, while the UtAs showed minimal movement.

Quantitative flow assessment of fetal vessels and the umbilical cord proved to be dependent on the gestational age of the fetus. The fetal great vessels were reliably visualized at earlier stages of gestation than the umbilical vessels. The conservation of mass approach conducted in both the great vessels and on opposite ends of the umbilical cord showed good agreement in the great vessels but greater inconsistencies in the umbilical vessels. As with visualizing the UtVs and OSAs, it is likely that spatial resolution was the limiting factor of this application. In the 2nd trimester of gestation, the diameters of the fetal great vessels were typically 5-6 mm, while the umbilical vessels were 3-4 mm. Hence, given their larger diameter, the great vessel flow measurements were less susceptible to partial volume effects, resulting in better agreement than the umbilical vessel measurements and improved visualization earlier in gestation.

We believe this technique represents an improvement over previous attempts to characterize total uteroplacental flow with US and MRI. The ability to retrospectively place measurement planes on data-derived angiograms over a large imaging volume allowed for relatively simple placement of measurement planes orthogonal to the complex, tortuous geometries of many uteroplacental vessels. Dealing with this geometry is a major limitation with US, where challenges with properly aligning acoustic windows with these vessels may result in reduced accuracy. As a result, clinical US examinations do not attempt to image the even more variable venous return, which PC VIPR was able to quantify. In addition, using PC angiograms inherently derived from the data removed the need for a dedicated MRA acquisition, which was cited as the main limitation of previous PC MRI approaches [86,87]. The PC MRA here incorporated all acquired radial projections, which would not be possible with a Cartesian acquisition because of cardiac pulsatility artifacts. When compared to US, PC VIPR allows for more accurate characterization of flow, as it is directly measured rather than estimated from models. This enhanced accuracy may prove valuable in

identifying compromised flow dynamics in high-risk populations, and the ability to reproducibly assess flow as early as late first trimester, as demonstrated here, could aid in early diagnosis. Although PC VIPR was unable to consistently visualize the UtVs and OSAs, these results suggested this was because they were very small and contributed little to total uteroplacental flow. It remains to be seen if the ability to probe flow in these vessels will improve when PC VIPR is scaled up for use in pregnant human subjects, given the increased vessel sizes. Future studies will investigate whether OSAs have larger flow contributions in some subjects, possibly dependent on factors such as placentation site, or if they generally contribute little to total flow.

There were a few limitations with this study. The spatial resolution of the PC VIPR acquisition limited detection of smaller uteroplacental and fetal vasculature. Improvements in spatial resolution would come at the expense of prohibitively long scan times with questionable gains, as even the high-resolution, contrast-enhanced angiograms could not reliably depict the OSAs. The repeatability studies also had relatively small sample sizes and were not designed to completely eliminate outside influences on flow. The same-day acquisitions were not always completed back-to-back in the scanning protocol. Likewise, while scans on consecutive days were attempted to be scheduled at the same time of day, this was not always possible. These gaps between repeatability scans allow the possibility that flow may have been altered due to time-dependent factors such as natural physiologic variations or length of exposure to anesthesia between acquisitions. Such factors should be controlled for in any future longitudinal studies through consistent scheduling of imaging sessions and consistent pre-scan dietary protocols for volunteers.

The results of this animal study have been encouraging and translation to human studies is currently under investigation. The 4D flow sequence easily scales to the human anatomy and is low in specific absorption rate (SAR). Ferumoxytol, used here for MRA comparisons, is approved for human use as an iron supplement to treat iron deficiencies during pregnancy but not for imaging during pregnancy. In the rhesus model, sedation of the mother eliminated artifacts from gross maternal and fetal body motion and produced more consistent breathing patterns compared to non-sedated imaging in humans. While gating and coaching can be used to limit maternal motion in human subjects, fetal motion cannot be controlled.

The radial trajectory of PC VIPR reduces this sequence's sensitivity to motion [29], but measurements in the moving fetus will be challenging and the impact on image quality and measurement reliability cannot be extrapolated from this study.

3.5 Conclusions

4D flow imaging was feasible in the primary uteroplacental vessels by late 1st trimester and in the fetal vessels by mid-to-late 2nd trimester in the pregnant rhesus macaque. Flow measurements in the uteroplacental and fetal vasculature showed decent consistency and repeatability, but large limits of agreement suggested only substantial changes to uteroplacental flow induced by disease would be reliably detected in this animal model. Comparisons of PC angiograms against higher-resolution, ferumoxytol-enhanced angiograms showed similar depictions of the primary uteroplacental vasculature. These results indicate that 4D flow MRI with PC VIPR holds promise a valuable tool in assessing uteroplacental health, as it could simultaneously assess blood flow in multiple vessels, which could be further coupled with measurements of placental perfusion, oxygenation, and inflammation from complementary scans. Future studies will work on translating these techniques to pregnant human subjects and determining if measurement variability in such a population will allow for detection of clinically significant alternations to uteroplacental flow. Chapter 8 will discuss possible next steps for improving performance in more detail.

Chapter 4: Initial Experience with MRI Exercise Studies

4.1 Background

4.1.1 Exercise Stress Tests

It is well established that stress tests can reveal important diagnostic information beyond that seen with tests performed at a resting heart rate [64]. These tests can reveal ischemia, increased ventricular pressures, valvular regurgitation, and deficiencies in recovery to a resting state. Such conditions may be absent, or less apparent, at a resting heart rate. Clinically, exercise tests are commonly performed with a treadmill or stationary bicycle and imaged with echocardiography for function and flow measures [65] or nuclear imaging for perfusion measures [97]. These tests target elevating the subject's heart rate to a pre-designated level defined in one of several possible ways: a pre-defined exercise power protocol, a target heart rate, or a selected rate of oxygen consumption [67]. As discussed in Chapter 2, while stress echocardiography has been standardized and well-validated for left-heart analysis, echo imaging of the RV is less reliable given the anterior position of the ventricle in the chest [71]. This is a notable limitation in diagnosing and monitoring patients who suffer from right-heart diseases, such as pulmonary hypertension, or whole-heart conditions, such as congenital heart defects. Additionally, while bicycle stress tests can allow for ultrasound imaging during exercise, treadmill examinations are limited to post-exercise imaging where the subject must be repositioned following exercise. In these cases, the effect of the exercise is likely diminished at the time of measurement. Given that heart rate can decrease as much as 50 bpm for healthy subjects in this time, it is suggested imaging must be completed within a minute post-exercise [69,98] to avoid amelioration of exercise induced cardiac abnormalities. Exercise tests with nuclear imaging utilize radiotracers such as Thallium-201 in conjunction with a SPECT or PET camera to characterize perfusion in the myocardium. These tests cannot provide time-resolved images during exercise and expose the subject to very minor amounts of radiation.

4.1.2 MRI Stress Tests

There are many benefits to conducting exercise stress examinations with MRI instead of the modalities described above. MRI offers superior contrast and feature resolution compared to ultrasound and nuclear imaging, along with the capabilities to characterize both anatomy and physiology. The function measurements typically acquired with echo exams and the perfusion measures from PET/SPECT scans could be acquired in a single imaging session with MRI. MRI also does not have the inter-operator dependency found with ultrasound and is not limited to certain imaging windows as RF radiation is not appreciably attenuated in the subject's body. In the past, however, MRI studies under exercise conditions have been difficult to conduct given the narrow confines of the scanner bore, lack of MR-compatible exercise equipment, and absence of robust imaging sequences tailored to the unique requirements of imaging under exercise conditions. These unique challenges include the compensation of motion artifacts from respiratory and exercise motion and a temporal resolution fast enough to image at highly elevated heart rates. As a result, clinical stress studies with MRI instead historically rely on pharmacological agents, such as Dobutamine, Adenosine, and Regadenoson. Compared to pharmacological stress, however, exercise stress more closely resembles cardiovascular stress experienced during daily life and is the preferred form of stress for diagnosing chest pain, dyspnea, valvular disease, and pulmonary hypertension [69,99].

To accommodate exercise stress in MRI, a variety of solutions have been pursued. The Simonetti group at the Ohio State University has developed an MR-compatible treadmill that can be placed next to the magnet and mimic the setup of treadmill echocardiography studies to allow for exercise protocols with high workloads (Figure 4-1a) [100]. Following exercise, the workflow requires repositioning of the patient from the treadmill to the table, establishment of ECG gating, and scan initiation, which can be completed in 20-30 s with highly-trained support staff [101]. Combined with subsequent scan time, the measured exercise response can be diminished due to these delays. Other groups have shown that hand grip exercises are easily conducted and introduce very little patient motion (Figure 4-1b) [102,103], but the achieved exercise power is relatively low and not easily measured. A lab from Auckland developed a customized

MR-compatible cycle ergometer that is used in a supine position similar to bicycle echocardiography and allows for exercise in the bore during exercise with moderate workloads (< 200 W) (Figure 4-1c) [104].

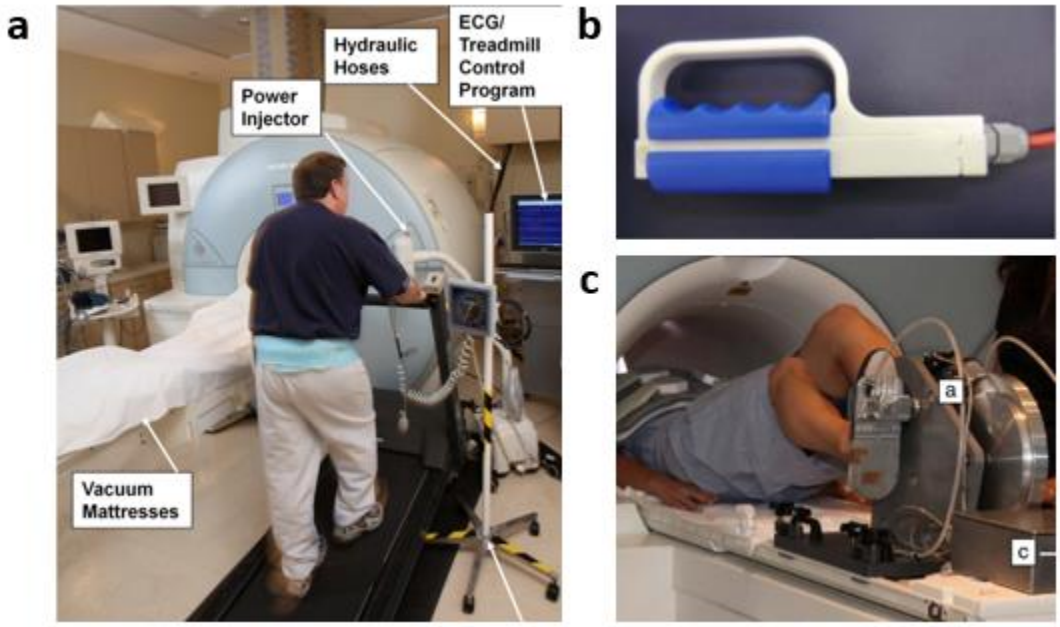

Figure 4-1: Early MR-compatible devices for MRI exercise challenges included (a) a retro-fitted treadmill, (b) resistance hand grips, and (c) a recumbent bicycle allowing for supine exercise in the scanner bore.

4.1.3 UW MR-Compatible Exercise Stepper

A group in the Biomedical Engineering department here at the University of Wisconsin-Madison developed a low-cost, custom-made MR-compatible stepper to allow for straightforward MRI exercise studies [105], herein referred to as the 'UW stepper.' This stepper is shown in Figure 4-2. To ensure MR-compatibility, the UW stepper is made of a high-density polyethylene, aluminum, brass, and other nonferrous materials. Stepping resistance is determined by removable nonferrous tiles placed in boxes at the end of each lever arm, allowing for discrete adjustment of resistance. An optical sensor in the base of the equipment tracks the rate of stepping during exercise. This information is sent to a computer in the MRI control room, allowing for real-time feedback of stepping cadence and exercise power.

Figure 4-2: Low-cost MR-compatible stepper developed at the University of Wisconsin-Madison. Subjects exercise via a dynamic stepping motion in a supine position in the MRI bore. Resistance is determined by removable weights included in the boxes at the end of each lever arm.

As shown, the UW stepper attaches to the MRI bed and allows subjects to exercise in a supine position in the magnet bore. This allows for necessary scan calibration to be performed prior to exercise, allowing for immediate scanning during, or following the cessation of, exercise. To minimize bulk displacement from exercise between pre-scans and imaging, the subject is connected to the base of the stepper via a backpack harness and has two handles to hold. This is effective at preventing the subject from pushing backwards while stepping against higher resistances. This equipment was designed to be compatible with the 1.5 T HDxt MRI scanner (GE Healthcare, Waukesha, WI).

4.2 Exercise CMR Feasibility in Patients with Pulmonary Arterial Hypertension

To assess the feasibility of using the UW Stepper in conjunction with product pulse sequences available on most MRI scanners for exercise cardiovascular magnetic resonance imaging (CMR), a small exercise study was attempted in a patient population with pulmonary arterial hypertension and comparable control groups.

4.2.1 Study Background

Cardiopulmonary exercise testing is increasingly used to assess disease progression in patients with pulmonary hypertension (PH) [106–108]. PH is characterized by an increase in blood pressure in the pulmonary vasculature, which can be caused by or result in vascular remodeling and stiffening of the

pulmonary artery [109,110]. PAH is particularly well-suited for assessment with exercise CMR, as it has significant impact on the right-heart, which is not adequately served by stress echo examinations due to increased beam attenuation. In addition, exercise stress has been identified as the preferred method of stress for diagnosing and assessing pulmonary hypertension, rather than the pharmacological agents typically used with MRI stress exams [69,99].

While some cases of PH are the end result of left-sided heart disease that directly influence systemic circulation (World Health Organization (WHO) functional group 2) [111], pulmonary arterial hypertension (PAH; WHO functional group 1) is the result of conditions, such as connective tissue diseases, acting directly on the pulmonary vasculature [112]. In these cases, although there is no initial left-heart dysfunction, right ventricular pressure overload induced by PAH can lead to a shift or distortion of the intraventricular septum [113–115]. This may lead to a reduced left ventricular (LV) volume in PAH patients relative to a healthy population, which in turn may lead to diminished stroke volume (SV) and cardiac output (CO).

Overall, while it is likely that a patient diagnosed with PAH will experience diminished left-heart function due to right ventricular pressure overload during the progression of the disease, such effects have not been investigated in detail with exercise MRI. Previous work has performed straightforward comparisons of blood flow in the aorta of PAH patients with controls using PC MRI [116], but has not correlated these measurements with metrics of vessel stiffness or investigated the value of exercise studies for these comparisons. The goal of this study was to use a custom-made, MRI-compatible exercise device to examine the feasibility of performing exercise CMR with product sequences to evaluate the effects of PAH on left-heart function. We hypothesize that PH subjects will show reduced left-heart efficiency (lower stroke volume, higher heart rate) relative to healthy controls and these differences will be more pronounced following exercise stress.

4.2.2 Methods

This study was approved by the local Institutional Review Board and was compliant with the Health

Insurance Portability and Accountability Act. Twenty-one subjects were recruited, provided written informed consent, and were screened via an MRI safety questionnaire. The 21 subjects were divided into 3 cohorts: 7 young, healthy controls (28 ± 4 years; 3 male, 4 female), 8 older, healthy controls (58 ± 10 years; 1 male, 7 female), and 6 pulmonary hypertension patients (WHO Group 1 (PAH) from systemic sclerosis, 60 ± 9 years; 1 male, 5 female). All control subjects were free of overt cardiovascular, pulmonary, and renal disease. The recruited PH subjects had no recent syncope and, like the controls, had no history of unassociated lung or cardiovascular disease. Exclusion criteria for this study included classification as New York Heart Association functional class IV (symptoms of limited cardiac capacity apparent at rest) and skeletal or muscle abnormalities which could prohibit exercise. The older, healthy control group was age-matched to the PH group. The younger control group was included to provide insight regarding loss of cardiac function via disease versus natural loss due to aging. Subjects were excluded from the final statistical analysis if image quality was too poor to delineate the aortic wall and LV boundaries or if the subject moved out of the prescribed scanning planes during exercise.

Imaging was performed on one of two clinical 1.5 T MRI systems (HDxt or Discovery 450w, GE Healthcare, Waukesha, WI) using an 8 channel cardiac coil and vector electrocardiographic (ECG) gating. Flow measurements were acquired with a prospectively ECG-gated 2D cine PC sequence performed across a 15 s breath hold. The imaging plane was prescribed orthogonal to the ascending aorta. Imaging parameters for the PC sequence were: field of view = 35 x 35 cm, matrix size = 128 x 256 (reconstructed to 256 x 256), slice thickness = 8 mm; TR/TE = 6.1/3.7 ms, flip angle = 30°, velocity encode (VENC) = 150 cm/s, parallel-imaging (ASSET) acceleration factor = 2, temporal resolution = 25 ms, and cardiac phases = 20. Cardiac function measures in the left ventricle were acquired with an ECG –gated investigational 3D Cartesian balanced steady-state free precession (bSSFP) sequence (kat-ARC) [117]. This sequence utilized parallel imaging and exploited spatiotemporal correlations to allow for whole-heart coverage within an 18 s breath hold. Slices were acquired in a short-axis orientation. Imaging parameters for the bSSFP sequence were: field of view = 36 cm x 29 cm, matrix size = 180 x 180, slice thickness = 8 mm, number of slices = 16, TR/TE = 3.4/3.1 ms, flip angle = 45°, net acceleration factor = 8.

Exercise was performed in a supine position in the scanner bore with the UW stepper. All subjects exercised at a low exercise power to guarantee the PH subjects would be able to complete the same exercise paradigm as the control groups. This exercise and imaging paradigm was designed to induce mild-to-moderate exercise stress in all subject groups (Figure 4-3). PC and bSSFP acquisitions were performed at rest prior to exercise. Subjects then exercised at a target power of 30 W for 3 minutes. Within a few seconds following the end of exercise, subjects held their breath for a PC MRI acquisition. This was followed by an additional minute of exercise at the same power to account for the drop in heart rate during the rest period of the PC scan. The breath-held bSSFP scan followed the cessation of the extra minute of exercise.

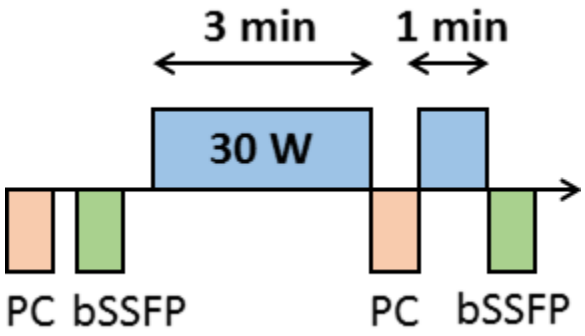

Figure 4-3: Exercise and imaging paradigm for all three groups. PC and bSSFP imaging was performed in the ascending aorta and LV, respectively, at rest. This was followed by 3 minutes of exercise at an exercise power of 30 W. PC imaging immediately followed the end of exercise. An additional minute of exercise at 30 W was performed to compensate for the recovering heart rate and a bSSFP scan was performed.

Aortic flow measurements were performed with CV Flow (Version 3.3, Medis, Leiden, Netherlands) and LV volume measurements were made with MASS viewer (Version 5.4, Medis, Leiden, Netherlands) on a GE Advantage workstation. The following parameters were calculated from the flow measurements: SV, CO, peak systolic flow (PSF), and the relative area change (RAC) of the ascending aorta between diastole and systole. Aortic stiffness was estimated with relative area change rather than pulse wave velocity due to the limited temporal resolution of the PC sequence. For LV volume measurements, parameters of interest were SV, CO, and ejection fraction (EF). All parameters were

measured at baseline and immediately following exercise stress. The consistency of SV measurements from the flow and function measurements were compared at rest and stress in each subject to examine the impact of exercise motion on our measurements.

All statistical analysis was performed with R (Version 3.2.3, R Foundation for Statistical Computing, Vienna, Austria). Continuous variables are presented as the mean value plus or minus one standard deviation of the sampled group. To determine the statistical significance of any intragroup changes between parameters measured at rest and stress, a paired student's t-test was performed for each cohort. A one-way ANOVA test with a post-hoc Tukey's honestly significant difference (HSD) test was used to determine statistically significant intergroup differences for each parameter at rest and stress. Levene's test was used in conjunction with the ANOVA test to ensure that the assumption of equal variances between groups was valid. For all statistical tests, a threshold of $\alpha = 0.05$ was chosen for statistical significance.

4.2.3 Results

MRI exercise stress tests were successfully performed in 19/21 subjects. Two of the older, healthy controls shifted their body position during exercise such that the prescribed scan planes were not usable. Thus, they were omitted from the analysis. Although the target exercise power for each group was 30 W, the actual exercise power achieved for the remaining young controls, older controls, and PH subjects was 38 ± 12 W, 32 ± 8 W, and 30 ± 10 W respectively. There was no statistically significant difference in the achieved exercise power between these groups ($p = 0.29$). These exercise powers resulted in an average heart rate increase of 46% for the young controls, 29% for the older controls, and 74% for the PH subjects.

Fig. 4-4 shows a representative comparison of image quality in magnitude PC images and bSSFP images before and immediately following exercise. Noticeable motion artifacts were observed in post-exercise images, especially in the bSSFP acquisitions. PC images showed signal loss in the ascending aorta. Increased blurring was observed in the PH subjects relative to the control groups.

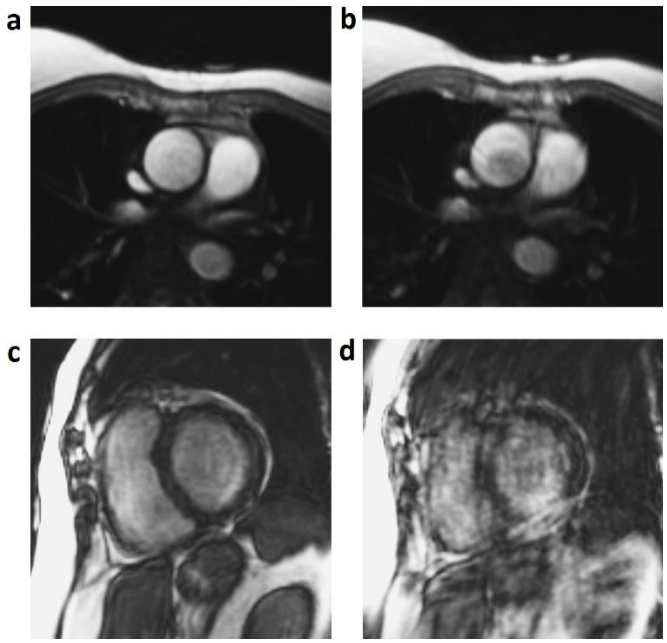

Figure 4-4: Influence of motion artifacts on image quality in magnitude PC images (a) at rest and (b) following exercise and bSSFP images (c) at rest and (d) following exercise.

The data distributions for SV, CO, PSF, and RAC are visualized at rest and following stress for all cohorts in Figure 4-5. Statistically significant increases in heart rate and CO following exercise, indicated that the mild exercise paradigm was able to induce a cardiac response in all cohorts. On average, SV in the PH subjects were 30% lower than the young controls and 28% lower than the older controls at rest, and 23% lower than the younger controls and 32% lower than the older controls following exercise. Interestingly, however, PH subjects demonstrated a resting CO approximately 30% lower than their healthy counterparts, while mean CO measurements were comparable amongst all groups following exercise (Figure 4-5b). Measurements of PSF showed no meaningful response to exercise in the young control groups. In contrast, the older controls showed a 19% increase in velocity and an 11% increase in flow in response to exercise. Likewise, the PH subjects demonstrated a larger 39% increase in velocity and 26% increase in flow. At both rest and exercise, the PH subjects demonstrated lower overall average values of PSF when compared to both control groups (Figure 4-5c).

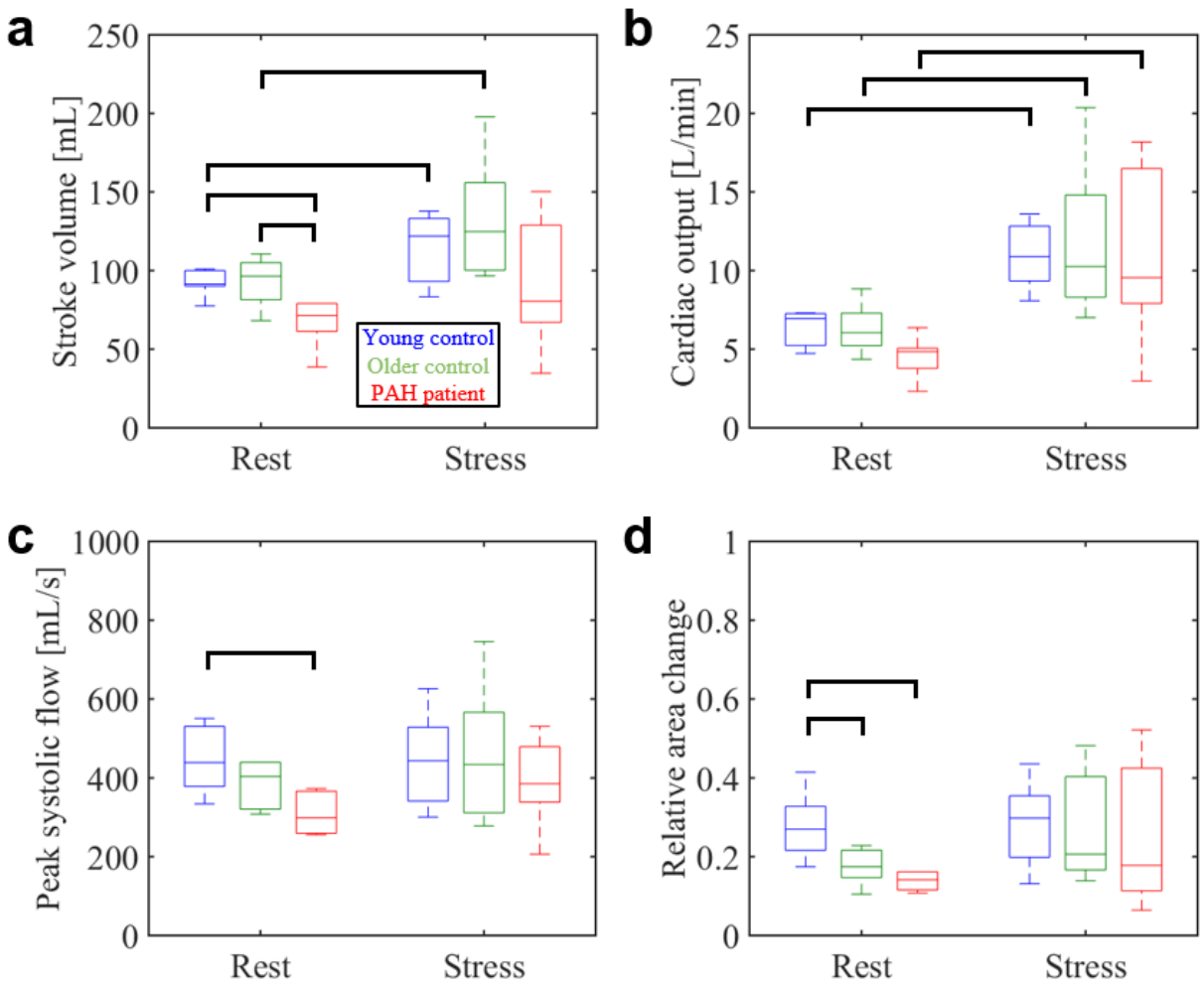

Figure 4-5: Distributions of (a) stroke volume, (b) cardiac output, (c) peak systolic flow, and (d) relative area change in all three cohorts as measured with a breath-held 2D PC acquisition. A bracket between two boxplots denotes a significant difference between the two distributions.

Significantly lower values of RAC in the older controls and PH subjects relative to the young controls at rest indicated stiffer aortic walls in these groups (Figure 4-5d). The PH subjects had the lowest mean RAC of all groups, suggesting the stiffest vessel walls amongst the three cohorts. Although not significant, exercise showed increased vessel compliance of the older controls and PH subjects to the level of the young controls. Overall, measurements for all hemodynamic parameters following exercise usually showed more variance amongst each cohort than at rest.

Figure 4-6 shows the distributions for SV, CO, and EF as determined from the LV volume measurements from the bSSFP acquisitions. The function measures did not display the same increase in SV with exercise that was found in the flow measurements (Figure 4-6a), but statistically significant increases in cardiac output were still observed for the younger controls and the PH subjects (Figure 4-6b). Ejection fraction did not appear to be strongly affected by the exercise stress with these measures (Figure 4-6c). A closer analysis of SV revealed that there was a relatively good agreement between flow and functional stroke volume measures in each subject at rest (Figure 4-7a), but this agreement was not present in the acquisitions following exercise, where the stroke volume measures were shown to be consistently lower in the bSSFP measurements (Figure 4-7b).

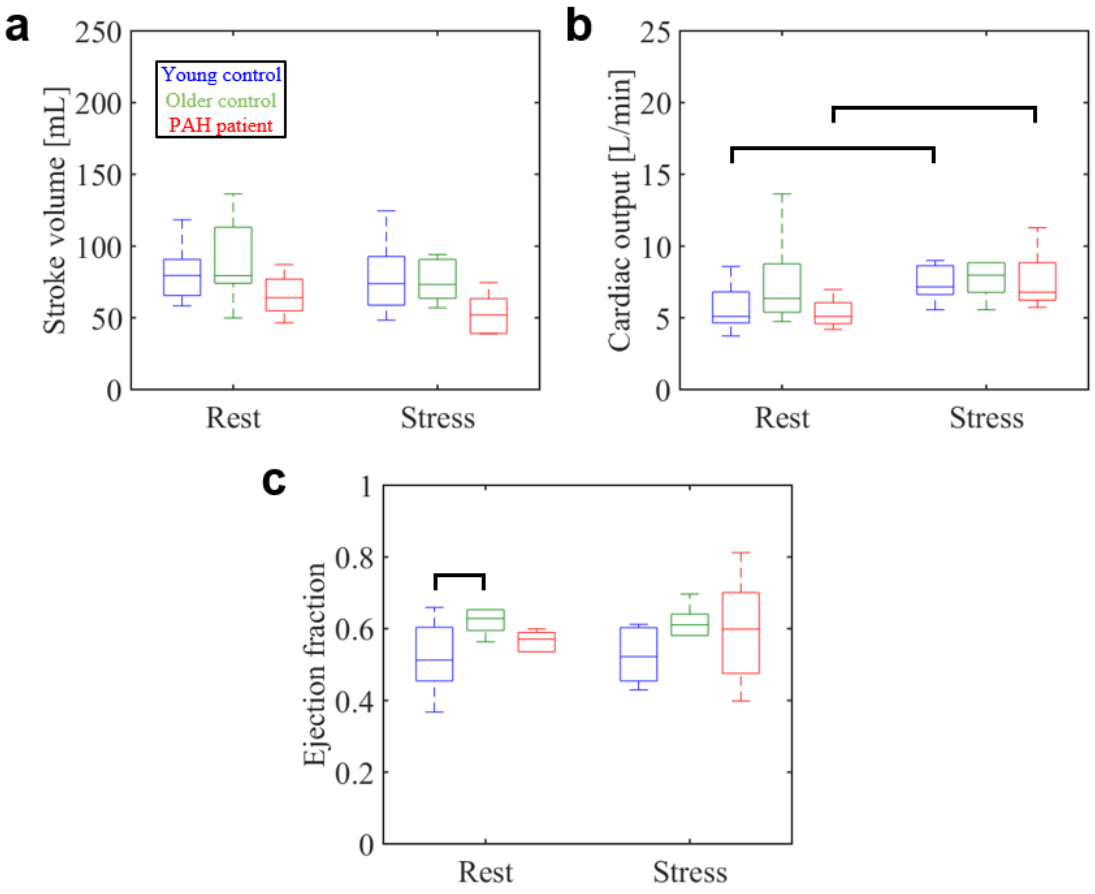

Figure 4-6: Distributions of (a) stroke volume, (b) cardiac output, (c) ejection fraction in all three cohorts as measured with a breath-held whole-heart bSSFP acquisition. A bracket between two boxplots denotes a significantly significant difference between the two distributions.

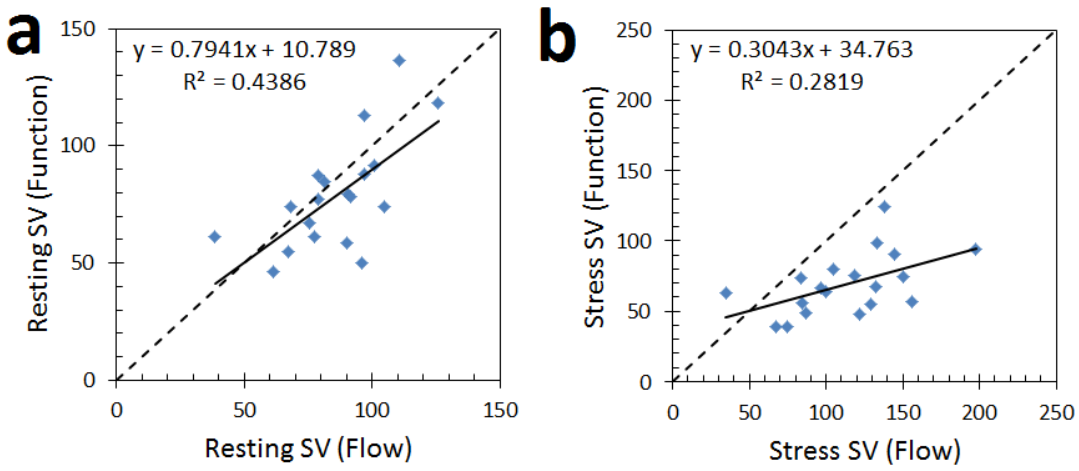

Figure 4-7: Stroke volume measures obtained via flow measurements vs. those from function measurements for each subject at (a) rest and (b) stress.

4.2.4 Discussion

The modest increase in heart rate observed across all three subject cohorts validated that the relatively low exercise power used in this study was still effective at inducing observable exercise stress in each cohort, although the cardiac response was diminished in the control groups. This demonstrated that mild exercise paradigms can be an effective method for stress imaging in subjects with reduced cardiac capacity. The drawback of using low exercise powers was observed in the younger controls, however, who were not as challenged by the paradigm and, on average, exercised at a power 25% above the targeted level. Since the resistance could be adjusted in real-time during exercise with the exercise equipment used for this study, in this case, where the young controls exercised faster than this metronome beat, there was no way to compensate and reduce their exercise power.

As hypothesized, PH patients demonstrated reduced LV stroke volume at rest and during stress when compared to control groups. These reduced stroke volumes may suggest the presence of a shifted intra-ventricular septum induced by right ventricular pressure overload. Despite low stroke volumes, however, the PH patients presented a preserved cardiac output following exercise as a result of a compensatory increase in heart rate (74% increase in PH subjects as compared to 29% in age-matched

controls). Therefore, while PH patients may be able to match exercise capabilities of age-matched controls in the short-term, the more rapid increase in heart rate will result in PH patients reaching a clinically-defined maximum heart rate sooner, yielding reduced exercise endurance. This behavior in the left ventricle is consistent with right heart dynamics previously reported following exercise in patients with PH [118]. While there was good agreement in SV measurements between the PC and bSSFP acquisitions at rest, the correlation was poor following exercise. This was due to a combination of large variance in the PC measurements and no measurable increase in the bSSFP volume quantification, suggesting both of these sequences have fundamental limitations when imaging following exercise stress.

Although the exercise stress induced comparable levels of cardiac output in the PH population and both control groups, the PH subjects demonstrated reduced peak systolic flow – further evidence of altered left heart function induced by right heart changes from PAH. It is worth noting, however, that for these parameters the older control group showed decreased mean values relative to the younger group as well, suggesting the reduced capacity shown in the PH subjects may be a more complex dynamic between natural age-related loss of cardiovascular function and disease progression.

The relative area change of the aorta proved to be capable of assessing vessel stiffness, demonstrating reduced aortic compliance in the PH subjects relative to the controls. This result was consistent with both the reduced exercise capacity of the PH subjects and the fact that the recruited subjects developed the condition as a result of ongoing systemic sclerosis [119]. There is great value in future investigations to perform non-invasive measures in the pulmonary artery of the PH subjects to examine the extent of stiffening relative to the aorta.

The potential value of performing exercise studies in a PH population was apparent, as the PH cohort showed larger relative responses to exercise than the healthy controls in all measured hemodynamic parameters except stroke volume, which is known to have a reduced response to exercise in PH subjects [118]. Outside of HR and CO, however, many parameters expected to have significant increases with exercise, such as PSF and EF, showed limited responses. Performing studies with increased exercise power may induce greater differences than observed with the mild exercise powers used in this study. Given the

disparity in exercise abilities between these cohorts, in future studies, it would be valuable to standardize our comparisons on more physiologic measures of exercise, such as a common heart rate or maximal oxygen uptake (VO_{2max}), rather than a common exercise power. Studies with increased exercise powers would be challenging to perform with the UW stepper, as its design is naturally unstable given its high, and constantly changing during exercise, center of mass. As such, for maximal safety, exercise powers above 70 W are not recommended, limiting studies with this equipment to modest exercise challenges.

There was limited sensitivity in assessing inter-cohort differences in the image acquisitions post-exercise, as a result of increased variance in these measurements. Decreased image quality from the presence of significant motion artifacts was likely a large contributor to this large variance. The bSSFP cardiac function images proved to be much more prone to motion artifacts than the PC acquisitions. Severe blurring and streaks were observed in the post-exercise images, likely due to large respiratory motion from incomplete breath holds during the acquisition. This made segmentation of the myocardial wall challenging and may be responsible for the consistent underestimation of LV volume in the acquisitions following exercise. We hypothesize that the decreased post-exercise image quality relative to the PC MRI is a product of the longer breath hold required for the cardiac function scans. Extended breath holds were found to be quite challenging immediately following exercise for some of the subjects, especially the PH group. The kat-ARC acquisition used for the LV volume measurements also exploited expected spatiotemporal correlations in the data which likely resulted in reduced reconstructed image quality in the presence of unexpected respiratory motion. The implementation of free-breathing or real-time acquisitions could present an increase in image quality, especially in the cardiac function images, and result in a more comfortable exercise paradigm for subjects. Such techniques may even allow for image acquisition during exercise, eliminating the additional minute of exercise between the PC and bSSFP scans as a possible source of variability in our measurements. Although more challenging for these subjects, it was essential to begin imaging immediately following exercise due to the rapid recovery of heart rate back to a resting state. The potential heart rate recovery across the image acquisitions following cessation of exercise was not deemed to be a concern, however, as a previous study showed that even in young athletes, heart rate will only

decrease an average of 5% in this time period [98].

There were a few limitations to this study beyond those already mentioned. The harness used to reduce chest motion was not entirely effective at preventing subject movement, as demonstrated with the two subjects who moved out of their prescribed scan planes. Motion such as this possibly led to shifts or rotations in scan planes in the other subjects, which could impact the accuracy of flow and vessel cross-sectional area measurements. In addition to this, since the stepping resistance with the UW Stepper is determined by discrete intervals of removable weights, once exercise has begun, the resistance cannot be changed. As a result, subjects must continuously change their stepping cadence if they are to perform graded exercise challenges. This requires continuous monitoring and coaching during the exercise challenges, and if the subject deviates from the target stepping cadence, the resistance cannot be adjusted in real-time to compensate and maintain a target exercise power. Finally, the statistical power of our observations was limited by the relatively small sample size of each cohort. These factors likely contributed to increased variance and lack of statistical significance in some of the measurements.

4.2.5 Conclusions

We investigated the impact of mild exercise stress on aortic flow and LV function in healthy controls and subjects with PAH using a novel custom-made, MRI-compatible exercise device. This equipment permitted subjects to exercise in a supine position fully in the bore of the scanner, allowing for imaging immediately following the cessation of exercise. PC images demonstrated superior image quality to the bSSFP images, presumably due to the shorter breath hold associated with the scan. Overall, stroke volume and cardiac output appeared to be the parameters showing the greatest response to exercise stress. As we hypothesized, the PH subjects showed reduced LV stroke volume and increased aortic stiffness relative to the healthy controls. While this study demonstrated the potential value in using exercise CMR in patient populations, it was hampered by some notable limitations: (1) the UW Stepper was not capable of the high-power, multi-stage exercise challenges needed to induce noticeable differences and improve sensitivity between subject groups and (2) traditional breath-held pulse sequences were too susceptible to motion artifacts, even when

imaging was conducted post-exercise, to allow for reliable quantification in stress images. The work presented in Chapters 5 and 6 will focus on addressing these two main limitations.

Chapter 5: Implementation of High Power MR-compatible Exercise Equipment

5.1 Ergospect Stepper

In response to the limitations of the UW stepper, a commercial MR-compatible stepper was acquired to conduct MRI studies at the UW during exercise: the Cardio Step Module (Ergospect Medical Technology, Innsbruck, Austria), herein referred to as the 'Ergospect stepper' [120]. This device is shown in Figure 5-1a and 5-1b.

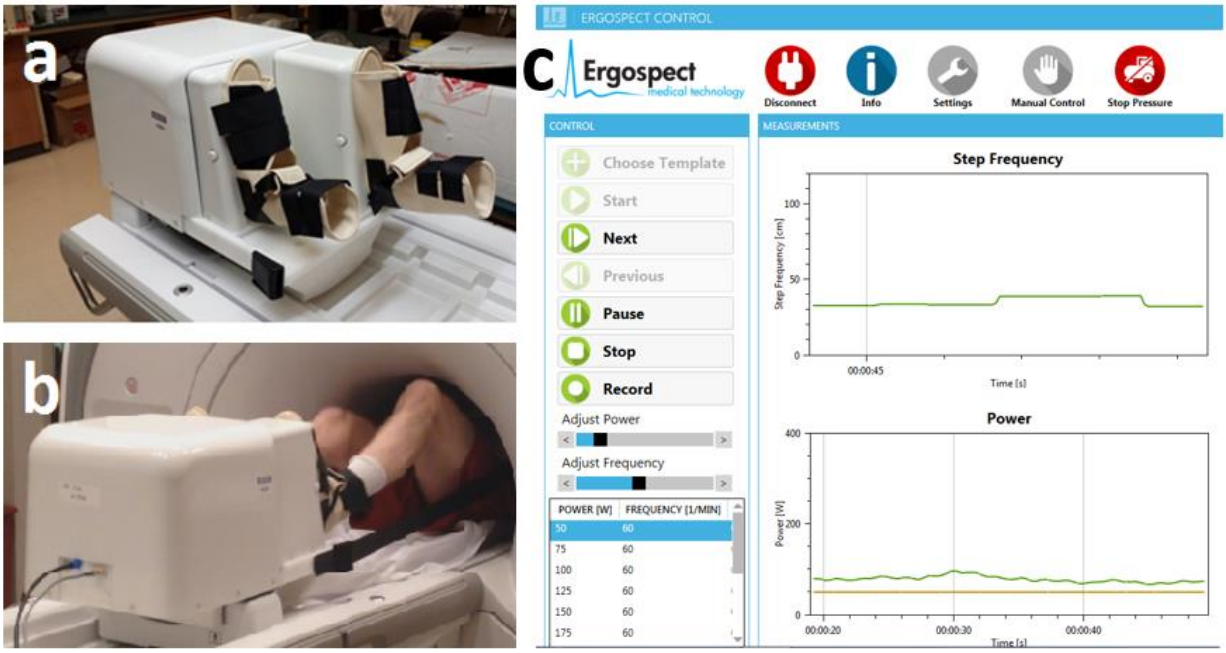

Figure 5-1: Ergospect stepper. (a) Built-in boots allow subjects to attach their feet to the end of pneumatic pistons through a natural stepping motion which (b) can be performed in the MRI scanner bore. (c) Software on a dedicated computer in the MRI control room allows for continuous monitoring and adjustment of exercise powers.

Like the UW stepper described in the previous chapter, this equipment allows subjects to exercise fully in the bore of the MRI scanner. To exercise with the Ergospect stepper, the subject steps against pneumatic

pistons, whose resistance is regulated by the internal air pressure. This pressure can be controlled, monitored, and recorded remotely in real-time from a computer in the MR control room (Figure 5-1c), allowing for adjustments to exercise protocols without the need to stop exercise and make physical changes to the equipment. Exercise protocols can be prescribed on this computer to allow for automated multi-stage exercise protocols. The exercise power is determined by this continuously adjustable resistance and the frequency of the subject's stepping motion, as recorded by force sensors in the stepper. A metronome beat instructs the subjects how quickly to step, but if the subject deviates from this beat, the pressure to the exercise device will automatically adjust to compensate and maintain the power originally prescribed in the exercise protocol. To minimize the motion of the subject during exercise, the subject is attached to the stepper via boots with Velcro straps and a chest harness (a vest connected to the stepper with detachable backpack straps) that prevents the subjects from pushing back away from the device during exercise. The chest harness also stabilizes the chest, so coil motion is minimal during exercise. To ensure the device remains stable during intense exercise, vacuum pads on the bottom creates a strong seal with the MR table, minimizing rotational motion from the alternating torque of the stepping motion. With this set-up, scans can be started during exercise. The Ergospect stepper is capable of exercise powers as high as 400 W, which, in our experience, only extremely fit subjects can achieve for an extended period.

5.1.1 Hardware Modifications

The Ergospect stepper features a modular design in which different base plates can be swapped out, allowing for compatibility with different MRI scanners. This equipment, however, was originally created to be compatible with Siemens scanners, which feature immobile scanner tables, and thus, feature great stability. This stepper was the first ever designed for use with GE MRI scanners and the first in North America. It was designed entirely from engineering drawings without an actual GE system to test it on. Many GE scanners feature tables on caster wheels which make them more prone to motion, even when they are attached to the scanner. As a result, some hardware re-designs were necessary for optimal compatibility of our stepper's base with the scanners at the UW-Madison.

The Ergospect stepper was designed for compatibility with the Discovery MR750 3.0 T scanner (GE Healthcare, Waukesha, WI) in the WIMRMR2 suite. When the stepper was received, it featured a design in which the front of the stepper connected via vacuum seal to the surface of the scanner bed, while the body of the stepper sat elevated on the lip of the table, partially protruding over the edge (Figure 5-1b). Due to this geometry, when subjects exercised, the force of their stepping motion, coupled with the already heavy weight of the stepper, produced a noticeable torque on the point where the stepper was vacuum-sealed to the scanner bed. This had two significant impacts on the feasibility of exercise studies with this device. First, at exercise powers above 100 W the equipment would rock back and forth as the subject stepped. With some of the energy from exercise resulting in bulk stepper movement instead of just the movement of the pneumatic pistons for each leg, the device would register lower exercise powers than were occurring. This would result in more difficult exercise challenges than were prescribed. Second, at higher exercise powers the torque on the table resulted in a repetitive flexing of the end of the MRI bed. It was feared that this repetitive load cycling on the end of the MRI bed could result in material fatigue and eventual failure.

To address these concerns, extensive time was spent consulting with Ergospect to assist in developing a new base which would allow exercise powers as high as 400 W to be achieved at no risk to the scanner hardware. The new design agreed upon involved moving the stepper forward up the table so it was no longer elevated with respect to the subject or protruding over the edge. This set-up involved the removal of the distal coil panel on the MR table and the implementation of a new base that sits flush with the contours of the coil slots. The new stepper base is shown in Figure 5-2a. An additional vacuum seal was also added to improve stability. Since this new base involves the exercise equipment sitting farther up on the table, however, studies with head coils are no longer possible and the maximum subject height for use with this device is approximately 6’3”. This was deemed an acceptable trade-off for this redesign, as according to recent data from the National Center for Health Statistics, less than 5% of the male population in the U.S. are taller than 6’3” [121], and the focus of these studies was on cardiac imaging.

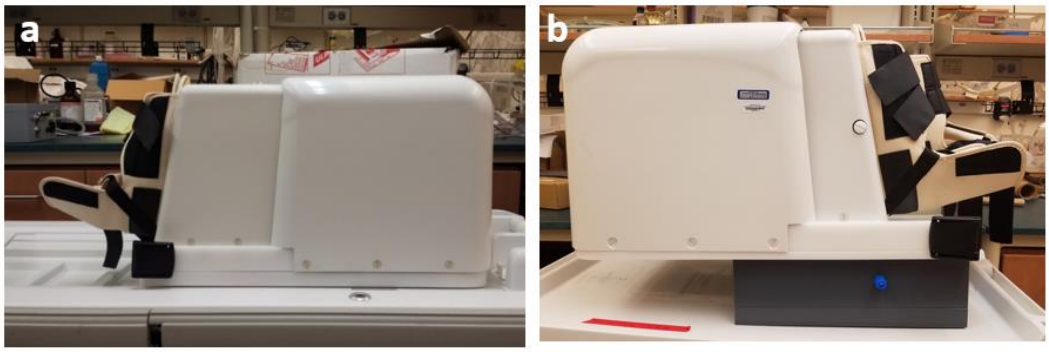

Figure 5-2: New Ergospect stepper bases for compatibility with (a) Discovery 750 scanner and (b) PET/MR scanner.

The implementation of this new base resolved the issues with stability and table flexing and has allowed for safe exercise on the MRI bed at exercise powers up to 400 W. Since then, collaborators in the Eldridge laboratory in pediatrics have commissioned a second base for compatibility with the PET/MR scanner. This base is shown in Figure 5-2b.

5.1.2 Software Calibrations

One of the most desirable features of the Ergospect stepper is its ability to continuously change the stepping resistance through regulation of the air supply to the device. This allows both for staged exercise challenges and consistent exercise work rates in the presence of variable stepping cadences. To achieve this, internal force sensors must provide accurate measurements of stepping frequency to the control software so piston pressures can be adjusted accordingly.

Initial testing of the Ergospect stepper, however, showed inaccurate and imprecise calibration. An example of this can be seen in Figure 5-3a. This example shows the measured exercise response by one subject to the same exercise challenge on three different occasions. Each iteration showed drastically different power profiles over time inconsistent with the prescribed exercise power, and all lacked the discrete power changes fundamental to the exercise paradigm.

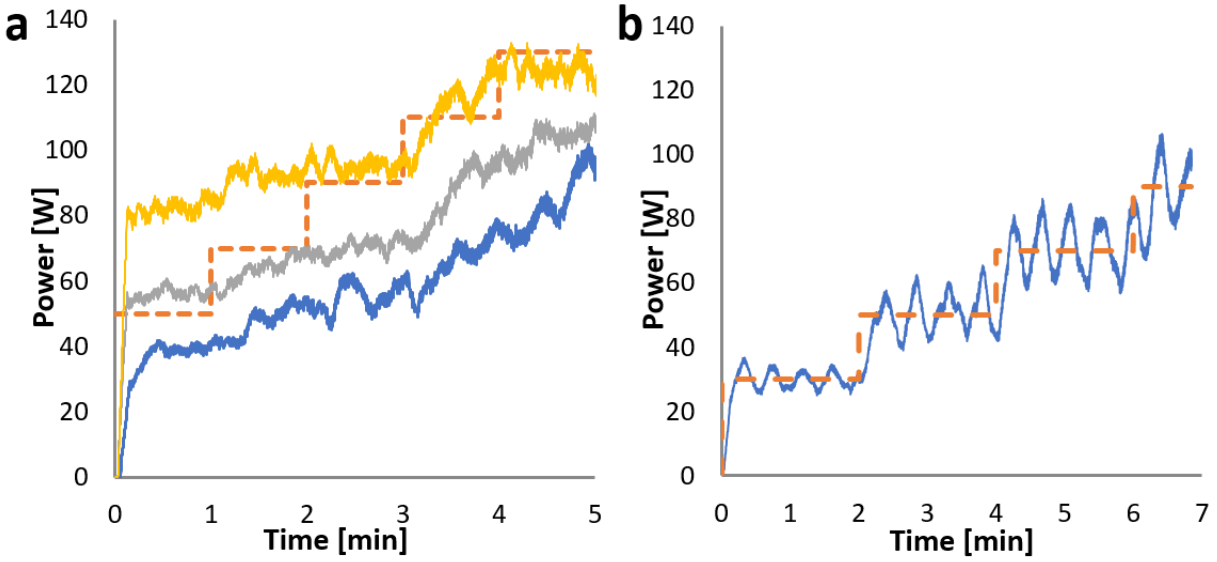

Figure 5-3: (a) Measured exercise responses with initial calibration. The dashed line represents the prescribed exercise power, while the three colored curves indicate the measured exercise power achieved on three separate occasions by the same subject. (b) Measured exercise responses following software update provided by Ergospect.

To address this lack of accuracy, Ergospect provided a software update to improve calibration. Figure 5-3b shows a comparison of measured exercise power vs prescribed exercise power with this new software revision. While there was a noticeable improvement in power accuracy for the lower exercise powers shown here, the new update introduced sinusoidal power fluctuations around the target exercise work rate. The reason for these fluctuations are a function of hardware limitations. Due to the nature of the pneumatic valves used in this equipment, the system experiences hysteresis. This meant that the stepper featured different pressure/power curves for increasing or decreasing resistance, as shown in Figure 5-4. The blue curves in the top plot represent the original pressure/power curves as hard-coded in the software.

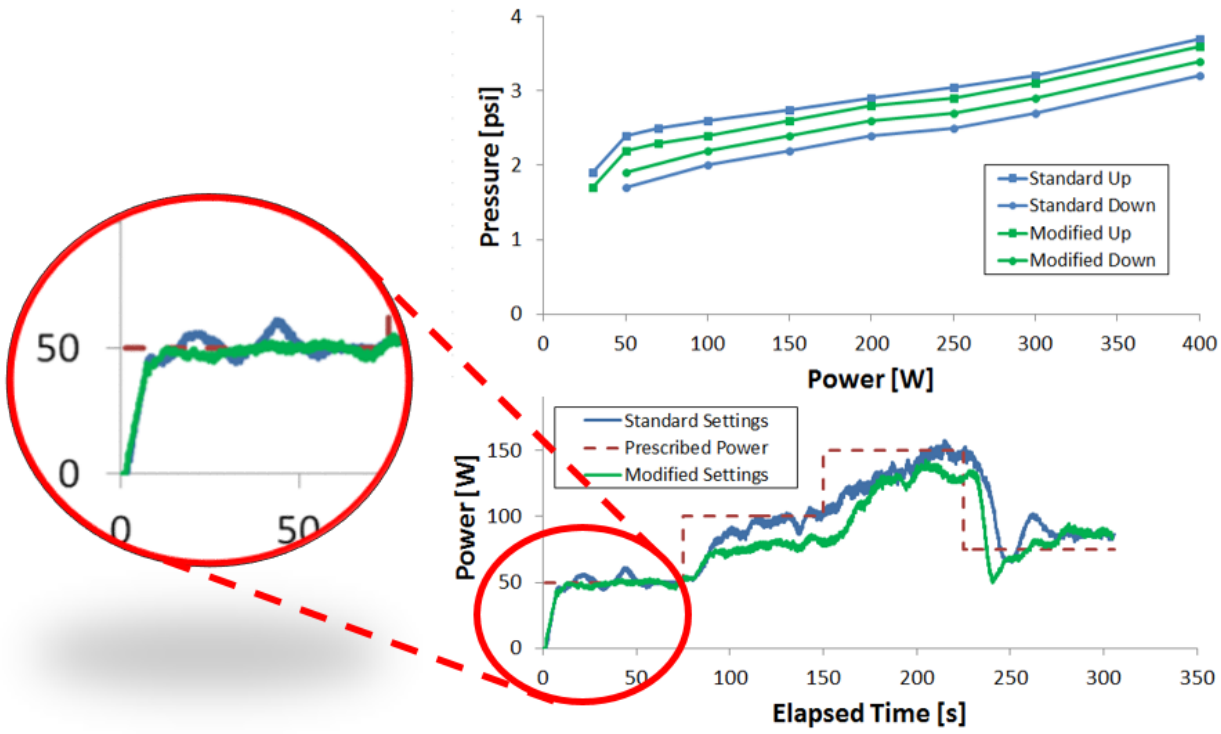

Figure 5-4: Top: The original pressure/power curves for stepper are given in blue, while the modified curves are in green. Bottom: The effects on these different curves on the achieved exercise powers are shown for a pre-defined exercise protocol.

To address the sinusoidal power response, the power/pressure curves in the software were modified and the threshold at which the equipment began automatically adjusting the power was reduced. By default, the automatic adjustment only activated when the subject deviated at least 10% from the prescribed power. This threshold was reduced to 5% to allow for more frequent adjustments to the power. In addition to this, the large pressure gap between the ascending and descending pressure/power curves was reduced, as shown by the new curves in green, to decrease the magnitude of pressure changes for each adjustment. As shown by the blown-up portion of the bottom plot in Figure 5-4, the changes to these parameters resulted in successfully eliminating the sinusoidal fluctuations for low exercise powers. The delay time in which the software detected power variations from the prescription and corrected these discrepancies was also reduced to improve performance. This is most apparent in Figure 5-4 where the modified power curve in green responded faster to the drop in the prescribed exercise power from 150 W to 75 W.

5.1.3 Frequency Sensor Inaccuracies

Although the software modifications represented an improvement in device accuracy at low exercise powers, there were still noticeable inaccuracies in achieving exercise powers above 100 W. Continued modifications to the hard-coded calibration were unable to resolve these issues, and through discussions with exercise subjects, it was learned that many subjects noted resistance changes dependent on the stepping motion they exercised with. Upon further investigation, it was observed that when subjects took shallow steps, the Ergospect stepper recorded accurate stepping frequency profiles, yet when subjects took full steps (utilizing the full dynamic range of the stepper), the device would record grossly inaccurate frequency. This can be visualized in Figure 5-5, where a single subject exercise with shallow steps for half of an exercise challenge and full steps for the other half, all while maintaining the same stepping frequency. These results suggested the remaining software calibration issues may be rooted in hardware limitations.

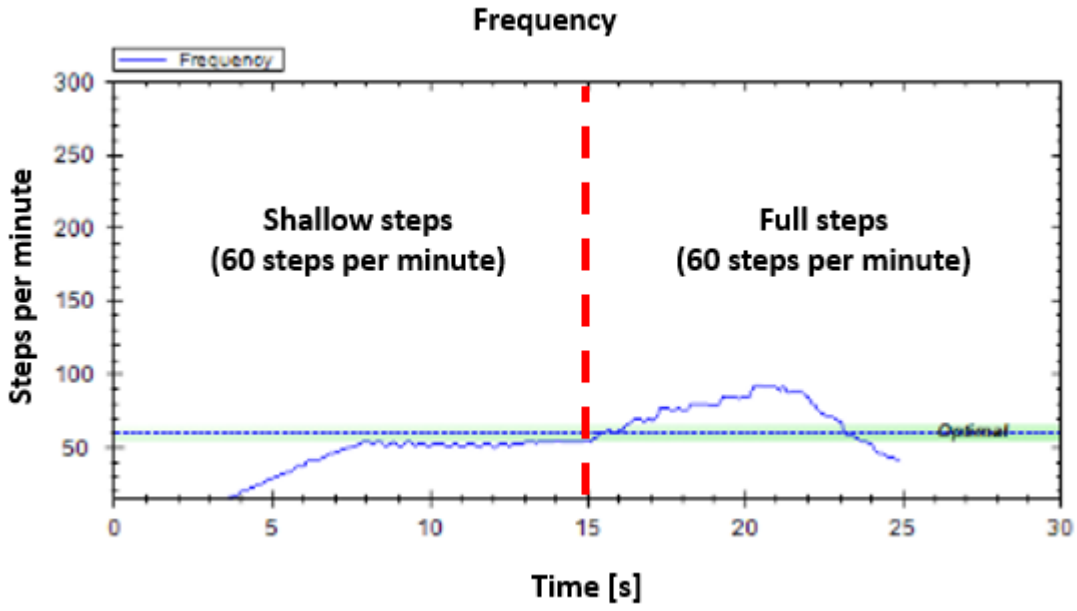

Figure 5-5: Measured stepping frequency for a single exercise trial where the subject took shallow steps for the first 15 seconds and full steps for the remaining time. Both stepping techniques were performed at a cadence of 60 steps per minute.

To understand what was causing these discrepancies based on stepping motion, the cover of the exercise equipment was removed for subsequent exercise tests. Further examinations revealed that the frequency inaccuracies were related to an issue with the internal frequency sensor. As shown in Figure 5-6a, when a subject steps, two pistons move in and out, resulting in a back-and-forth movement of a belt connected to them. The movement of this belt, in turn, causes the rotation of tapered wheel, as seen in Figure 5-6b. Given the variable diameter of this wheel, when it rotates, it induces mild flexing in the adjacent cantilevered beam that acts as a frequency sensor. The rate of flexing in this sensor is passed on to the Ergospect stepper software and used as the measurement for stepping frequency.

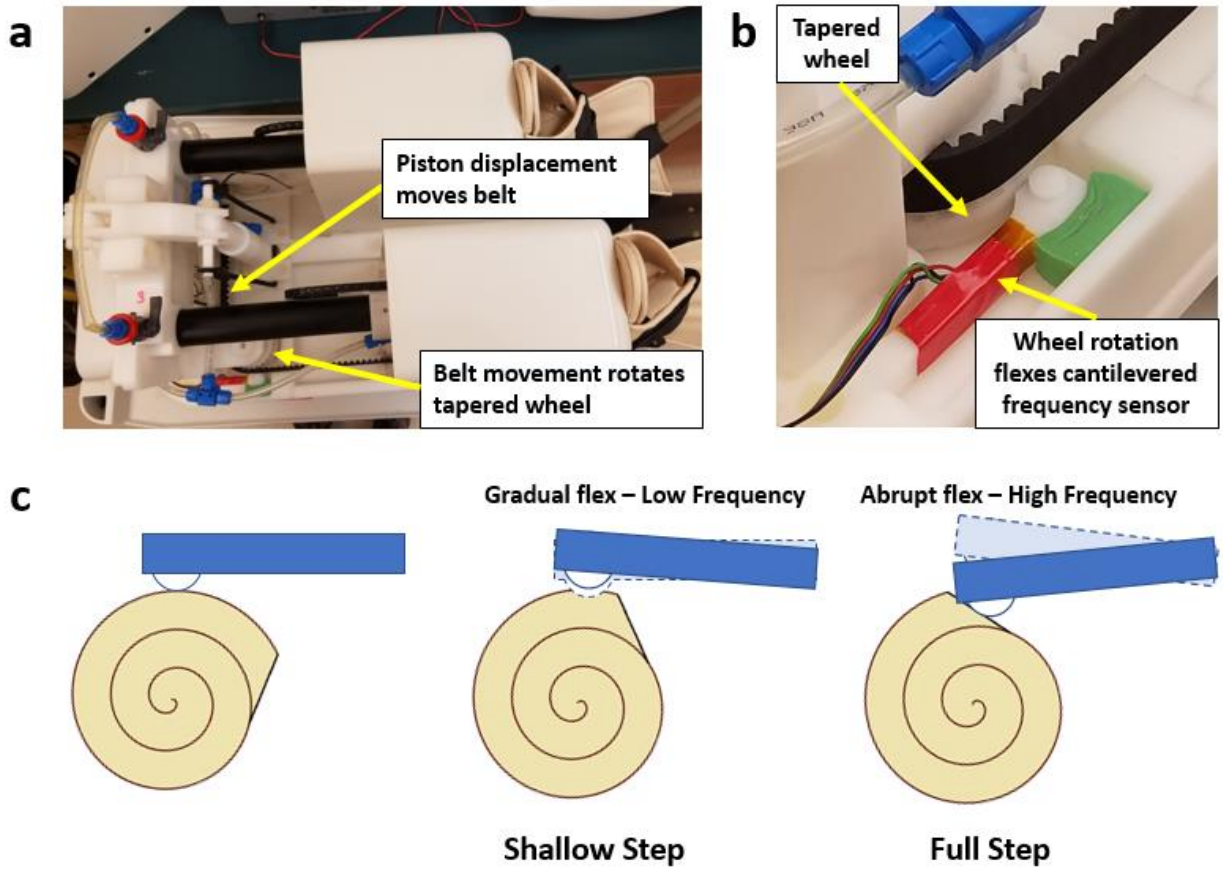

Figure 5-6: Internal view of the Ergospect stepper. (a) When the subject steps, the movement of the two pistons induces the back-and-forth movement of a belt. (b) The movement of this belt, in turn, induces the rotation of a variable-diameter wheel, which results in the flexing of an adjacent cantilevered beam serving as a frequency sensor. The rate of flex in this beam is recorded as stepping frequency. (c) Misalignment of the wheel resulted in sudden displacement of the beam as it passed over the "notch", rather than the expected gradual flexing. This resulted in the recording of erroneously high frequencies.

Because of the variable-diameter of the wheel abutting the frequency sensory, there is a “notch” where the wheel jumps from its maximum radius to its minimum radius. The Ergospect stepper was designed to operate so the cantilevered beam never crossed over this region, and instead only experienced smoothly varying flex. With the stepper used at this institution, however, the wheel had become misaligned. As a result, as shown in Figure 5-6c, when subjects took full steps, the notch would cross beneath the cantilevered frequency sensor, resulting in an abrupt flexing that was erroneously registered as a much higher stepping frequency than was actually occurring. When subjects took shallow steps, however, the wheel did not rotate enough for the notch to move beneath the sensor. This resulted in the phenomena seen in Figure 5-5, where shallow steps provided accurate frequency readings while full steps registered artificially high measurements. It was also likely responsible for the power inaccuracies seen for high exercise powers in Figure 5-4 – it had been noted during exercise studies that subjects are more prone to taking full steps at higher exercise powers when they are pushing against a greater resistance.

To address these issues, the belt was removed from exercise equipment, the wheel was rotated into proper position, and the belt was reattached. This proved to be effective at eliminating all erroneous frequency measurements. Further tests also showed that fixing the frequency sensor resulted in much more accurate power profiles, as seen in Figure 5-7. When compared to the two power curves in Figure 5-5, it is apparent that these modifications have successfully suppressed sinusoidal variations in power and inaccuracies at higher exercise powers.

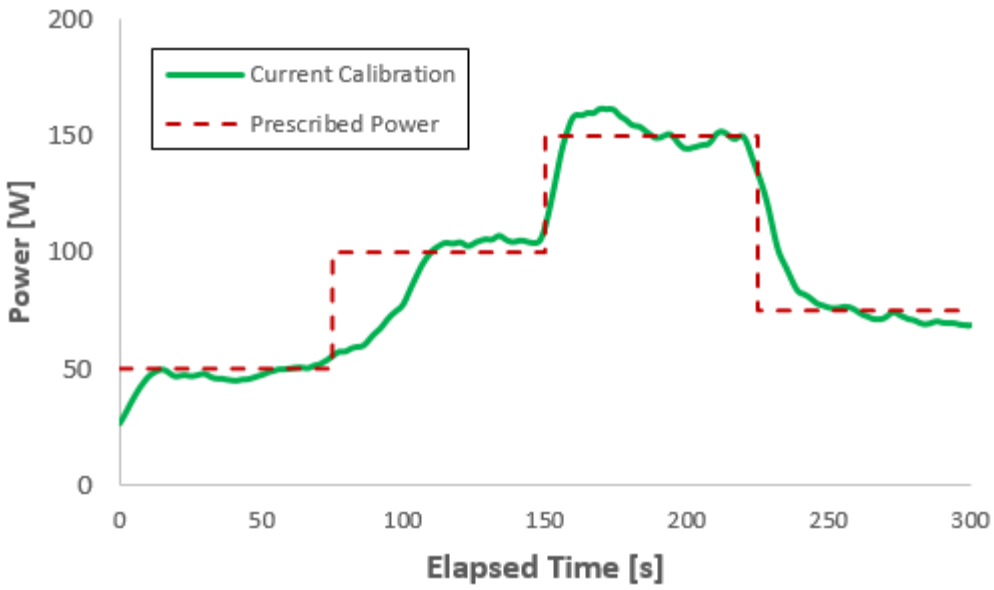

Figure 5-7: Measured exercise power curves in response to prescribed exercise challenge with current stepper calibration and modifications. There was a noticeable improvement in power accuracy at high powers when compared to the results in Figure 5-4.

5.1.4 Conclusions

With the hardware modifications and software calibrations described above, the Ergospect stepper is now capable of accurate, multi-stage exercise paradigms for exercise powers up to 400 W. This represents a significant improvement over the capabilities the UW stepper and addresses the limitations with that device identified in the initial exercise study in PH subjects. The Ergospect stepper now allows for exercise challenges more closely mirroring what is utilized in clinical settings, such as the Bruce protocol. Since proper calibration of this device, over 75 research exercise studies have been successfully completed with the Ergospect stepper with minimal complications.

Chapter 6: Feasibility of 4D Flow MRI during Exercise

The initial exercise CMR study described in Chapter 4 concluded that exercise CMR presented many advantages over traditional techniques such as stress echocardiography but had a few notable limitations: (1) the previous stepper was not capable of the high-power, multi-stage exercise challenges inherent to many clinical exercise studies and (2) traditional breath-held pulse sequences were too susceptible to motion artifacts, even when imaging was conducted post-exercise, to allow for reliable quantification in stress images. The previous chapter discussed how the implementation of the commercial Ergospect stepper overcame the challenges mentioned in the first point. In this chapter, the application of 4D Flow MRI is presented in response to the challenges in the second point.

4D Flow MRI offers many advantages over traditional 2D PC techniques when quantifying blood flow during exercise. As 4D Flow is a volumetric acquisition with measurement planes placed retrospectively, there is little concern regarding vessels of interest moving outside of the imaging volume during exercise. Furthermore, 4D Flow MRI can quantify flow in all of the great vessels and cardiac chambers simultaneously. Most importantly, however, 4D Flow MRI can be acquired alongside simultaneous respiratory and ECG. This allows for free-breathing during exercise imaging with effective motion suppression through the utilization of a retrospective double-gated reconstruction [40].

In addition to standard flow velocity and volume measurements, 4D Flow MRI is increasingly used in research applications to assess more complex hemodynamic parameters not possible with 2D PC acquisitions, including pressure gradients, pulse wave velocity (PWV), wall shear stress, and kinetic energy (KE) [5]. PWV can provide valuable information regarding vessel wall compliance. Ventricular KE is of interest because it increases with exercise in healthy subjects [122] but recent 4D Flow MRI studies have shown that KE increases without a corresponding increase in cardiac output in patients with a variety of cardiac pathologies [54]. These latter studies motivate the use of 4D Flow MRI to measure KE and cardiac output as an indicator of ventricular efficiency.

For these studies, we utilized 4D Flow MRI with a radially undersampled trajectory (PC VIPR

[43,44]), which is well suited for exercise imaging as it confers (1) increased robustness to motion and (2) good compatibility with retrospectively ECG-gated reconstructions, mitigating the impact of decreased gating signal quality during exercise. The feasibility of assessing blood flow in the aorta, main pulmonary artery, left ventricle, and right ventricle was assessed in both adult subjects and pediatric subjects.

6.1 Feasibility in Adult Subjects

Initial feasibility of PC VIPR imaging during exercise was investigated in a small cohort of healthy adult subjects. It was hypothesized that while overall image quality of 4D Flow MRI may decrease during exercise due to blurring artifacts from subject motion, PC VIPR should be able to quantify increases in blood flow and kinetic energy.

6.1.1 Methods

Eleven healthy adults (26 ± 1 years; 8 male, 3 female) at similar levels of fitness were recruited for this study. All subjects provided written informed consent. Exclusion criteria included: (1) any history of cardiovascular or cardiopulmonary disease, (2) muscular or skeletal abnormalities that could limit exercise capacity, and (3) any contraindications to MRI scanning. This study was approved by the local Institutional Review Board and was compliant with the Health Insurance Portability and Accountability Act.

Exercise Protocol: Exercise was conducted in the magnet bore with the Ergospect stepper. This equipment allowed for real-time monitoring of step frequency and exercise power, and automatically adjusts stepping resistance in real-time to maintain the target exercise power. The target exercise power for each subject was 70% of the power corresponding to each subject's maximal oxygen consumption (VO_{2max}), as previously established on a bicycle ergometer in an exercise lab. Exercise power output values for each subject are given in Table 6-1. Subjects were coached to step at a cadence of 60 steps/min for the duration of exercise. All exercise imaging was performed during continued exercise after subjects had been exercising at the target power output for at least 3 minutes and had achieved a steady-state heart rate. Composite Poincaré plots [123] were created from normalized RR interval length measurements to characterize heart rate variability and determine if steady-state heart rates were maintained during exercise.

Subject	Age	Sex	P_{max} [W]	70% P_{max} [W]
1	25	F	200	140
2	27	M	290	203
3	25	M	275	193
4	25	F	140	98
5	25	M	245	172
6[1]	26	M	290	203
7	25	F	185	130
8[2]	26	M	290	203
9	27	M	260	182
10	25	M	200	140
11	26	M	170	119

[1]Subject did not complete resting 4D Flow; [2]Subject did not complete exercise 4D Flow

Table 6-1: Subject demographic information and exercise powers corresponding to VO_{2max}

4D Flow MRI Acquisition: Subjects were imaged on a clinical 3.0 T scanner (Discovery 750, GE Healthcare, Waukesha, WI) with an 8-channel cardiac coil. Cardiac 4D Flow MRI at rest and during exercise was performed with a radially undersampled 4D flow sequence (PC VIPR) [43,44]: TR/TE = 6.2/2.0 ms; flip angle (FA) = 10°, velocity encoding (VENC) = 200 cm/s; field of view (FOV) = 32x32x32 cm; spatial resolution = 1.25 mm isotropic, scan time = 9.25 minutes fixed at rest and exercise. A higher VENC than was typical for cardiac imaging was selected to account for increased blood velocities with exercise. Images were reconstructed offline with retrospective respiratory gating from an abdominal belt to include only data during expiration with adaptive thresholding and 50% efficiency. Retrospective ECG gating with spatial frequency dependent temporal interpolation was used for cine reconstruction [40,124]. Fifteen cardiac phases were reconstructed to account for the shorter RR interval length and increased noise during elevated heart rates.

Image Quality Assessment: To assess the impact of exercise on image quality, a radiologist scored the image quality of the ascending aorta, aortic arch, descending aorta, and main pulmonary artery (MPA)

in each image series using a Likert scale with the following criteria: 0 = vessel not visible; 1 = non-diagnostic image quality; 2 = poor image quality (above average noise/artifacts); 3 = average image quality (average noise/artifacts); 4 = very good image quality (minimal noise/artifacts); 5 = excellent image quality. Rest and exercise images were anonymized and randomized so the reader was blinded to rest/exercise status. In addition, relative signal-to-noise ratio (SNR) between resting and exercise scans for each subject were compared using the SNR_{stdv} method described by Dietrich et al. [125].

4D Flow MRI Analysis (Flow): 4D Flow MRI complex difference images were segmented with MIMICS (Version 17.0, Materialize, Leuven, Belgium) to isolate the ascending aorta (AAo) and main pulmonary artery (MPA). Using previously described methods, flow quantification was performed using a combination of Ensight (Version 10.0, CEI Inc. Apex, NC), to generate two-dimensional, time-resolved magnitude and phase contrast datasets perpendicular to the vessel orientation, and a custom MATLAB tool [126], to quantify the flow through the AAo and MPA. Flow volumes per heart beat (SV), flow volumes per minute (CO), and mean flow were recorded in the AAo and MPA. The pulmonary to systemic flow ratio, Q_p/Q_s, was assessed in all subjects to measure the internal consistency of the flow measurements. PWV was measured in the aorta and MPA using the time-to-foot (TTF) method with the 4D flow workflow described by Wentland et al. [53].

To assess measurement repeatability, inter-observer and intra-observer variability was assessed in the AAo and MPA during rest and exercise. Inter-observer variability was assessed by comparing mean flow measurements from the original observer with those from a second observer blinded to the measurement plane placements and results of the original observer. To determine intra-observer variability, the original observer repeated all flow measurements in the AAo and MPA. The observers had 5 years ("original observer") and 2 years ("second observer") of experience in 4D flow post-processing.

Measurement reliability was estimated with internal flow consistency checks in the pulmonary and systemic circulation in each subject at rest and during exercise. For the pulmonary measurements, total flow in the MPA was compared to flow in the left pulmonary artery (LPA) and right pulmonary artery (RPA) together. Systemic circulation consistency was assessed by comparing total flow in AAo to that in the

descending aorta (DAo) and superior vena cava (SVC) together. As a further test of reliability, stroke volume measurements in the AAo and MPA from PC VIPR were compared in subjects against those calculated from a clinical, breath-held 2D PC acquisition at rest (TR/TE = 5.3/3.0 ms, FA = 30°, VENC = 200 cm/s, FOV = 39x39 cm, in-plane resolution = 1.5x1.5 mm, slice thickness = 6 mm, scan time ≈ 15 s). For subjects upon which data was available, such a comparison was also performed in the MPA during exercise. 2D PC measurements in the AAo were not yet available from collaborators for similar systemic comparisons during exercise.

4D Flow MRI Analysis (Kinetic Energy): The LV and RV were segmented from the time-averaged magnitude images in MIMICS [127]. A custom script applied this mask to the time-resolved velocity images to extract the velocity magnitude for each voxel in the ventricle. Ventricular KE was calculated from the sum of the KE for the voxels within the segmented volume:

$$KE = \sum_{1}^{voxels} \frac{1}{2} m v^2 = \sum_{1}^{voxels} \frac{1}{2} (\rho V) v^2 \qquad \textit{Eq. 6-1}$$

where ρ=1060 kg/m^3 is the density of blood, V=1.95 mm^3 is the voxel volume, and v is the velocity magnitude for the voxel. Ventricular energy efficiency was defined as the SV normalized to the KE, $\eta = \frac{SV}{KE}$, or the amount of blood ejected from the ventricle per unit kinetic energy in the ventricle. To minimize the influence of heart rate on comparisons, KE and η were assessed at peak systole and peak diastole, rather than across the entire cardiac cycle. Repeatability in total KE, systolic KE, and diastolic KE, was assessed with inter-observer and intra-observer variability analysis following the same protocol described for the flow measurements.

Physiologic Gating Performance: To determine the impact of exercise on robustness of standard physiologic gating used with MRI, both ECG gating tracks and respiratory bellows measurements were analyzed. To assess ECG gating performance, the percentage of data acquired outside of the median measured RR interval for each subject was calculated. The number of missed ECG triggers was estimated by using an algorithm that detected abnormally long RR intervals at approximately integer multiples of the

median heart beat length (this algorithm will be explored more in depth in the child studies later in this chapter). To better understand the performance of respiratory gating during exercise imaging, a variety of respiratory gating thresholds were investigated. For all subjects, additional reconstructions were performed with thresholds on expiration of 20%, 30%, 40%, 60%, 70%, and 100%. The impact of respiratory threshold on flow in the AAo and MPA, as well as Q_p/Q_s ratio, was quantified.

Statistical Analysis: Unless stated otherwise, all parameters are presented as the mean sample value plus/minus the sample standard deviation. Statistically significant differences in these parameters between rest and during exercise were determined with a paired student's t-test. A standard t-test was used for any groupwise comparisons (AAo vs. MPA, RV vs. LV). The image quality scores as identified by the radiologist for each image series were compared between rest and exercise using a Wilcoxon rank-sum test. Bland-Altman analysis was used to quantify the mean difference (*d*) and 95% limits of agreement (*LoA*) for the inter-observer and intra-observer variability analysis. In addition, the intraclass correlation coefficient (ICC: Case 3, Type 1) was computed for all repeated measurements. All tests used a threshold of $\alpha = 0.05$ for statistical significance.

6.1.2 Results

4D Flow MRI was successfully acquired during exercise in 10 of 11 subjects, although one of these subjects was unable to complete their resting scan due to claustrophobia. The subject who did not complete their exercise imaging ceased due to general discomfort. The average exercise power output during imaging was 158 ± 37 W. This resulted in an average increase of 44 ± 16% in heart rate (rest: 63 ± 14 bpm; exercise: 92 ± 24 bpm) during exercise ($p = 0.0001$). Figure 6-1 shows the composite Poincaré plots for all subjects at rest and during exercise. These plots showed similar long-term heart rate variability (x_2 axis) across scans at rest and under stress, as $\sigma_{x2,rest} = 0.095$ and $\sigma_{x2,stress} = 0.105$. Increased short-term variability (x_1 axis) in heart rate was observed during exercise ($\sigma_{x1,rest} = 0.054$, $\sigma_{x1,stress} = 0.076$).

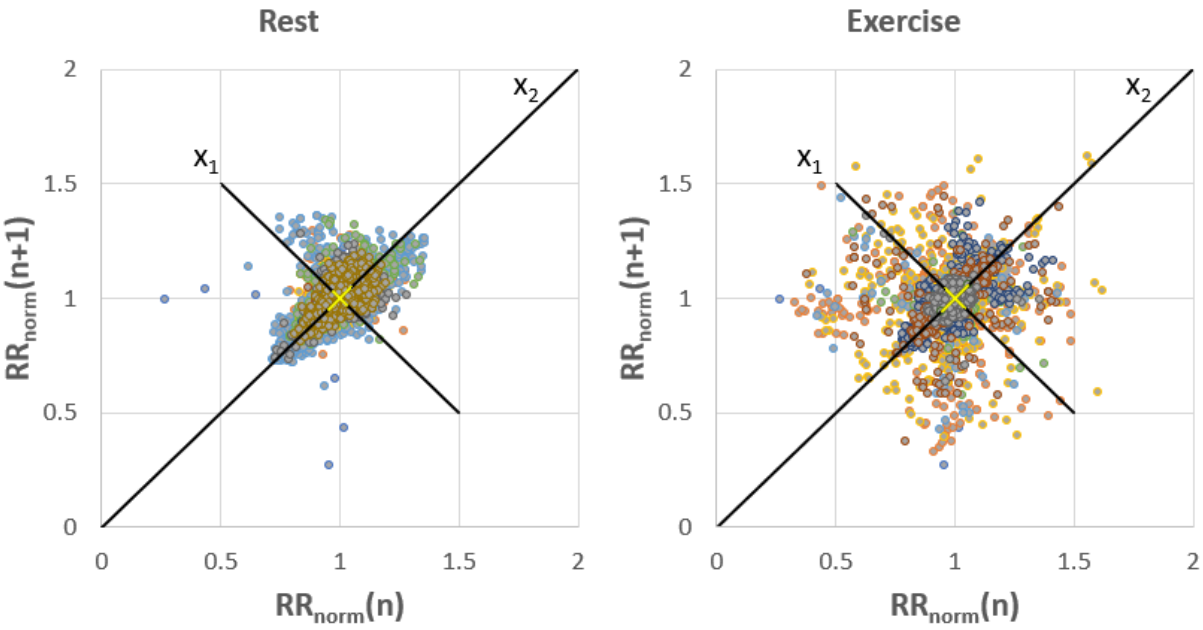

Figure 6-1: Composite Poincaré plots generated from normalized RR interval length data in each subject at rest (left) and during exercise (right). Variation along the x_1 axis represents short-term variability in heart rate, while variation along the x_2 axis represents long-term variability.

Image Quality Assessment: Qualitative image scoring by a radiologist suggested no significant difference in image quality between rest and exercise for the vessel segments investigated. Mean scores in the MPA, ascending aorta, aortic arch, and descending aorta were, respectively, 4.2 ± 0.4, 3.8 ± 0.4, 3.6 ± 0.9, and 4.1 ± 0.8 at rest and 4.5 ± 0.5 (p=0.3), 3.9 ± 0.3 (p=1), 3.3 ± 0.9 (p=0.6), and 4.5 ± 0.5 (p=0.3) during exercise. Notably, however, for both rest and exercise images, image scoring was statistically significantly lower in the ascending aorta and aortic arch when compared to the MPA ($p<0.001$ for both). Exercise 4D Flow images showed an average decrease in SNR of approximately 15% (maximum decrease: 35%) relative to resting 4D Flow in the same subjects, largely due to increased motion blurring during exercise. Small vessels and regions with more complex flow dynamics, such as aortic arch and ventricles, were impacted the most by SNR decreases, but the AAo, MPA, and ventricles could be segmented in all subjects. Representative examples of the impact of exercise on image quality in magnitude images, complex difference images, and segmented PC angiograms are shown in Figure 6-2.

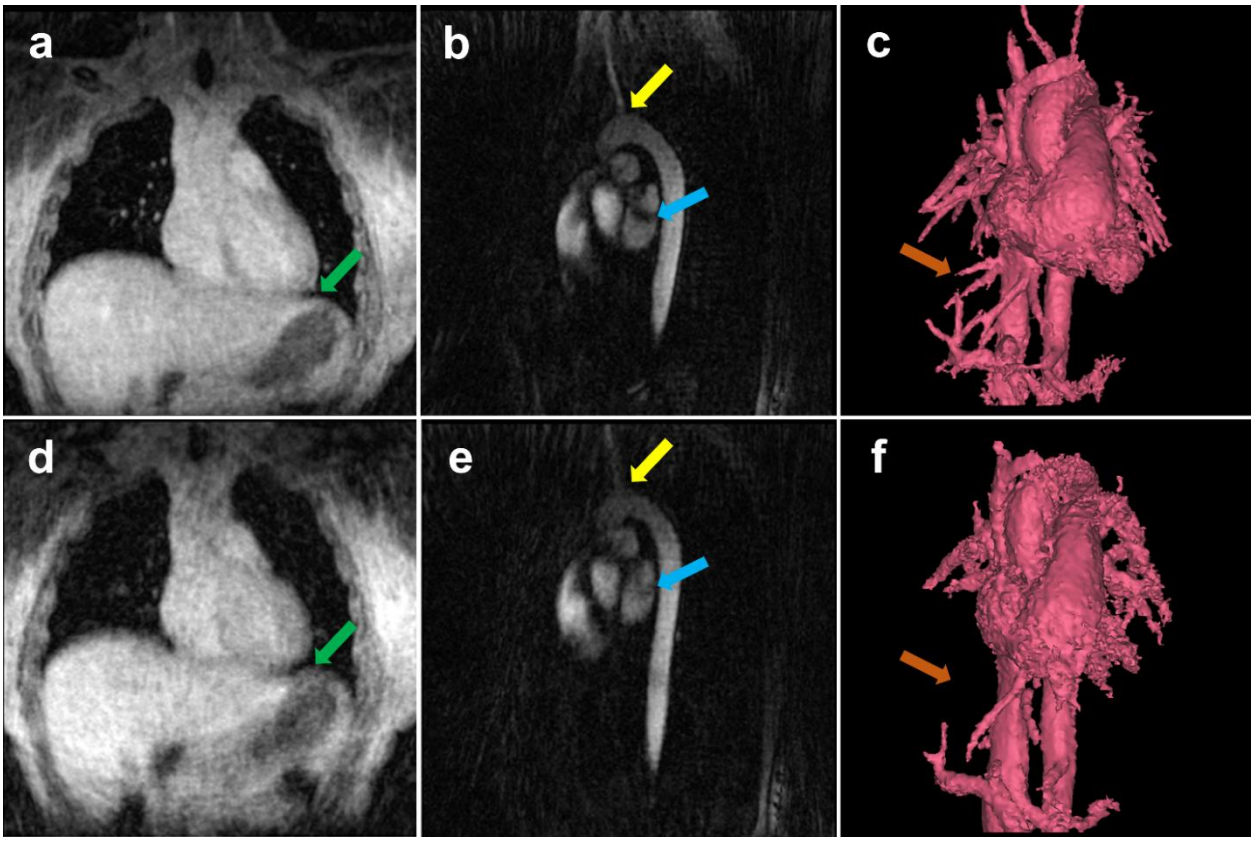

Figure 6-2: Representative resting data shown as a (a) coronal magnitude slice, (b) sagittal PC angiogram slice, and (c) segmented, volume rendered PC angiogram reconstructed from a 4D Flow MRI acquisition. Increased blurring and decreased conspicuity of regions with slow or complex flow is observed in the (d) coronal magnitude image, (e) sagittal PC angiogram, and (c) volume-rendered angiogram acquired during exercise. Colored arrow pairs indicate regions with the most noticeable changes in image quality between rest and exercise.

Flow Analysis: Flow analysis in the AAo and MPA is summarized in Figure 6-3. SV showed no significant changes with exercise. Mean systemic SV was 75 ± 12 mL at rest and 81 ± 27 mL during exercise, while pulmonary SV was 79 ± 13 mL at rest and 93 ± 29 mL during exercise. In contrast, CO showed highly significant increases with exercise, rising from 4.7 ± 0.5 L/min to 7.0 ± 1.4 L/min in the AAo ($p=0.001$) and from 4.9 ± 0.8 L/min to 8.0 ± 1.4 L/min in the MPA ($p<0.001$). Mean flow also increased from 84 ± 11 mL/s to 127 ± 22 mL/s in the AAo ($p<0.001$) and from 87 ± 14 mL/s to 146 ± 24 mL/s in the MPA ($p<0.001$). At rest, the average Q_p/Q_s ratio was 1.05 ± 0.17, while the average value was 1.16 ± 0.10 during exercise. The distribution of Q_p/Q_s ratios during exercise was a statistically significant difference from the

normal value (≈1) for healthy subjects. In the aorta, PWV showed significant increases with exercise in all subjects, from 4.0 ± 0.6 m/s to 6.6 ± 2.7 m/s (p=0.03). PWV measurements in the MPA, however, were not possible due to temporal resolution constraints and the shorter vessel length when compared to the AAo.

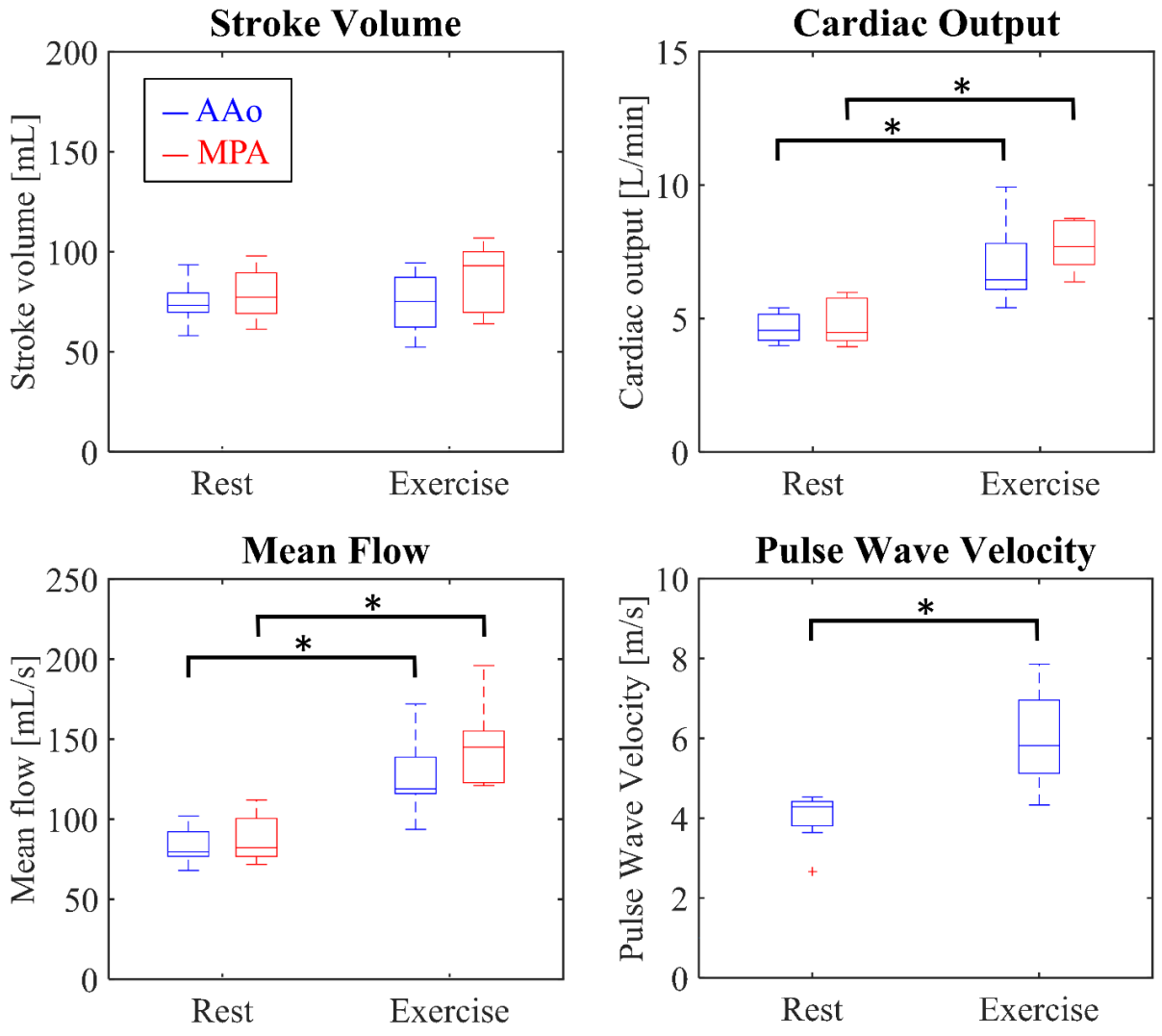

Figure 6-3: Distributions of stroke volume, cardiac output, mean flow, and pulse wave velocity as measured at rest and during exercise in the ascending aorta (AAo) and main pulmonary artery (MPA). A bracket between two boxplots indicates statistically significant differences between the two distributions ($p < 0.05$). Pulse wave velocity measurements are only shown for the aorta, as measurements were not possible in the MPA.

Inter-observer and intra-observer measurements showed excellent agreement at both rest and stress for flow

measurements in the AAo and MPA. Inter-observer comparisons at rest showed a relative difference of 6% in the AAo and 5% in the MPA and good correlation between measurements ($ICC_{AAo,rest}$ = 0.89; $ICC_{MPA,rest}$ = 0.95). Similar variability was observed for measurements during exercise, where relative differences of 4% in the AAo and 6% in the MPA were obtained. Once again, there was good correlation between the measurements of the two observers ($ICC_{AAo,stress}$ = 0.94; $ICC_{MPA,stress}$ = 0.91). Intra-observer comparisons showed slight improvements, with average relative differences of 4% in both the AAo and MPA at rest, 2% in the AAo during exercise, and 4% in the MPA during exercise. Excellent correlation was observed for these measurements ($ICC_{AAo,rest}$ = 0.94; $ICC_{MPA,rest}$ = 0.95; $ICC_{AAo,stress}$ = 0.98; $ICC_{MPA,stress}$ = 0.97). Bland-Altman plots, including mean difference and 95% LoA are presented in Figure 6-4 for these comparisons.

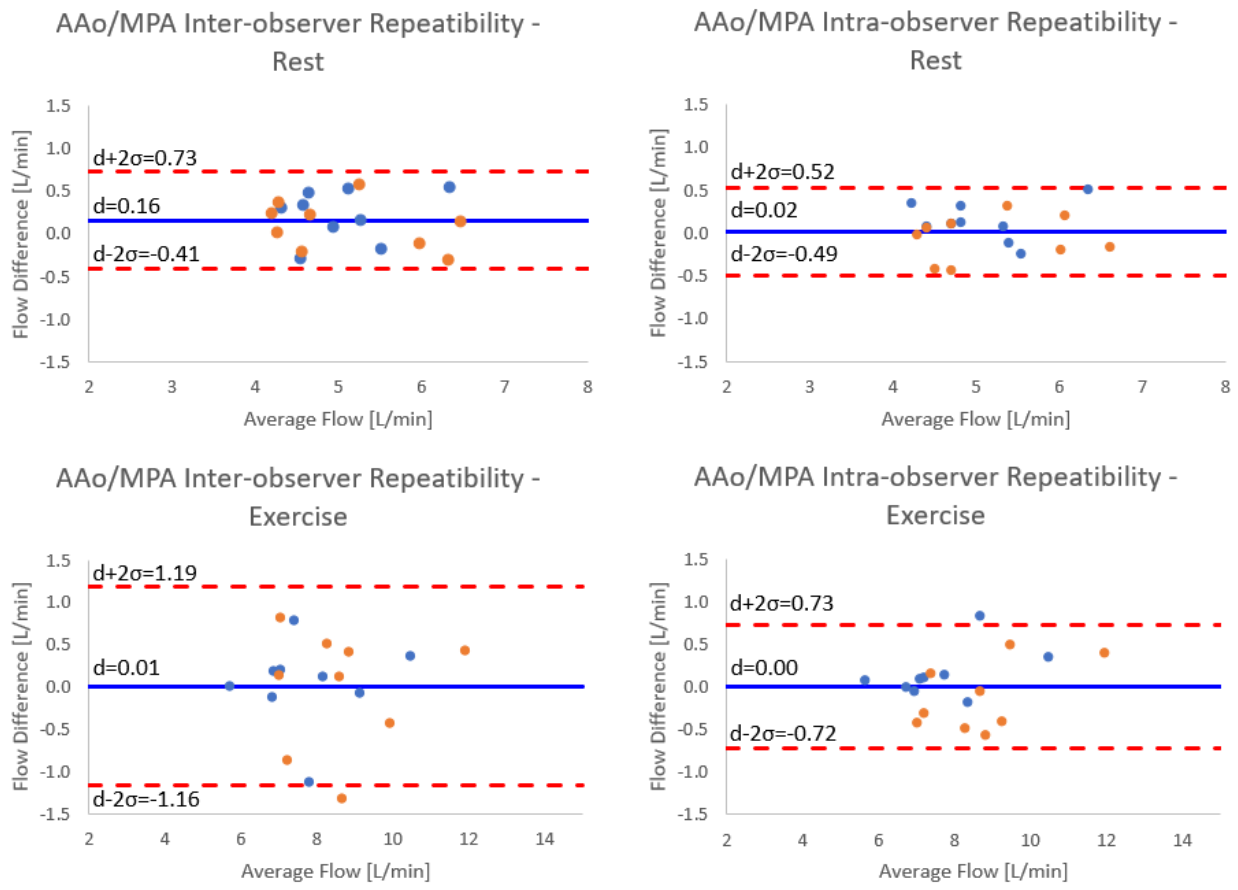

Figure 6-4: Bland-Altman plots for inter-observer and intra-observer variability in mean flow in the AAo (blue dots) and MPA (orange dots) at rest and during exercise. The solid blue line indicates the mean difference (d), while the dashed red lines indicate the upper and lower bounds of the 95% limits of agreement.

Table 6-2 shows the results from the checks of internal consistency in the systemic circulation. At rest, an average difference of flow of 12% was observed between the AAo and DAo+SVC, while an average difference of 8% was measured when comparing flow in the MPA against the LPA+RPA. During exercise, these differences were 15% and 17% respectively.

Rest

Subject	Systemic Consistency [mL]					Pulmonary Consistency [mL]				
	AAo	DAo	SVC	Diff.	Percent	MPA	LPA	RPA	Diff.	Percent
1	55.5	44.6	32.2	-21.3	38.4	63.1	25.1	35.9	2.1	3.3
2	95.5	73.9	36.9	-15.3	16.0	84.4	46.1	47.7	-9.4	11.1
3	74	44.6	36.4	-7	9.5	93.4	47.5	63.7	-17.8	19.1
4	75.8	44.9	32	-1.1	1.5	71.3	28.7	44.2	-1.6	2.2
5	79.5	44.2	37.2	-1.9	2.4	94.2	42.9	50	1.3	1.4
6	75.9	44	20.5	11.4	15.0	75.2	47.2	36.7	-8.7	11.6
7	93.4	57.8	35.2	0.4	0.4	77.8	40.4	44.1	-6.7	8.6
8	74.3	53.5	35.6	-14.8	19.9	71.1	39.9	41.2	-10	14.1
9	71.3	39.6	28.7	3	4.2	63	31.2	34.6	-2.8	4.4
				Average:	12 ± 12%				**Average:**	8 ± 6%

Exercise

Subject	Systemic Consistency [mL]					Pulmonary Consistency [mL]				
	AAo	DAo	SVC	Diff.	Percent	MPA	LPA	RPA	Diff.	Percent
1	63.1	59.1	15.8	-11.8	18.7	67.3	31.2	48.7	-12.6	18.7
2	72.7	53.5	24.3	-5.1	7.0	75.2	26.8	31.6	16.8	22.3
3	76.2	71.9	39.9	-35.6	46.7	99.9	41	65	-6.1	6.1
4	74.4	58.1	24.8	-8.5	11.4	73	25.1	42.9	5	6.8
5	97.1	56.1	28.9	12.1	12.5	111	37.3	41.7	32	28.8
6	52.8	37.2	20.2	-4.6	8.7	66.9	20.2	29.8	16.9	25.3
7	75.5	61.3	23.5	-9.3	12.3	Could not resolve LPA or RPA.				
8	86.2	55	36.5	-5.3	6.1	95.5	32.2	45.2	18.1	19.0
9	63.7	49.3	20.4	-6	9.4	66.5	25.3	35.5	5.7	8.6
				Average:	15 ± 13%				**Average:**	17 ± 9%

Table 6-2: Internal consistency measurements for flow in the pulmonary and systemic circulation at rest and during exercise. All measurements are total flow in the vessel across a single cardiac cycle. $Diff_{systemic}$ = AAo – (DAo+SVC). $Diff_{pulmonary}$ = MPA – (LPA+RPA).

Figure 6-5 shows comparisons of flow measurements acquired with PC VIPR and the standard, clinical 2D PC sequence. PC VIPR consistently underestimated the 2D PC measurements by an average of 24% in the AAo and 25% in the MPA.

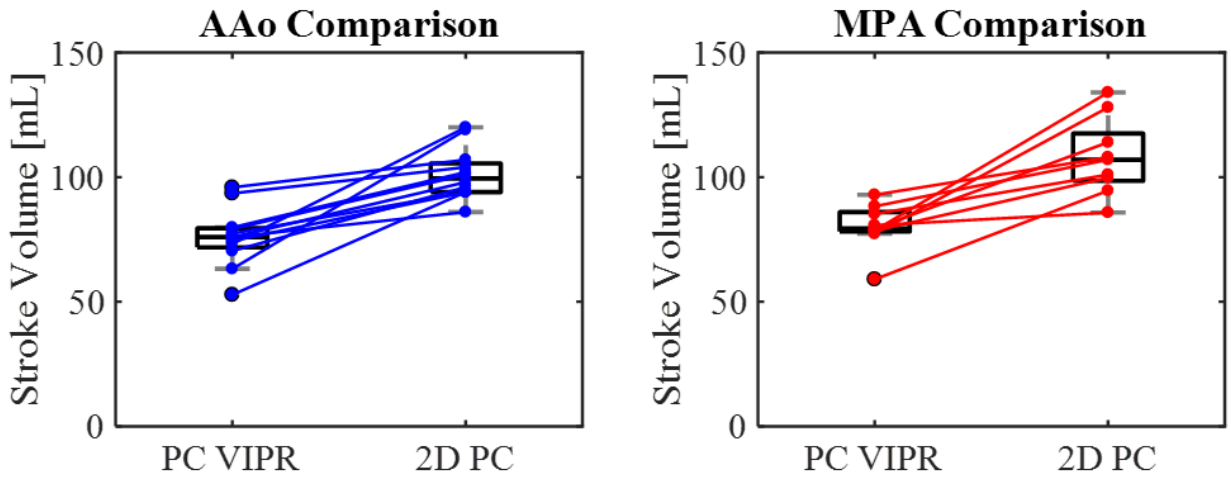

Figure 6-5: Comparison of flow measurements acquired with PC VIPR and a standard 2D PC sequence in the ascending aorta and main pulmonary artery during rest. Consistently lower flow was measured with PC VIPR acquisitions in both vessels.

Consistently lower PC VIPR measurements were also observed in the MPA during exercise, as seen in Figure 6-6. On average, PC VIPR measurements were 32% lower than 2D PC during exercise.

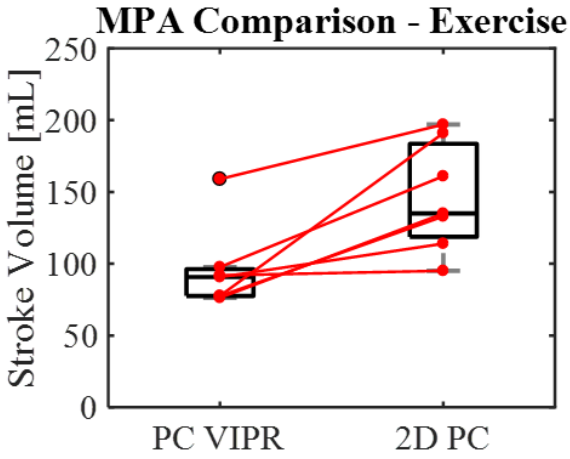

Figure 6-6: Comparison of flow measurements acquired with PC VIPR and a standard 2D PC sequence in the main pulmonary artery during exercise. Again, PC VIPR measurements showed lower flow than those quantified from 2D PC.

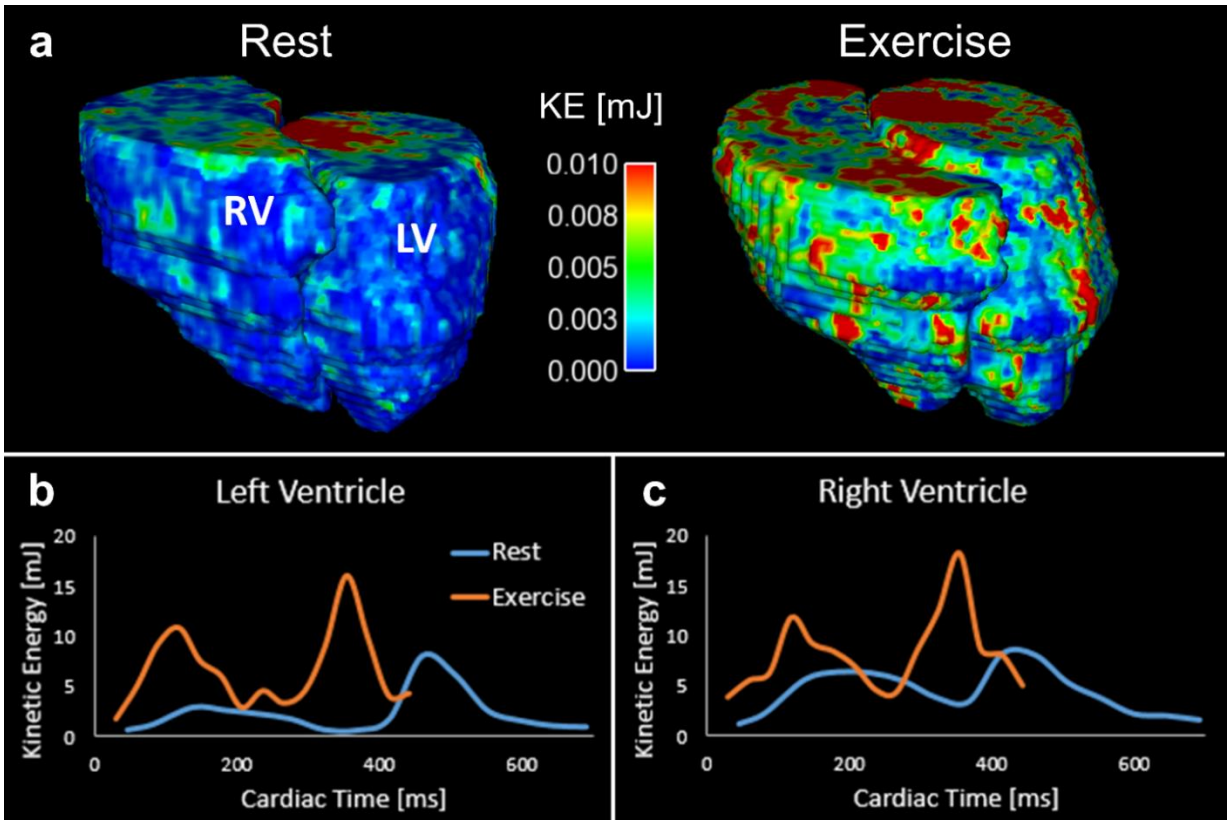

Figure 6-7: 4D Flow analysis of kinetic energy (KE) during rest and exercise: (a) KE maps show increases in LV and RV KE with exercise; time resolved plots of KE in the (b) LV and (c) RV show large increases in KE during diastolic filling and systolic ejection. Time-resolved KE curves have been smoothed by fitting a 3rd order Bezier spline to the measurements in each cardiac phase.

Kinetic Energy Analysis: The capabilities of 4D flow MRI analysis of ventricular KE are shown in Figure 6-7. KE maps during rest and exercise show (Figure 6-7a) clear increases in the KE in both ventricles with exercise. Time-resolved plots of KE in the LV (Figure 6-7b) and RV (Figure 6-7c) show dual peaks corresponding to diastolic filling and systolic ejection. These values, along with KE efficiency, are quantified at end-systole and end-diastole for each subject in Figure 6-8. KE_{RV} showed significant increases with exercise during both systole (8.3 ± 2.3 mJ at rest and 12.6 ± 4.5 mJ during exercise, p=0.02) and diastole (5.7 ± 1.2 mJ at rest and 9.7 ± 5.5 mJ during exercise, p=0.04). KE_{LV}, on the other hand, demonstrated non-significant increases with exercise for both systole (4.3 ± 1.8 mJ at rest and 9.0 ± 6.8 mJ during exercise, p=0.11) and diastole (6.9 ± 2.1 mJ at rest and 8.5 ± 4.0 mJ during exercise, p=0.38). During systole, KE_{RV} was consistently greater than KE_{LV}, but minimal differences were observed during diastole.

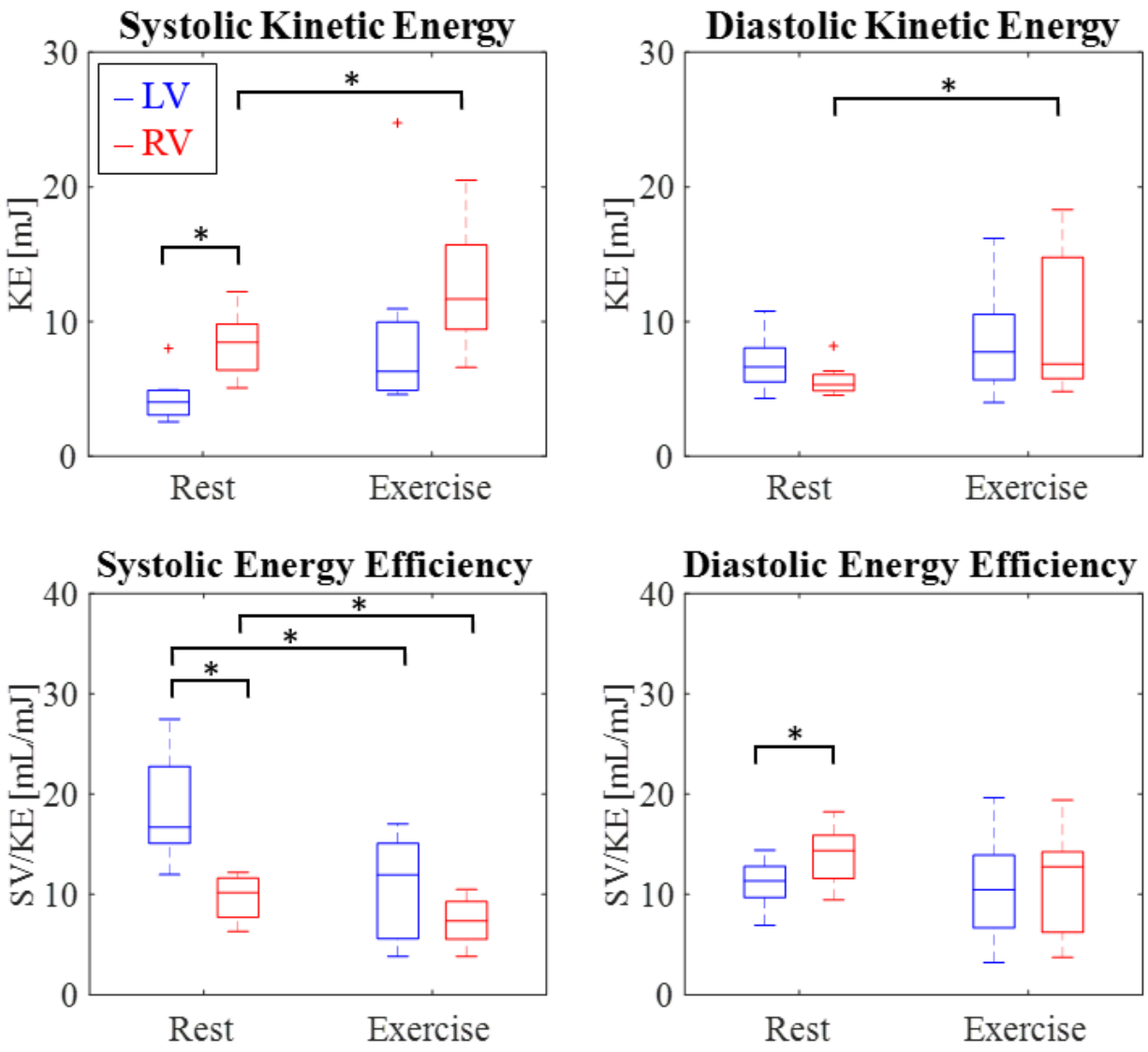

Figure 6-8: Distributions of kinetic energy and ventricular energy efficiency in healthy adults at peak systole and peak diastole at rest and during exercise in the left and right ventricles. A bracket between two boxplots indicates a statistically significant difference between the two distributions.

With regards to ventricular efficiency, exercise induced significant decreases during systole in both η_{RV} (9.6 ± 2.3 mL/mJ at rest and 7.3 ± 2.4 mL/mJ during exercise, p=0.04) and η_{LV} (18.6 ± 5.3 mL/mJ at rest and 10.8 ± 5.2 mL/mJ during exercise, p=0.04). Such differences were not as apparent in diastole (η_{RV} = 13.9 ± 2.9 mL/mJ at rest and 11.2 ± 5.5 mL/mJ during exercise, p=0.12; η_{LV} = 11.1 ± 2.4 mL/mJ at rest and 10.6 ± 5.5 mL/mJ during exercise, p=0.82). At rest, η_{RV} was significantly lower than η_{LV} during systole

($p<0.001$) and significantly higher during diastole ($p=0.05$).

Inter-observer and intra-observer repeatability analysis for KE measurements showed dramatically reduced agreement when compared to flow measurements in the MPA and AAo. For the sake of brevity, results in this section will be presented in the format *parameter* = [*total/systole/diastole*]. Inter-observer comparisons at rest showed average relative differences of [28/35/21]% in the LV and [30/38/23]% in the RV. Correlation of measurements was varied, but were generally poor outside of diastole: $ICC_{LV,rest}$ = [0.28/0.26/0.79] and $ICC_{RV,rest}$ = [0.22/0.41/0.43]. Surprisingly, inter-observer comparisons during exercise showed similar relative differences of [24/27/21]% in the LV and [30/33/23]% in the RV, but noticeably improved correlation: $ICC_{LV,stress}$ = [0.75/0.71/0.93] and $ICC_{RV,stress}$ = [0.70/0.74/0.87]. Intra-observer comparisons at rest yielded relative differences of [35/32/19]% in the LV and [34/48/22]% in the RV. During exercise, the relative differences decreased to [19/20/18]% in the LV and [32/42/20]% in the RV. As before, improved correlation was seen during exercise: $ICC_{LV,rest}$ = [0.42/0.17/0.75], $ICC_{RV,rest}$ = [0.50/0.73/0.68], $ICC_{LV,stress}$ = [0.91/0.96/0.87], and $ICC_{RV,stress}$ = [0.75/0.73/0.89]. Bland-Altman plots for total KE, including mean difference and 95% LoA, are presented in Figure 6-9 for these comparisons.

Physiologic Gating Performance: At rest, on average, 98% of projections were acquired within the median RR interval, with the lowest percentage for a single subject being 94%. During exercise, on average, 94% of projections were acquired within each subject's median RR interval, with the lowest single-subject percentage reaching 88%. Across all subjects, these values corresponded to an average of 2% of RR triggers missed at rest and 7% missed during exercise. Figure 6-10 shows the impact of respiratory gating threshold during image reconstruction on Q_p/Q_s ratio, AAo flow, and MPA flow. MPA flow was relatively independent of the chosen threshold, while Ao flow was drastically underestimated for low threshold percentages. This resulted in most accurate Q_p/Q_s ratios measured for thresholds around 60-70%.

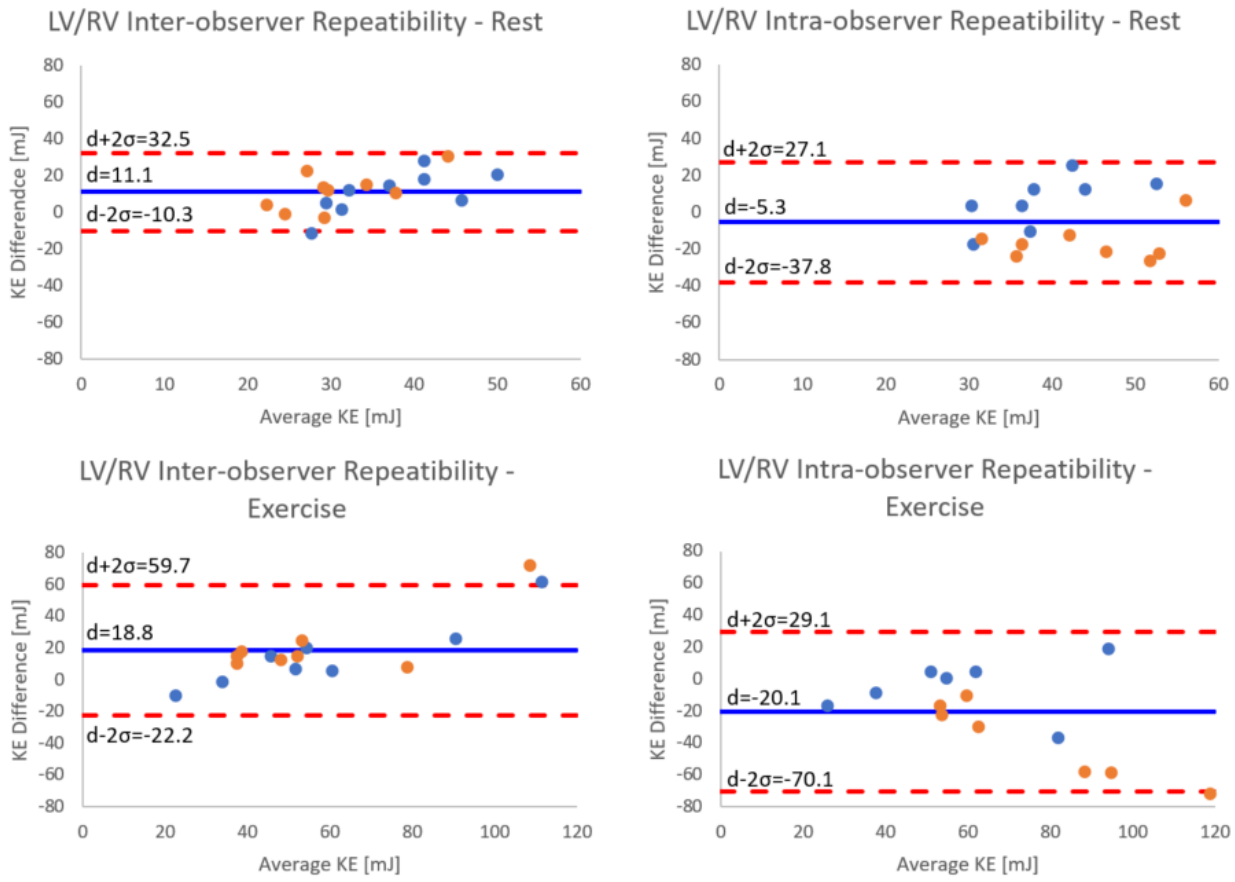

Figure 6-9: Bland-Altman plots for inter-observer and intra-observer variability of total KE in the LV (blue dots) and RV (orange dots) at rest and during exercise. The solid blue line indicates the mean difference (d), while the dashed red lines indicate the upper and lower bounds of the 95% limits of agreement.

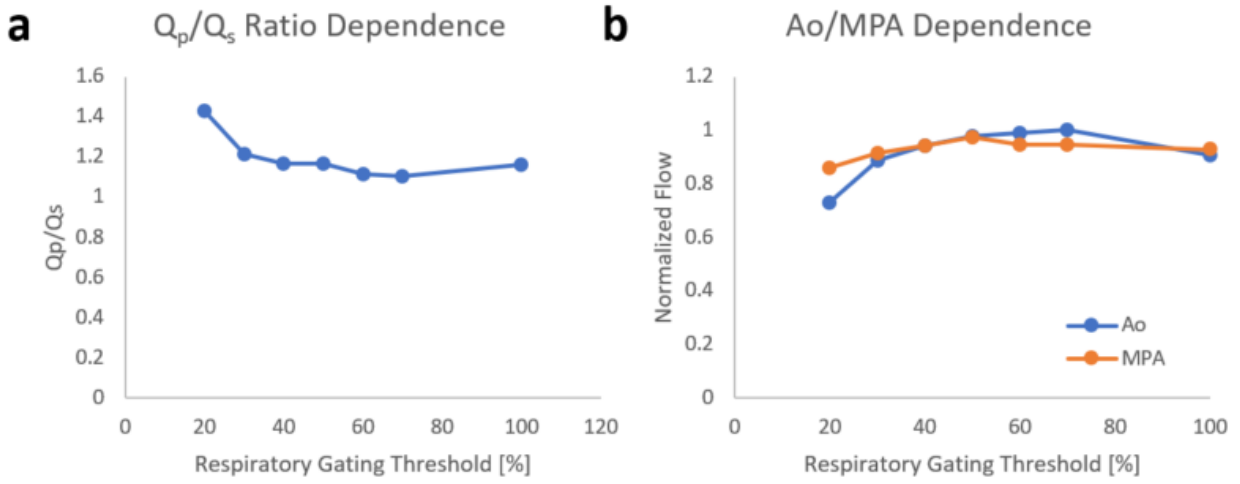

Figure 6-10: Dependence of (a) Q_p/Q_s and (b) Ao and MPA flow on respiratory gating threshold during image reconstruction.

6.1.3 Discussion

These results demonstrated the feasibility of high power exercise challenges in the MRI bore and simultaneous 4D Flow MRI imaging, as ten of eleven subjects successfully completed the exercise challenge at a sustained exercise power at 70% of their individual VO_{2max}. The subject that did not complete their exercise challenge stopped due to general discomfort rather than exhaustion. Performing future exercise CMR on a wide-bore scanner may help mitigate discomfort and claustrophobia induced by exercising in the narrow magnet bore. Analysis of heart rate variability during the extended exercise sessions with Poincare plots showed similar long-term variability between the groups at rest and during exercise, suggesting 3 minutes of exercise prior to imaging was sufficient to obtain a steady-state heart rate during imaging. Further analysis of cardiac gating showed a minor decrease in ECG gating quality during exercise with a slight increase in missed RR triggers. Although this issue was not significant in this study, techniques to improve ECG gating robustness may be required for exercise imaging in patient populations with less reliable gating signals.

The lack of significant differences in SV between rest and exercise were not unexpected, as it has been previously demonstrated that, unlike upright exercise, supine exercise often does not have a measurable impact on SV [128]. In contrast, cardiac output and mean blood flow in the AAo and MPA and increased significantly with exercise. Intra-observer and inter-observer comparisons for flow in the MPA and AAo showed excellent repeatability at rest and during exercise, suggesting the observed minor decrease in SNR during exercise was not an impediment to consistent segmentation of these vessels. PWV measurements at rest showed excellent agreement with those reported in previous 4D flow studies [53,129], and PC VIPR during exercise was able to quantify increases in this parameter with exercise in all subjects. While PWV is often used as a surrogate for vessel compliance, this increase with exercise likely reflects the increased cardiac output with exercise, rather than a change in vessel compliance.

The distribution of Q_p/Q_s ratios measured at rest reflected excellent measurement consistency, as these values were not statistically significant from the expected value of approximately 1 for healthy subjects. Notably, however, this was not the case during exercise where flow in the MPA was, on average,

15% higher than that in the AAo for all subjects. The investigation into the effects of variable respiratory thresholds during image reconstruction suggested this parameter may play a role in this discrepancy, as aortic flow was highly dependent on this threshold during exercise. On average, optimal Q_p/Q_s values were obtained during exercise at a threshold of 70% on expiration. This represents approximately a 40% increase in reconstructed data over the typical threshold of 50%, which roughly corresponds to an SNR gain of 18%. At rest, it was observed that SNR in the AAo was already lower than that in the MPA. It is hypothesized that the SNR gain associated with the more lenient respiratory threshold may help offset the measured further 15% SNR loss from exercise. Improvements in Q_p/Q_s ratio did not continue for higher respiratory thresholds, as further SNR boosts were likely offset by increased blurring from respiratory motion. It is also speculated that differences in AAo and MPA scan plane placement relative to the direction of respiratory motion could result in different sensitivities to changes in this motion during exercise.

Measurements of internal flow consistency in the systemic and pulmonary circulation showed good agreement both at rest and during exercise. These results suggested precision of 4D flow measurements during exercise similar to that observed during a typical exam at rest. Comparisons of SV as measured with PC VIPR and a standard breath-held 2D PC sequence showed that PC VIPR consistently underestimated flow for all subjects. This was consistent with results reported in prior comparisons of 4D flow MRI and 2D PC techniques [126,130–133]. While the mechanisms for the disparity between these techniques are not fully understood, some have been postulated. As a result of the increased number of velocity-encoding steps, 4D flow acquisitions feature poorer temporal resolution than 2D PC approaches. It has been demonstrated this will result in poorer characterization of peak flow, and therefore lower stroke volumes [132]. Furthermore, 4D flow exams are much longer than 2D acquisitions, resulted in flow waveforms averaged over a greater number of heart beats. If heart rate naturally varies during 4D flow imaging, the reconstructed waveform will represent an average cardiac response which may be lower than would be seen with a faster 2D sequence at the beginning of the imaging period. On the other hand, Frydrychowicz et al. reported that using a phantom calibration instead of software calibration to account for phase offsets from eddy currents improved agreement between 4D flow and 2D PC measurements, suggesting some additional

role of eddy currents [130]. Despite the lower flow measurements with 4D flow techniques, Hanneman et al. showed that the Q_p/Q_s ratio is preserved, suggesting this error is systemic and accurate relative comparisons between 4D flow data are still feasible [131]. Thus, while PC VIPR flow measurements may have reduced absolute accuracy, comparisons between rest and exercise acquisitions should still hold significant value. The relative flow underestimation with PC VIPR slightly increased during exercise, but it was unclear if this was a simply result of the smaller sample size, unsuitability of the breath held 2D PC sequence for exercise acquisitions, or reduced ability of PC VIPR to adequately characterize peak flow with increased heart rates. These factors, combined with the good agreement seen in the internal consistency measurements above, suggested PC VIPR was a viable approach for quantitative whole-heart flow imaging during strenuous exercise.

Of all the parameters measured, total ventricular KE proved to be most sensitive to changes with exercise, showing the greatest increase in mean value during stress. These results were consistent with those reported previously from studies utilizing cardiac catheterization [122]. When compared to one another at rest, KE_{RV} was higher than KE_{LV} during systole but lower during diastole, in agreement with results presented from previous 4D flow studies [134,135], and these relationships were preserved in measurements during exercise. In the context of this feasibility study, SV normalized by KE energy did not provide any additional sensitivity to exercise as a surrogate for ventricular efficiency. However, this was possibly because all recruited subjects for this study demonstrated similar healthy ventricular dynamics, whereas this parameter may prove more responsive in studies involving patients with compromised or irregular cardiac function.

While KE measurements were the most sensitive to increases in exercise, they also demonstrated noticeably increased relative differences and decreased correlation in the inter-observer and intra-observer comparisons as compared to flow measurements. This is likely a “double-edged sword” of KE calculations based around squared velocity measurements, as the effects of noise are enhanced as well. For reference, two KE measurements in a single voxel with a 30% difference, the magnitude typically observed in this study, represent a change in velocity of 16%. Correlation was typically poor for end-systolic measurements

but good for end-diastolic measurements. This was likely a consequence of using a time-averaged mask resulting in analysis volumes closer to end-diastolic volumes than end-systolic. These results suggest the application of a time-resolved mask, likely registered from corresponding bSSFP scans to achieve reasonable SNR, could greatly improve the repeatability of KE measurements in the ventricles. Fascinatingly, relative differences were lowest and correlation was highest for measurements performed during exercise, despite reduced SNR. It is hypothesized that the blurring of fine ventricular features may have reduced observer subjectivity when contouring the ventricles, resulting in better agreement (though not necessarily a more accurate segmentation).

This use of 4D Flow MRI for exercise CMR offered many advantages over traditional clinical stress echocardiography including (1) time-resolved flow distributions over a 3D imaging volume not reliant on fitting data to pre-established flow models, (2) more repeatable quantification of right-heart function, and (3) the ability to reconstruct PC angiograms from flow data, all possible from a single scan. Streamline and pathline visualizations of flow can also be generated from 4D flow data, allowing for visualization and characterization of complex flow patterns. Such tools could be valuable for exploring how ventricular flow, which has been shown to be highly vortical [136,137], will evolve in response to exercise, and illustrate the reduced ventricular efficiency observed during exercise in all subjects.

When compared to prior studies performing exercise CMR, many advantages of using a radially undersampled 4D Flow sequence were apparent. To counter the challenges of increased motion and breath hold difficulty during exercise, early exercise CMR relied on imaging following exercise [101,138], resulting in a rapidly dropping heart rate during imaging due to natural recovery from exercise. The ability to image during free-breathing exercise with 4D Flow MRI allowed for quantification of exercise stress with a more physiologic, steady-state heart rate. The natural motion robustness of the radial k-space trajectory (PC VIPR) mitigated the increased motion artifacts introduced from bulk subject motion during exercise and resulted in only a minor SNR loss from motion blurring in exercise images. Radiologist image scoring only noted above average noise and artifacts in a single exercise acquisition, with most cases being scored as very good or excellent image quality. Alternatively, real-time PC MRI [139] could overcome the

challenges of breathing and subject motion during exercise, but currently such approaches are limited to 2D acquisitions with coarse spatial resolution and are particularly difficult to perform at high heart rates.

This study had a few limitations. While the small sample size was sufficient for proof of concept, it does not prove definitive robustness of this technique. In addition, each subject's VO_{2max} was determined from exercise challenges on an upright stationary bicycle. Subsequently, the target exercise power during scanning was set to 70% of this VO_{2max}. It has been previously shown that posture has an impact on cardiac dynamics during exercise [128] and, therefore, the baseline for 100% VO_{2max} might be different in a supine position in the bore. On top of this, possible systemic differences in exercise power measurements between the exercise stepper and upright bicycle were not characterized. While this was not a major factor for our feasibility study, it might be an important consideration for exercise CMR studies that require precise exercise responses. The poor repeatability and high variability of KE measurements limited the statistical significance of comparisons. This could limit the diagnostic value of this parameter in clinical applications and warrants improved characterization of sources of variability to improve performance in future work. Possible sources of error in intra-ventricular measurements may include sub-optimal sequence optimization (VENC and spatial resolution specifically), differences in segmentation techniques between observers, and the use of a time-averaged mask for segmentation. Finally, while the choice of 15 cardiac frames was adequate for maintaining sufficient SNR for vessel segmentation during exercise, it limited sensitivity to time-resolved cardiac dynamics.

6.1.4 Conclusions

In this study, we demonstrated the feasibility of using 4D flow MRI for whole-heart exercise CMR in healthy controls. Almost all subjects successfully completed a strenuous exercise challenge at a power corresponding to 70% VO_{2max}. MRI measurements showed significant increases in cardiac output and flow in the great vessels and KE in the ventricles. Minor decreases in SNR were associated with imaging during exercise, but overall flow measurements during stress still appeared to be reliable, in part due to the natural motion robustness of PC VIPR. We believe with further testing and development biventricular 4D flow

exercise CMR can fulfill a valuable clinical role in evaluating and monitoring patients with right-side or whole-heart defects, a group previously not well-addressed by the clinical standard of stress echocardiography. Future directions to address the limitations of this work are proposed in Chapter 8.

6.2 Application in Pediatric Subjects

The previous feasibility study clearly demonstrated that PC VIPR with retrospective ECG and respiratory gating could be used effectively to quantify complex flow in the ventricles and great vessels during strenuous exercise challenges in adult subjects. Extending the ability to conduct exercise CMR examinations to pediatric populations would be of special interest to clinicians in monitoring the manifestation and progression of a variety of conditions, especially those associated with right-heart or whole-heart abnormalities which are not well-served by echocardiography. For example, exercise testing has been shown to have good prognostic value in pediatric subjects suffering from cystic fibrosis [140]. Exercise stress tests can also be used effectively in pediatric patients with Tetralogy of Fallot and other congenital heart defects to assess exercise capacity, monitor disease progression, and establish the efficacy of surgical repairs [141,142].

Exercise CMR in pediatric subjects, however, presents a few notable challenges not commonly observed in an adult population. In general, pediatric subjects are less compliant than adult populations. This can result in greater deviations from prescribed exercise protocols than in adults. Also, as a result of their smaller body sizes relative to the magnet bore, children have a much greater range of motion in the scanner, allowing for increased bulk motion during exercise. A primary concern for this increased motion is more prevalent motion artifacts during image reconstruction. While such motion can still be minimized with the dual-gating PC VIPR approach described before [40], additional factors inherent to exercise makes acquiring robust ECG gating inherently more difficult. Increased respiratory motion in the presence of steep gradient fields may induce voltage in the ECG leads, reducing the accuracy of ECG traces [143]. In addition to this, on average, children feature increased heart rates relative to adults [144], which has been linked to decreased ECG signal fidelity as a result of increased magnetohydrodynamic effects [145]. These factors,

when coupled with the decreased quality of ECG lead contact due to subject perspiration, result in a higher rate of inaccuracies when attempting to use ECG gating during exercise CMR. A pulse oximeter can be used for cardiac gating instead, but these devices are also susceptible to false readings in the presence of motion.

In the context of these exercise studies, the decreased gating fidelity normally manifested as missed cardiac triggers. Increased noise in the ECG trace reduced the accuracy of the algorithm that detected the R wave corresponding to the beginning of each new heartbeat. This resulted in the cardiac gating recording erroneously long RR intervals, or heart beat lengths, when previous R waves were not detected. This proved to be a significant issue with the PC VIPR reconstruction, as the length of the reconstructed cardiac waveform was determined from the median heart beat length across the entire acquisition. When a significant amount of artificially long RR intervals were recorded, this resulted in an irregularly long reconstructed heartbeat. Such a reconstruction could result in the inclusion of a second systolic peak and a non-physiologic flow waveform. These effects are demonstrated in Figure 6-11. As seen in Figure 6-11a, typical RR interval lengths show a natural variability across a scan, in part due natural heart rate variability and limited temporal resolution when sampling. Figure 6-11b shows a typical reconstructed aortic flow waveform. In Figure 6-11c, the potential effects of exercise on gating is visualized. There is a notable amount of missed heart beats, resulting in an inaccurate flow waveform (Figure 6-11d). This waveform has an improperly long reconstructed cardiac cycle length, resulting in the inclusion of the systolic waveform from the "next" cardiac cycle.

Here we test the feasibility of using PC VIPR to assess flow in the great vessels and ventricles during strenuous exercise challenges in a pediatric population. Results are compared to those measured in the healthy adult population. To counter the challenges related to the decreased ECG trace fidelity, a custom algorithm was implemented to detect missed triggers and assign the corresponding projections to the correct phase in the cardiac cycle.

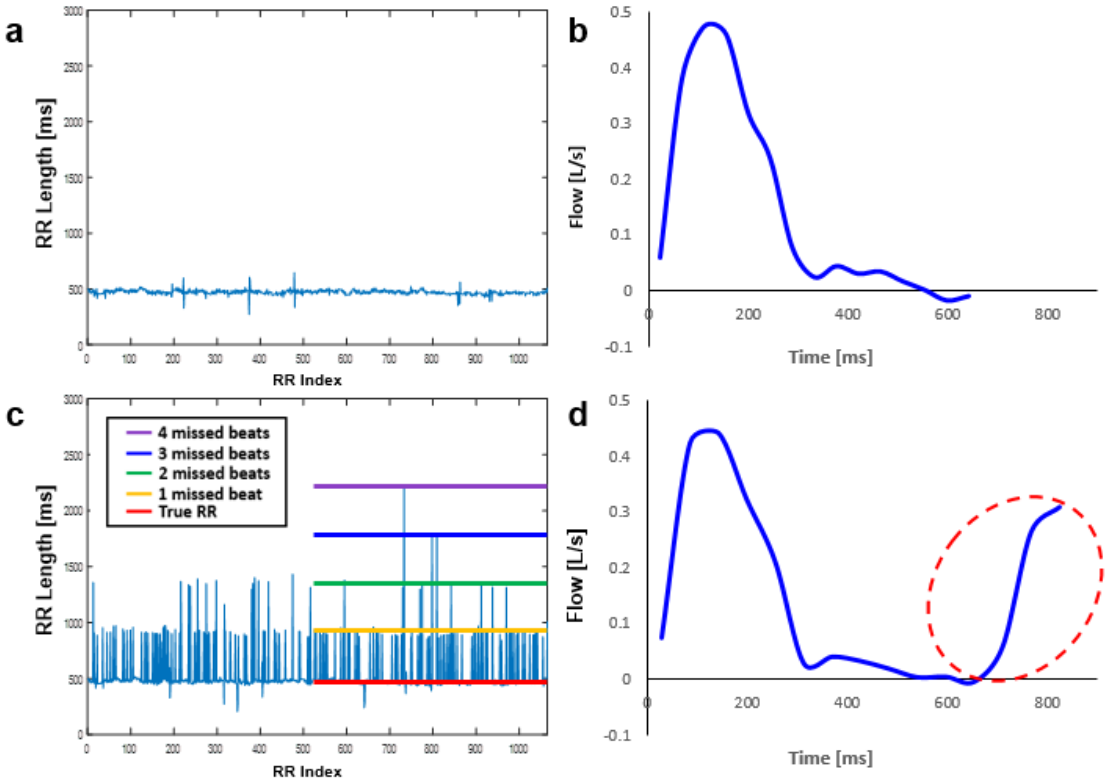

Figure 6-11: (a) Typical variability noted in RR interval length as recorded by ECG gating and (b) a typical reconstructed aortic flow waveform. (c) During exercise, many artificially long RR intervals are observed as a result of previously missed R-wave triggers, resulting in (d) a reconstructed flow waveform with an artificially long cardiac length. As a result, systolic data from the "next" cardiac cycle in included, yielding an inaccurate representation of flow across the cardiac cycle.

6.2.1 Methods

Eighteen healthy, prepubescent children (13 ± 1 years; 8 male, 10 female) at similar stages of fitness were recruited for this study. All subjects provided written informed consent. As before, exclusion criteria included: (1) any history of cardiovascular or cardiopulmonary disease, (2) muscular or skeletal abnormalities that could limit exercise capacity, and (3) any contraindications to MRI scanning. This study was approved by the local Institutional Review Board and was compliant with the Health Insurance Portability and Accountability Act.

Exercise Protocol: Exercise was conducted in a supine position in the magnet bore with the Ergospect stepper. The target exercise power for each subject was 70% of the power corresponding to each

subject's VO_{2max}, as previously established on a bicycle ergometer in an exercise lab. Subjects were verbally coached to step at a cadence of 60 steps/min for the duration of exercise. All exercise imaging was performed after subjects had been exercising at the target power output for at least 3 minutes and had achieved a steady-state heart rate.

4D Flow MRI Acquisition: Subjects were imaged on a clinical 3.0 T scanner (Discovery 750, GE Healthcare, Waukesha, WI) with an 8-channel cardiac coil. Cardiac 4D Flow MRI at rest and during exercise was performed with an identical radially-undersampled PC VIPR acquisition to that performed in the adult subjects [43,44]: TR/TE = 6.2/2.0 ms; flip angle (FA) = 10°, velocity encoding (VENC) = 200 cm/s; field of view (FOV) = 32x32x32 cm; spatial resolution = 1.25 mm isotropic, scan time = 9.25 minutes). Images were reconstructed offline with retrospective respiratory gating from an abdominal belt to include only data during expiration with adaptive thresholding and 50% efficiency. Retrospective ECG gating was used for cine reconstruction [40,124]. Fifteen cardiac phases were reconstructed to allow for improved SNR in each time frame during exercise.

ECG Gating Correction: During image reconstruction, the median RR interval length was calculated and the percentage of data acquired outside of this interval was presented. If more than 5% of the acquired projections were outside of this window, a gating correction algorithm was applied to the ECG gating track in MATLAB. This threshold was subjectively identified as the amount of inaccuracies that could be tolerated before noticeable changes were observed in the reconstructed flow waveforms. The algorithm compared each recorded RR interval length to the median length of the fifty closest RR intervals, which was assumed to well-approximate the true heartbeat length. If the RR interval length was found to be close to an integer multiple (2 or greater) of the median value, and thus the result of previously missed R wave triggers, the interval in question was subdivided into multiple equal-length intervals on the order of the expected heartbeat length. These corrections were saved as a new ECG gating track. For subjects requiring corrected gating, the reconstruction described above was repeated with the new gating track.

Image Quality Assessment: To assess the impact of exercise on image quality, relative SNR between resting and exercise scans for each subject were compared using the SNR_{stdv} method described by

Dietrich et al. [125]. This SNR performance was compared to that quantified in the adult subjects.

4D Flow MRI Analysis (Flow): 4D Flow MRI complex difference images were segmented with MIMICS (Version 17.0, Materialize, Leuven, Belgium) to isolate the ascending aorta (AAo) and main pulmonary artery (MPA). Flow quantification was performed using a combination of Ensight (Version 10.0, CEI Inc. Apex, NC), to generate two-dimensional, time-resolved magnitude and phase contrast datasets perpendicular to the vessel orientation, and a custom MATLAB tool [126], to quantify the flow through the AAo and MPA. Stroke volume (SV), cardiac output (CO), and mean flow were recorded in the AAo and MPA. The pulmonary to systemic flow ratio, Q_p/Q_s, was assessed in all subjects to measure the internal consistency of the flow measurements. To assess the impact and efficacy of the gating correction algorithm on flow measurements, peak systolic flow and stroke volume were compared intra-subject for reconstructions with original and corrected gating.

4D Flow MRI Analysis (Kinetic Energy): The LV and RV were segmented from the time-averaged magnitude images in MIMICS [127]. A custom script applied this mask to the time-resolved velocity images to extract the velocity magnitude for each voxel in the ventricle. Ventricular KE was calculated using Eq. 6-1 from above. Ventricular energy efficiency was defined as the SV normalized to the KE, $\eta = \frac{SV}{KE}$. To minimize the influence of heart rate on comparisons, KE and η were assessed at peak systole and peak diastole, rather than across the entire cardiac cycle.

Statistical Analysis: Unless stated otherwise, all parameters are presented as the mean sample value plus/minus the sample standard deviation. Statistically significant differences in these parameters between rest and during exercise were determined with a paired student's t-test ($\alpha = 0.05$). A standard t-test was used for any groupwise comparisons (AAo vs. MPA, RV vs. LV).

6.2.2 Results

All subjects successfully completed exercise imaging. The average exercise power output during imaging was 107 ± 24 W. This resulted in an average increase of 45 ± 14% in heart rate (approx. 35 bpm) during exercise ($p < 0.0001$).

ECG Gating Correction: Seven of eighteen children had corrupted ECG gating where at least 5% of all data was acquired outside of the expected RR interval. Across these subjects, an average of 27 ± 13% of ECG triggers during the MRI acquisition were missed. ECG correction was attempted in these seven subjects, and PC VIPR reconstruction was performed again with the corrected gating track. Following correction, only 3 ± 2% of data was acquired outside of the new expected heartbeat length, in excellent agreement with 2 ± 1% observed in subjects with robust gating. However, two of the subjects featured gating tracks that could not be properly fixed with the MATLAB algorithm. This occurred because these gating tracks featured other sources of inaccuracy besides missed triggers, including premature triggers and unexpected changes in median signal magnitude, as shown in Figure 6-12. These additional sources of error introduced more complex variation in recorded heartbeat length that made correcting for missed beats challenging.

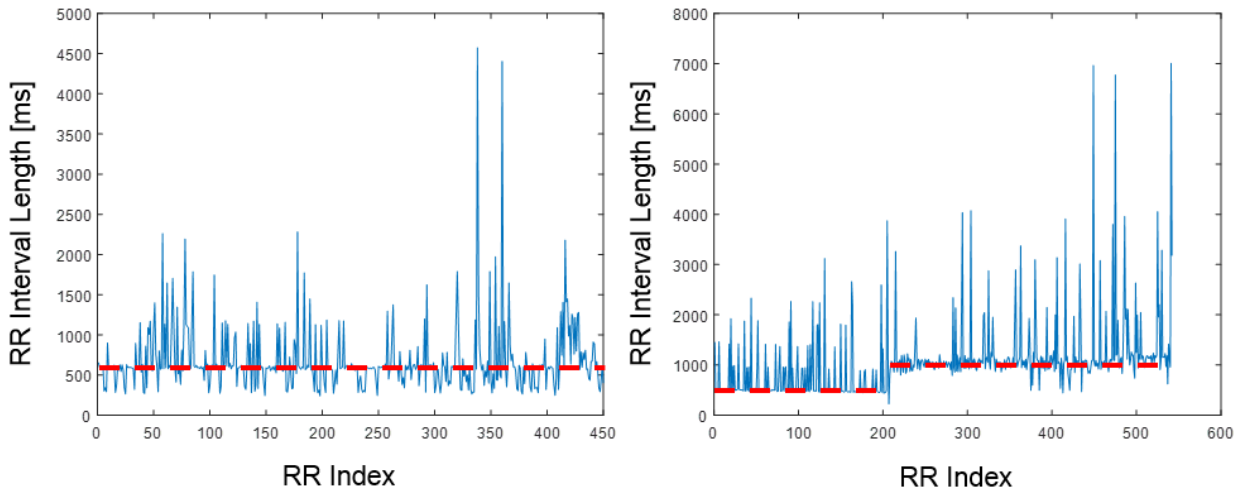

Figure 6-12: Recorded RR interval lengths over time for the two subjects the ECG correction algorithm could not properly correct for. (Left) This gating recorded a multitude of premature triggers (triggers below dashed red line). When premature triggers were immediately followed by missed triggers, RR-intervals at non-integer multiples of the expected heart beat length (dashed red line) were recorded. The correction algorithm, which looked for intervals at integer multiples, could not correct for these. (Right) This subject featured an abrupt change in the measured baseline, obfuscating the correct RR interval missed triggers should be corrected to.

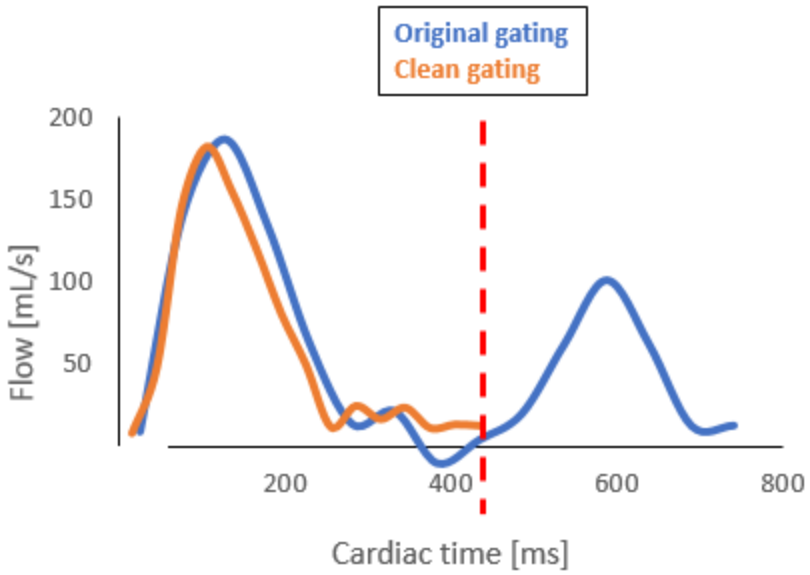

Figure 6-13: Effect of corrected ECG gating on aortic flow waveforms. Shortening of the reconstructed cardiac cycle from decreased median RR interval length resulted in the elimination of spurious flow corresponding to the systolic upstroke of a second cardiac cycle (as separated by the dashed red line). The original systolic waveform (and peak flow) was well preserved, however.

Figure 6-13 shows the impact of reconstruction with a corrected gating file on a representative flow waveform, as measured in the ascending aorta. The original systolic waveform and peak flow was preserved when compared against the original reconstruction, but total flow decreased due to the elimination of the non-physiologic flow upstroke at the end of the cardiac cycle. Quantification of changes in peak flow and total flow (stroke volume) with the corrected gating reconstruction are is presented in Table 6-3. Across all measurements, peak flow changed an average of 8.3±7.8%, while total flow showed a great average change of 28.2±19.4%.

Image Quality Assessment: Relative SNR approximations quantified an average decrease in SNR of approximately 20% with exercise in child subjects. Ten of eighteen subjects showed changes of less than 15%, and the maximum loss observed across all subjects was approximately 50%. This represented a greater effect of exercise imaging on SNR than noted previously in the adult subjects.

Subject	Vessel	Original gating		Clean Gating		Percent change	
		Peak [mL/s]	SV [mL]	Peak [mL/s]	SV [mL]	Peak [mL/s]	SV [mL]
1	Ao						
	MPA						
2	Ao						
	MPA						
3	Ao	0.189	0.120	0.181	0.056	4.2	53.7
	MPA	0.271	0.171	0.255	0.071	5.9	58.8
4	Ao	0.314	0.092	0.239	0.056	23.9	39.1
	MPA	0.356	0.114	0.354	0.076	0.6	33.4
5	Ao	0.221	0.014	0.176	0.018	20.4	26.6
	MPA	0.333	0.061	0.306	0.057	8.1	6.9
6	Ao	0.394	0.063	0.397	0.065	0.8	2.4
	MPA	0.412	0.064	0.430	0.067	4.4	5.3
7	Ao	0.237	0.056	0.254	0.041	7.2	25.9
	MPA	0.234	0.072	0.252	0.051	7.7	29.6
					Average:	8.3 ± 7.8	28.2 ± 19.4

Table 6-3: Peak systolic flow (Peak) and stroke volume (SV) in the aorta (Ao) and main pulmonary artery (MPA) as measured for reconstructions with original and corrected ECG gating. The gating tracks for subjects 1 and 2 could not be salvaged by the correction algorithm.

4D Flow MRI Analysis (Flow): Flow analysis across all subjects (using corrected gating if available) is presented in Figure 6-14. SV showed minimal changes with exercise. Left heart SV was 57.0 mL at rest and slightly decreased to 50.5 mL during exercise ($p=0.02$). Right-heart SV was 57.9 mL at rest and increased to 61.0 mL during exercise ($p=0.28$). Pulmonary SV was significantly higher than systemic SV during exercise ($p=0.01$). These measurements corresponded to average Q_p/Q_s ratios of 1.02 ± 0.14 at rest and 1.23 ± 0.19 during exercise. This mirrored the measurements in the healthy adults, where resting measurements showed Q_p/Q_s measurements exceptionally close to the expected value for healthy subjects ($Q_p/Q_s=1$), but measured pulmonary flow was noticeably higher than systemic flow during exercise.

CO was more sensitive to exercise than SV. Systemic CO increased from 4.5 ± 0.8 L/min at rest to 5.7 ± 1.0 L/min during exercise ($p<0.001$). Likewise pulmonary CO increased from 4.6 ± 0.8 L/min to 6.9 ± 1.0 L/min ($p<0.001$). Once again, during exercise, pulmonary CO was significantly greater than systemic CO ($p=0.004$). Mean flow featured similar relationships to CO. Left-heart mean flow was 84.7 ± 16.8 mL/s

at rest and 102.6 ± 22.0 mL/s during exercise (p=0.002). Right-heart mean flow increased from 86.0 ± 14.8 mL/s at rest to 124.8 ± 24.4 mL/s during exercise (p<0.001). Right-heart flow was significantly higher than left-heart flow during exercise (p=0.02).

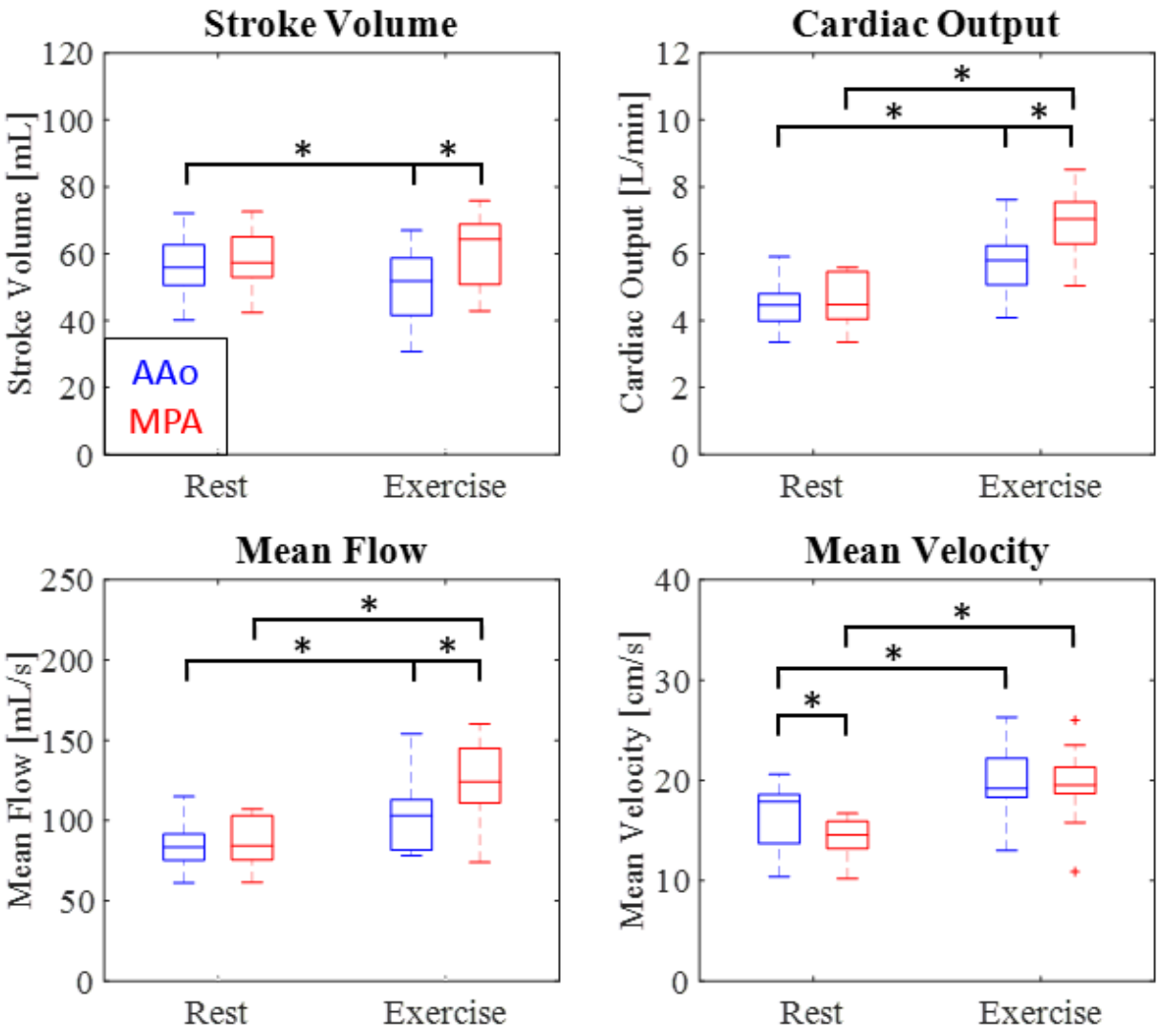

Figure 6-14: Distributions of stroke volume, cardiac output, mean flow, and mean velocity as measured at rest and during exercise in the ascending aorta (AAo) and main pulmonary artery (MPA). A bracket between two boxplots denotes statistically significant differences (p<0.05).

Mean blood flow velocity in the AAo and MPA was also sensitive to exercise. Mean velocity in the AAo was 16.4 ± 3.0 cm/s at rest and 19.6 ± 3.9 cm/s ($p<0.001$). In the MPA, mean velocity increased from 14.3 ± 2.1 cm/s at rest to 19.5 ± 3.6 cm/s during exercise ($p<0.001$). While there was no significant difference between systemic and pulmonary velocity during exercise, pulmonary velocity was significantly lower during rest ($p=0.04$), likely due to the larger vessel cross-sectional area.

4D Flow MRI Analysis (Kinetic Energy): Figure 6-15 presents the distributions for kinetic energy and kinetic energy efficiency (η) at peak systole and diastole during rest and exercise. During peak systole, KE_{LV} increased from 3.2 ± 1.5 mJ at rest to 5.7 ± 2.3 mJ during exercise ($p=0.005$). KE_{RV} increased from 5.6 ± 3.3 mJ at rest to 7.7 ± 3.3 mJ during exercise ($p=0.003$). During peak diastole, KE_{LV} was 6.2 ± 2.2 mJ and increased to 7.5 ± 2.8 mJ during exercise ($p=0.07$). Likewise, KE_{RV} increased from 4.3 ± 1.0 mJ to 7.0 ± 2.4 mJ ($p<0.001$). Systolic KE_{RV} was higher than KE_{LV} at rest ($p=0.03$) and exercise ($p=0.09$), but lower than KE_{LV} at rest ($p=0.03$) and exercise ($p=0.62$) during diastole.

At peak systole, η_{LV} decreased from 20.4 ± 7.5 mL/mJ at rest to 10.5 ± 5.7 mL/mJ during exercise stress ($p=0.007$), and η_{RV} decreased from 12.0 ± 3.6 mL/mJ to 9.3 ± 5.2 mL/mJ during exercise ($p=0.08$). During peak diastole, η_{LV} was 9.7 ± 2.3 mL/mJ at rest and 8.2 ± 5.5 mL/mJ during exercise ($p=0.39$). η_{LV} decreased from 13.6 ± 2.3 mL/mJ at rest to 9.6 ± 3.7 mL/mJ during exercise ($p<0.001$). Right-heart efficiency was lower than left-heart efficiency at rest ($p=0.001$) and stress ($p=0.58$) during systole, but higher than left-heart efficiency at both rest ($p=0.004$) and stress ($p=0.45$) during diastole.

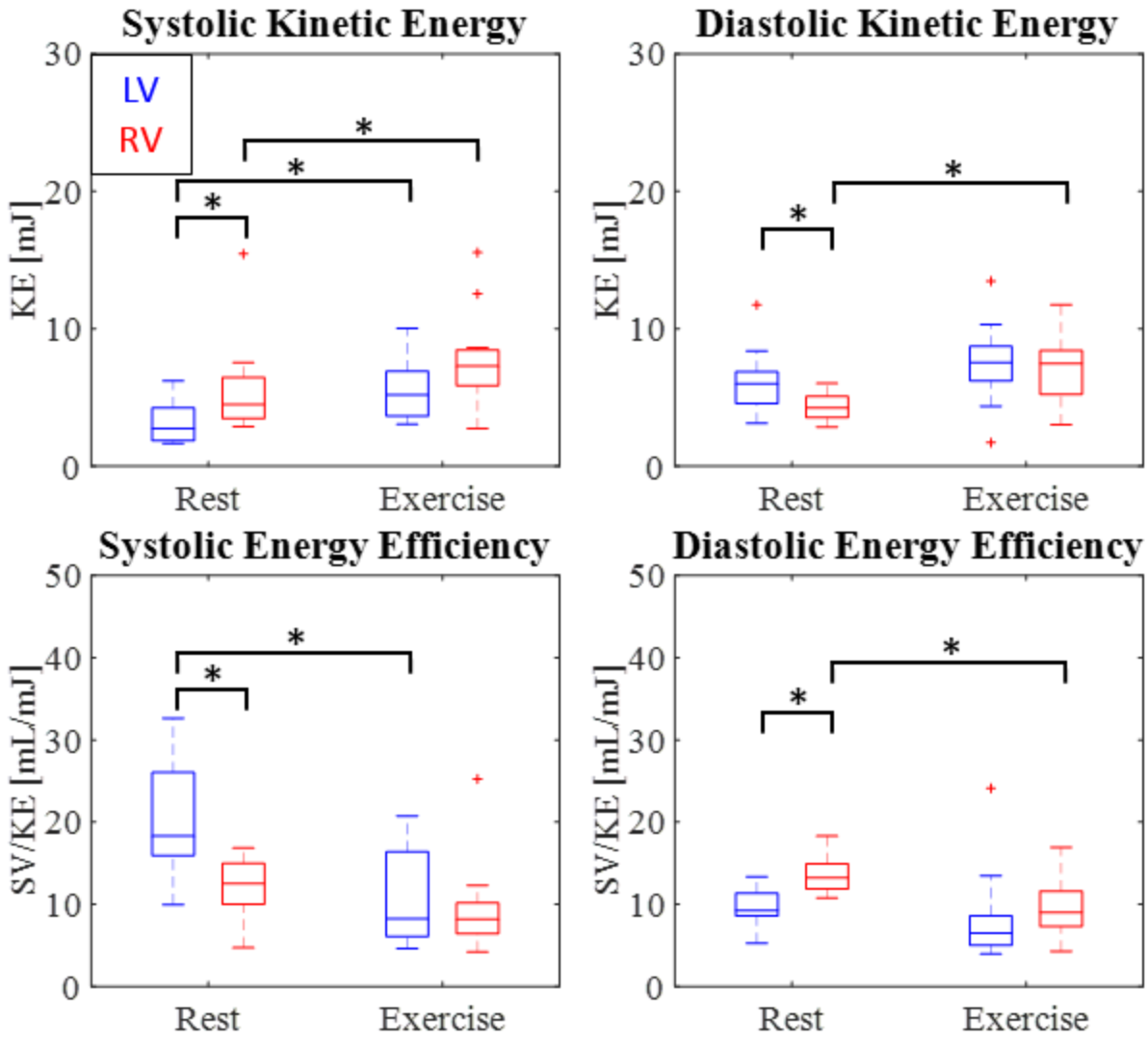

Figure 6-15: Distributions of kinetic energy and kinetic energy efficiency during systole and diastole as measured at rest and during exercise in the left ventricle (LV) and right ventricle (RV). A bracket between two boxplots denotes statistically significant differences ($p<0.05$).

6.2.3 Discussion

As with the adult subjects, extended exercise challenges at 70% of each subject's VO_{2max} appeared feasible, as all subject successfully completed exercise imaging. A noticeable issue with child exercise studies not encountered with the adult subjects, however, was the increased prominence of corrupted ECG gating. Almost half of all subjects featured gating tracks where 15-30% of all cardiac triggers were missed by the ECG gating. It is theorized that the increased prevalence of missed triggers in this subject population may

be due to their smaller size relative to the magnet bore when compared to adults. Greater freedom-of-motion allows for increased subject motion, especially during exercise, which could contribute to decreased gating fidelity, as outlined in the introduction to this work. Pulse oximetry did not offer a more robust gating solution when reliable ECG signals could not be obtained, as it proved to be highly sensitive to subject motion as well. As such motion would be difficult to minimize for future exercise studies, there may be value in investigating alternative gating methods, such as self-gating techniques [124,146,147].

The implemented ECG correction algorithm proved to be mostly effective at salvaging the scans for children with corrupted gating tracks. For most of the subjects, the algorithm effectively corrected abnormally long RR intervals to new intervals at the expected RR interval length. This proved to be effective at eliminating improperly high flow across the cardiac cycle by removing the second systolic peak in the reconstructed flow waveforms. Peak systolic flow was preserved suggesting the algorithm did not significantly alter the original systolic waveform. Good agreement was also observed in systolic flow profiles between the reconstructed waveforms with original and corrected gating. The most notable advantage this algorithm offered was the preservation of original image SNR. An alternative solution would be to simply discard projections associated with missed triggers, but given that some subjects had up to 50% of all triggers missed, this would result in significant SNR losses, rendering images difficult to interpret. One of the two cases which the algorithm failed featured numerous early triggers. These, alone and when coupled with subsequent missed triggers, resulted in triggers that could not be properly corrected for, as their lengths were not integer multiples of the expected RR window. For such cases, a combination of the ECG correction algorithm and rejection of projections associated with early triggers may provide the most accurate reconstruction.

The SNR analysis showed slightly decreased SNR during exercise in the child subjects than was observed in the adult subjects. It is hypothesized this may be from increased motion blurring present in these images. The ventricles and great vessels were still capable of being resolved and segmented in all images, however, so the additional SNR loss was not prohibitive to image analysis. Still, it was likely this SNR loss contributed to some increased variability in measurements of various hemodynamic parameters.

This additional SNR loss could have been compensated for by using a lower VENC in this subject population. For these acquisitions, the same VENC was used as in the adult subjects (200 cm/s), which was likely excessive given the naturally lower cardiac output in young subjects. Future studies should explore the use of VENCs tailored to the subject groups in question.

As in the adult subjects, SV showed weak sensitivity to exercise, likely due to the supine position in which the subjects were exercising. CO, mean flow, and mean velocity, on the other hand, were highly sensitive to increases with exercise stress, as was expected. At rest, flow parameters in the AAo and MPA showed excellent agreement and an expected Q_p/Q_s ratio around 1. Like in the adult subjects, however, flow parameters in the MPA were typically higher than that measured in the AAo – a non-physiologic situation for subjects with no inter-cardiac shunts. Investigation in the adult subjects suggested these discrepancies may be linked to greater sensitivity to SNR loss and/or differences in susceptibility to altered respiratory motion during exercise in the ascending aorta when compared to the MPA.

Kinetic energy measurements showed reduced kinetic energy and efficiency when compared to adult subjects, as expected for the smaller, still-developing hearts in children. Measurements during systole were more sensitive to significant changes with exercise than those during diastole. Similar trends were observed as in the adult subjects, where the LV was more efficient during systole, while the RV was more efficient during diastole.

The congruity of these results with those obtained in the healthy adults suggest 4D flow with PC VIPR can also be a valid tool for quantitative exercise CMR in healthy children. Children showed similar responses to exercise as adult subjects, but typically had lower magnitude in hemodynamic parameters given the smaller heart, ventricle volumes, and vessels. Increased motion proved to be a special challenge in imaging child subjects during exercise as compared to adults. The implemented gating correction algorithm seemed effective at salvaging flow waveforms corrupted by this excess motion, however. As the exercise equipment was tailored for use with grown adults, specialized adjustments for children (such as smaller strap-in boots and a smaller chest harness) could help decrease subject motion.

There were a few limitations with this study in addition to those already identified in the adult

population. As noted before, the sequence used was identical to that used for the adult subjects. Using VENCs and imaging volumes more tailored to the smaller size of children may improve SNR and image quality. In addition, children were generally less cooperative during exercise challenges than adults and were more likely to quit exercise before exhaustion. This introduced some uncertainty in establishing VO_{2max} prior to imaging, and likely resulted in a greater variance in achieved exercise power during MRI imaging. Finally, while increased SNR loss and decreased gating fidelity suggested increased motion during exercise in child subjects, no analysis was done to confirm this. Future studies should quantify the amount of motion present during exercise imaging to better understand the impact on image quality and repeatability.

6.2.4 Conclusions

This study demonstrated that whole-heart exercise CMR was possible in healthy children using 4D flow MRI. The children in this study showed similar hemodynamic response to exercise as observed in healthy adult subjects. Exercise studies with child subjects tended to have lower SNR and decreased gating quality when compared to those in adults due to increased bulk motion during exercise. A custom MATLAB algorithm proved capable of correcting for most gating errors and allowed for the reconstruction with more accurate flow waveforms. Future studies will focus on performing scans with equipment and sequences more tailored to the younger age and smaller body size in this population to improve image quality. Overall, however, the work presented in this chapter demonstrated that PC VIPR allows for robust, free-breathing acquisitions during exercise in both children and adults that are less susceptible to motion corruption than traditional sequences with breath holds.

Chapter 7: Exercise CMR in Preterm Children and Adults

The previous chapter demonstrated the feasibility of exercise CMR with PC VIPR in healthy adults and children. These free-breathing acquisitions showed improved robustness to motion over the traditional breath-held sequences explored in Chapter 4. This chapter extends this methodology to study cardiac performance in preterm adults and children, a population that may have increased risk for heart disease.

7.1 Background

Premature (or preterm) birth is a serious health problem, accounting for 12% of all births and contributing to more than 85% of all complications and death arising around the time of birth [148]. Preterm birth is defined as the birth of a baby earlier than 37 weeks of gestation, rather than the typical average of 40 weeks. As a result of underdeveloped lungs and airways, preterm babies often require mechanical ventilation and oxygen therapy [149]. Such therapies, however, can induce lung injuries and impair early airway development [150,151]. Recent advances, such as surfactant therapy [152], have improved short-term respiratory health, but it is unclear how long-term respiratory health, and cardiac health by extension, is affected by preterm birth due to previously low survival rates in this subject population.

Due to the therapies described above, a sizeable number of preterm subjects have now reached early adulthood, allowing for initial examinations on the long-term impacts of preterm birth on cardiopulmonary function. One such large-scale study in a group of healthy young adults (age 18-24) born preterm found this cohort had higher heart rates, higher systolic blood pressure, and lower diastolic blood pressure when compared to age-matched controls born at term [153]. A comparable study utilizing MRI imaging found that healthy adults born preterm featured smaller RV volumes but larger RV mass when compared to controls [154]. These results suggest preterm-birth infants may have an increased risk for cardiovascular disease later in life.

The fundamental differences in cardiac function for preterm-birth adults identified by the studies above is extremely concerning given their young age and the fact that they were otherwise considered to be medically healthy. The underlying mechanisms for this dysfunction is still largely not understood, however.

As a result, there is a need for robust biomarkers for understanding these mechanisms, aiding in early diagnosis, and monitoring disease progression over time. Continued studies with 4D flow MRI are well-suited for understanding this underlying dysfunction, as it allows for whole-heart imaging capturing flow dynamics in the great vessels and ventricles simultaneously. Furthermore, a wide range of potential biomarkers can be derived from a single 4D flow examination, including pressure, wall shear stress, and kinetic energy, among others. Coupling 4D flow exams with strenuous exercise challenges may also allow underlying cardiac dysfunction to be detected at younger ages, before symptoms become apparent.

In this study, a cohort of preterm young adults and children underwent exercise CMR with 4D flow MRI to detect and better understand any possible cardiac dysfunction. Flow was assessed in the aorta, main pulmonary artery, and the right and left ventricle. Results were compared to those in age-matched controls to assess differences associated with premature birth. It was hypothesized that flow field visualizations and quantification in the ventricles possible with 4D flow would help explain abnormal cardiac behavior observed in other studies.

7.2 Methods

Eleven preterm young adults (27 ± 1 years; 5 male, 6 female) and seventeen preterm children (13 ± 1 years; 6 male, 13 female) were recruited for this study. These subjects were recruited from the Newborn Lung Project cohort and were all born prior to 32 weeks of gestation at a birthweight below 1500 g. At the time of this study, these subjects were all free of overt cardiovascular and cardiopulmonary disease and had no physical limitations inhibiting exercise capabilities. These subject cohorts were age-matched to the healthy young adult and child cohorts recruited for the feasibility study described in the previous chapter. This study was approved by the local Institutional Review Board and was compliant with the Health Insurance Portability and Accountability Act.

Exercise Protocol: Exercise was conducted in a supine position in the magnet bore with the Ergospect stepper. The target exercise power for each subject was 70% of the power corresponding to each subject's VO_{2max}, as previously established on a bicycle ergometer in an exercise lab. Subjects were verbally

coached to step at a cadence of 60 steps/min for the duration of exercise. All exercise imaging was performed after subjects had been exercising at the target power output for at least 3 minutes and had achieved a steady-state heart rate.

4D Flow MRI Acquisition: Subjects were imaged on a clinical 3.0 T scanner (Discovery 750, GE Healthcare, Waukesha, WI) with an 8-channel cardiac coil. Cardiac 4D Flow MRI at rest and during exercise was performed with an identical radially-undersampled PC VIPR acquisition to that performed in the control subjects examined in Chapter 6 [43,44]: TR/TE = 6.2/2.0 ms; flip angle (FA) = 10°, velocity encoding (VENC) = 200 cm/s; field of view (FOV) = 32x32x32 cm; spatial resolution = 1.25 mm isotropic, scan time = 9.25 minutes). Images were reconstructed offline with retrospective respiratory gating from an abdominal belt to include only data during expiration with adaptive thresholding and 50% efficiency. Retrospective ECG gating was used for cine reconstruction [40,124]. Fifteen cardiac phases were reconstructed.

ECG Gating Correction: During the image reconstruction, the median RR interval length was calculated and the percentage of data acquired outside of this interval was presented. If more than 5% of the acquired projections were outside of this window, the gating correction algorithm described in Chapter 6 was applied to the ECG gating track in MATLAB. For subjects with corrected gating, the reconstruction described above was repeated with the new gating track.

4D Flow MRI Analysis (Flow): 4D Flow MRI complex difference images were segmented with MIMICS (Version 17.0, Materialize, Leuven, Belgium) to isolate the ascending aorta (AAo) and main pulmonary artery (MPA). Flow quantification was performed using a combination of Ensight (Version 10.0, CEI Inc. Apex, NC), to generate two-dimensional, time-resolved magnitude and phase contrast datasets perpendicular to the vessel orientation, and a custom MATLAB tool [126], to quantify the flow through the AAo and MPA. Stroke volume (SV), cardiac output (CO), mean velocity, and mean flow were recorded in the AAo and MPA.

4D Flow MRI Analysis (Kinetic Energy): The LV and RV were segmented from the time-averaged magnitude images in MIMICS [127]. A custom script applied this mask to the time-resolved velocity

images to extract the velocity magnitude for each voxel in the ventricle. Ventricular KE was calculated from the sum of the KE for the voxels within the segmented volume using the previously described KE formula (Eq. 6-1). Ventricular energy efficiency was defined as the SV normalized to the KE, $\eta = \frac{SV}{KE}$. To minimize the influence of heart rate on comparisons, KE and η were assessed at peak systole and peak diastole, rather than across the entire cardiac cycle.

Ventricular Vortex Analysis: To better understand differences in flow dynamics between control and preterm subjects, pathline and streamline visualizations were performed in the LV and RV. To remove ventricle size and SV as a confounding factor for differences in flow behavior, only control and preterm subjects with similar stroke volumes (within 5%) were compared to one another. Differences in flow fields were qualitatively assessed at different stages of the cardiac cycle. To quantify differences in ventricular flow fields, total vorticity was calculated across each ventricular volume using Eq. 7-1.

$$\boldsymbol{\omega} = \nabla \times \boldsymbol{u} \qquad \textit{Eq. 7-1}$$

where $\boldsymbol{\omega}$ is the vorticity vector, ∇ is the del operator, and $\boldsymbol{u}$ is the velocity field. To minimize ventricle size as a confounding factor in comparisons, vorticity was normalized by SV for each subject. Due to the nature of the curl computation, vorticity calculation can be very sensitive to the presence of noise in low flow regions of the ventricle. As a result, additional calculations were performed where the normalized vorticity in each voxel was multiplied by the velocity magnitude in that voxel, to de-emphasize voxels with low flow.

Statistical Analysis: Unless stated otherwise, all parameters are presented as the mean sample value plus/minus the sample standard deviation. Statistically significant differences in these parameters between rest and during exercise were determined with a paired student's t-test ($\alpha = 0.05$). A one-way ANOVA analysis with Tukey's HSD test was conducted to determine statistically significant differences between the four cohorts.

7.3 Results

Ten of eleven preterm adults and sixteen of seventeen preterm children successfully completed exercise

imaging. The adult who could not complete imaging complained of increased feelings of claustrophobia during exercise imaging, while the child simply could not maintain focus for the extended scanning session. Table 7-1 compares the mean exercise power corresponding to 70% VO_{2max} for each cohort, and the mean heart rate increases associated these exercise powers. Preterm subjects had lower exercise powers corresponding to 70% VO_{2max} for comparable increases in heart rate when compared to the age-matched control groups.

Cohort	Mean Power [W]	Mean HR Increase [bpm]
Adult - Control	153 ± 36	28 (↑45%)
Adult - Preterm	131 ± 24	28 (↑37%)
Child - Control	107 ± 24	35 (↑45%)
Child - Preterm	87 ± 19	28 (↑35%)

Table 7-1: Mean exercise powers corresponding to 70% of each cohort's VO_{2max} and associated heart rate increases when compared to rest.

ECG Gating Correction: Two preterm adults and two preterm children had noticeably corrupted ECG gating (more than 5% of projections detected outside median RR interval) at rest. Seven of ten preterm adults and 12 of 16 preterm children who completed exercise imaging had corrupted ECG gating during exercise. The ECG correction algorithm proved effective at correcting these gating tracks below the desired 5% threshold in 22 out of 23 cases.

4D Flow MRI Analysis (Flow): Measurements for the control groups have been previously presented in Chapter 6. Table 7-2 presents the mean values for cardiac output, stroke volume, and mean velocity at rest and stress in all cohorts, as measured in the aorta and MPA. Figure 7-1 shows distributions for CO, SV, and mean velocity in each cohort at rest and during exercise. Cardiac output was highly sensitive to exercise, with statistically significant increases observed in almost all cohorts in both the aorta and MPA. In the aorta, PC VIPR measurements showed average increases in CO with exercise of 49%, 33%, 27%, and 16% in the adult controls, adult preterms, child controls, and child preterms respectively. MPA flow showed slightly greater increases of 63%, 43%, 50%, and 33%.

			Adult-Control	Adult-Preterm	Child-Control	Child-Preterm
Cardiac Output [L/min]	Aorta	Rest	4.7 ± 0.5	4.9 ± 1.0	4.5 ± 0.8	3.8 ± 0.8
		Exercise	7.0 ± 1.4	6.5 ± 1.4	5.7 ± 1.0	4.4 ± 2.1
	MPA	Rest	4.9 ± 0.8	5.4 ± 0.9	4.6 ± 0.8	4.2 ± 1.3
		Exercise	8.0 ± 1.4	7.7 ± 1.3	6.9 ± 1.0	5.6 ± 2.1
Stroke Volume [mL]	Aorta	Rest	75 ± 12	66 ± 15	57 ± 9	48 ± 13
		Exercise	81 ± 27	64 ± 18	50 ± 11	38 ± 19
	MPA	Rest	79 ± 13	72 ± 11	58 ± 9	53 ± 16
		Exercise	93 ± 29	75 ± 14	61 ± 10	48 ± 20
Mean Velocity [cm/s]	Aorta	Rest	12.9 ± 1.9	13.2 ± 2.2	16.4 ± 3.0	14.6 ± 1.9
		Exercise	18.6 ± 4.0	16.9 ± 3.3	19.6 ± 3.9	16.8 ± 4.2
	MPA	Rest	12.7 ± 2.2	16.0 ± 9.6	14.3 ± 2.1	13.9 ± 2.7
		Exercise	19.8 ± 5.0	21.1 ± 2.3	19.5 ± 3.6	18.1 ± 3.8

Table 7-2: Mean values for cardiac output, stroke volume, and mean velocity at rest and during exercise in each cohort as measured in the ascending aorta and main pulmonary artery.

The control subjects and preterm subjects tended to display different mechanisms for increasing their CO in response to exercise. Control subjects tended to show increases in both HR and SV in response to exercise, while preterm subjects were more likely to rely only on increases in HR with no change (or a slight decrease) in SV. These different mechanisms were more noticeable in the adult subjects. Table 7-3 shows the average increase in HR and SV with exercise for each cohort. The distributions for both CO and SV were increasingly lower as a function of both subject age and birth time. Adults subjects tended to have higher CO and SV than child subjects. Term subjects also tended to have higher CO and SV than age-matched subjects born preterm.

Mean velocity was also sensitive to exercise, showing statistically significant increases in all cohorts. Similar increases were observed in both the Ao and MPA. In the Ao, increases of 44%, 28%, 20%, and 15% were measured in the adult controls, adult preterms, child controls, and child preterms respectively. In the MPA, increases of 56%, 32%, 36%, and 30% were observed.

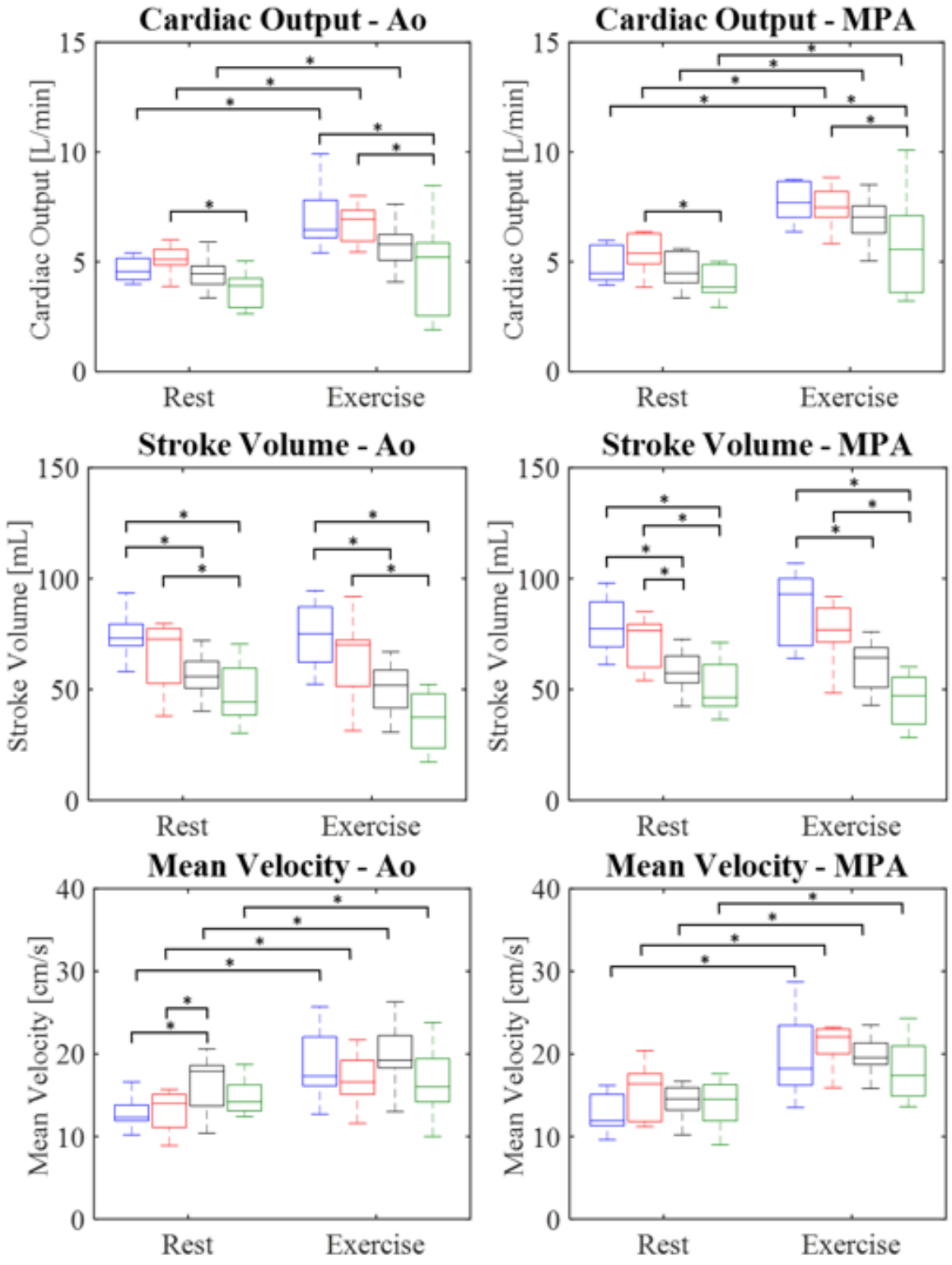

Figure 7-1: Distributions of cardiac output, stroke volume, and mean velocity as measured in the aorta and MPA in all cohorts at rest and during exercise. From left to right, the boxplots represent the adult controls (blue), adult preterm (red), child controls (black), and child preterm (green). A bracket between two boxplots denotes a statistically significant difference ($p<0.05$).

Cohort	HR Change	SV Change (RV/LV)
Adult - Control	↑45%	↑18% / ↑8%
Adult - Preterm	↑37%	↑4% / ↓4%
Child - Control	↑45%	↑5% / ↓12%
Child - Preterm	↑35%	↓10% / ↓21%

Table 7-3: Mechanisms for increasing cardiac output in response to exercise. Control subjects tended to rely more on a balanced increase of both heart rate and stroke volume to increase cardiac output, whereas preterm subjects were more likely to rely only on heart rate.

4D Flow MRI Analysis (Kinetic Energy): Table 7-4 presents the measurements for KE and KE efficiency, η, in the LV and RV for all cohort groups. KE showed significant increases with exercise for most subject groups. Measurements in adult subjects were generally higher than those in child subjects, but minimal differences were observed between age-matched control and preterm groups. For most measurement distributions, KE_{RV} was similar to KE_{LV}.

			Adult-Control	Adult-Preterm	Child-Control	Child-Preterm
KE - Systole [mJ]	LV	Rest	4.3 ± 1.8	8.2 ± 4.2	3.2 ± 1.5	3.8 ± 1.4
		Exercise	9.0 ± 6.8	11.0 ± 6.1	5.7 ± 2.3	5.0 ± 2.5
	RV	Rest	8.3 ± 2.3	10.9 ± 3.3	5.6 ± 3.3	5.5 ± 3.1
		Exercise	12.6 ± 4.5	13.1 ± 4.5	7.7 ± 3.3	7.0 ± 2.6
KE - Diastole [mJ]	LV	Rest	6.9 ± 2.1	10.3 ± 3.3	6.2 ± 2.2	7.2 ± 2.8
		Exercise	8.5 ± 4.0	10.6 ± 4.1	7.5 ± 2.8	9.2 ± 5.3
	RV	Rest	5.7 ± 1.2	6.2 ± 0.7	4.3 ± 1.0	6.1 ± 4.4
		Exercise	9.7 ± 5.5	11.6 ± 4.1	7.0 ± 2.4	8.5 ± 5.0
η - Systole [mL/mJ]	LV	Rest	18.6 ± 5.3	10.2 ± 4.4	20.4 ± 7.5	14.6 ± 5.6
		Exercise	10.8 ± 5.2	8.1 ± 4.8	10.5 ± 5.7	11.4 ± 10.9
	RV	Rest	9.7 ± 2.3	7.3 ± 2.0	12.0 ± 3.6	11.5 ± 4.9
		Exercise	7.3 ± 2.4	6.4 ± 1.8	9.3 ± 5.2	7.3 ± 2.3
η - Diastole [mL/mJ]	LV	Rest	11.1 ± 2.4	7.4 ± 2.7	9.7 ± 2.3	7.5 ± 2.4
		Exercise	10.6 ± 5.5	7.3 ± 3.3	8.2 ± 5.5	4.8 ± 1.8
	RV	Rest	13.9 ± 2.9	12.2 ± 2.3	13.6 ± 2.3	11.3 ± 5.5
		Exercise	11.2 ± 5.5	7.5 ± 2.7	9.6 ± 3.7	6.3 ± 1.9

Table 7-4: KE and KE efficiency, η, in the LV and RV at both rest and exercise for all subject groups. Measurements are presented for time frames corresponding to end-systole and end-diastole.

Kinetic energy efficiency was a more robust metric in identifying possible differences in cardiac function between these subject groups. Figure 7-2 shows the distributions of this parameter in the LV and RV for all cohorts. Results are presented for both end-systole and end-diastole.

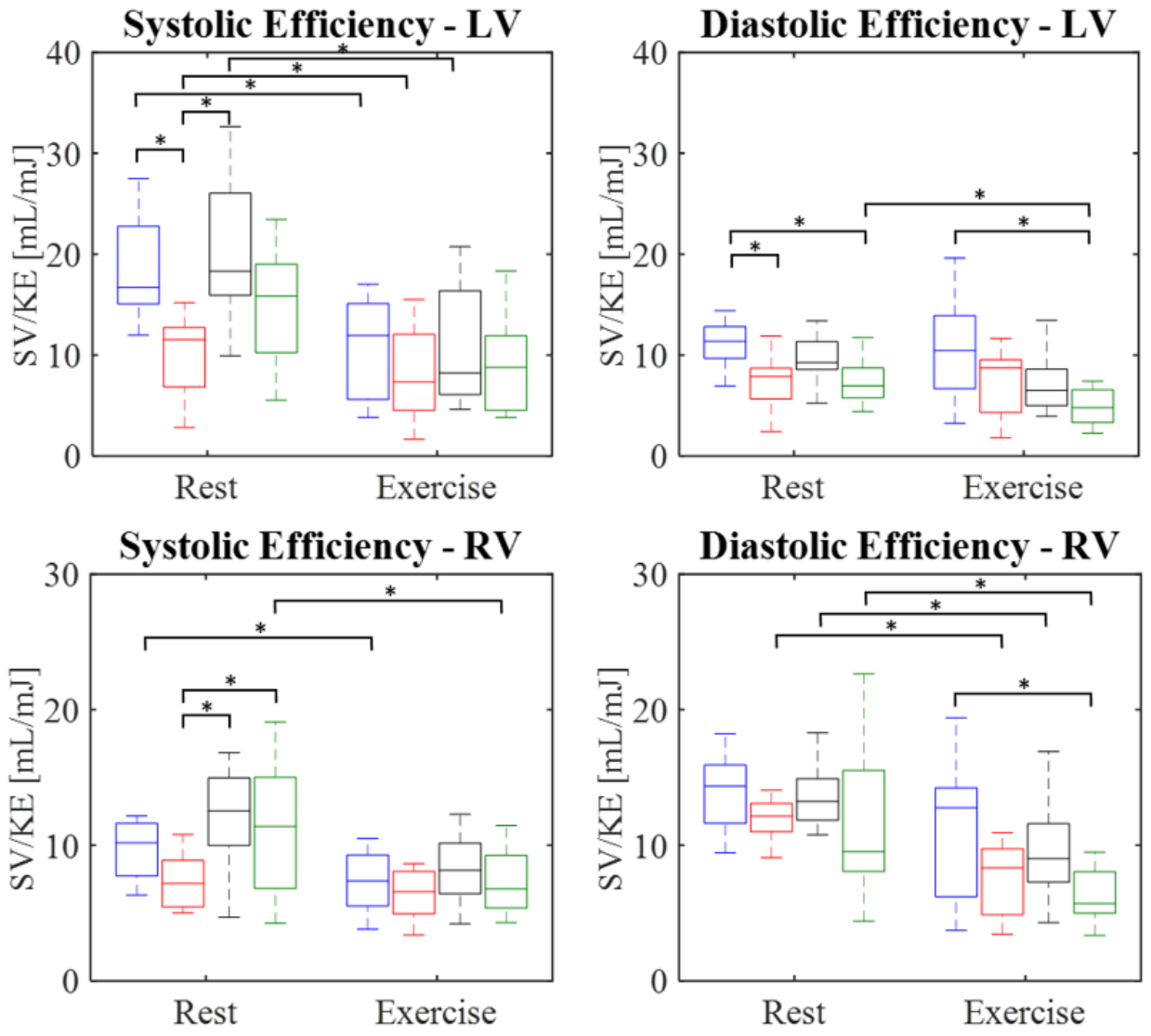

Figure 7-2: Distributions of kinetic energy efficiency in the RV and LV at end-systole and end-diastole in all four subject cohorts. Results are presented at rest and during exercise. From left-to-right, the distributions represent adult controls (blue), adult preterms (red), child controls (black), and child preterms (green).

Although not always significant, KE efficiency distributions in preterm subjects in all cases were lower relative to age-matched term controls. These relationships were preserved, and enhanced in many situations, with exercise. Preterm subjects showed greater reductions in diastolic efficiency relative to term controls than systolic efficiency.

Ventricular Vortex Analysis: Streamline analysis was performed in the LV and RV to better understand possible variations in flow dynamics resulting in the reduced kinetic energy efficiency in preterm subjects. Figure 7-3 shows a representative example of streamline visualizations in the RV of an adult control and adult preterm subject with similar stroke volumes. In the RV, controls subjects tended to display well-structured diastolic filling vortices. This was not the case in preterm subjects, where less-structured vortices with more chaotic flow were common. Streamline analysis in the LV did not find any consistent differences in flow dynamics between control and preterm groups.

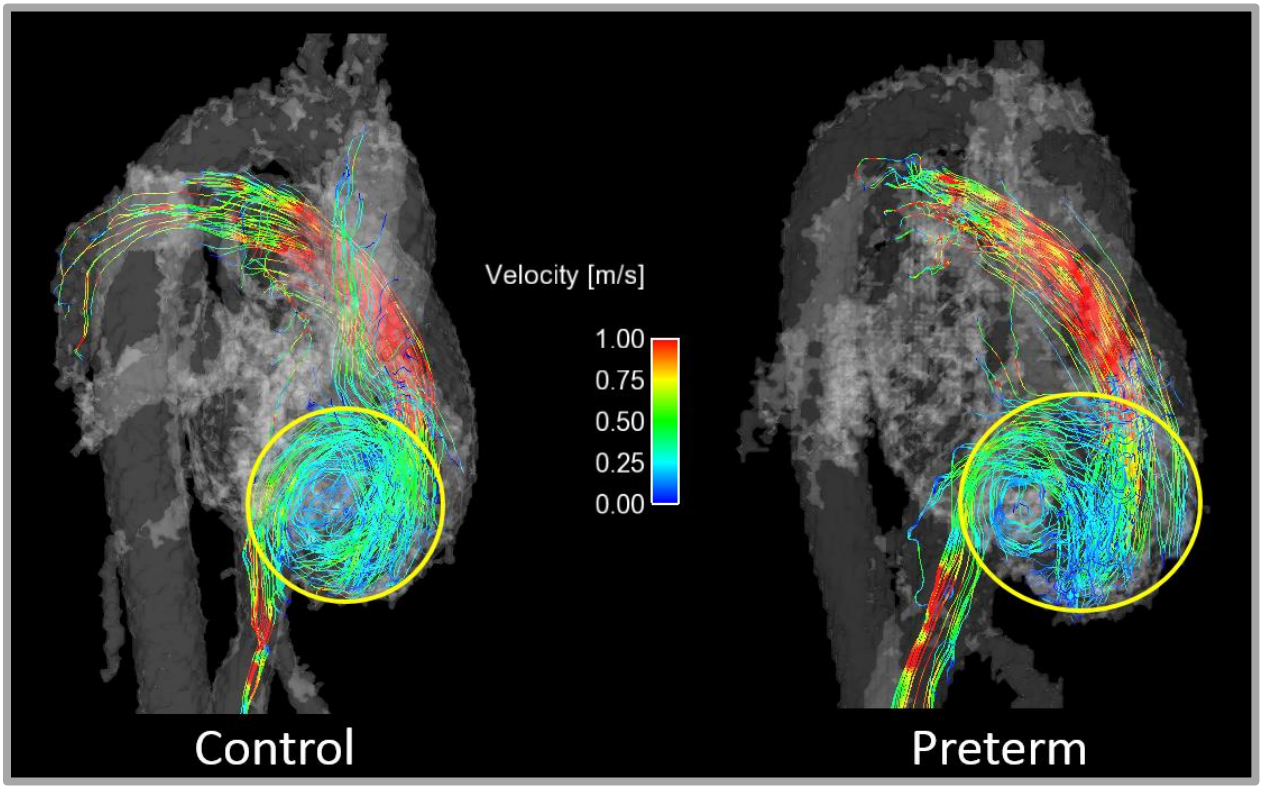

Figure 7-3: Representative streamline visualization in the RV for an adult control and adult preterm subject with similar stroke volumes. Control subjects tended to have better-structured filling vortices, while preterm subjects had filling vortices with more chaotic flow.

Vorticity measurements also suggested fundamental differences in RV vortex dynamics, as shown in Figure 7-4. Total vorticity normalized by SV showed slightly elevated values in preterm subjects when compared to age-matched controls. Vorticity scaled by velocity magnitude in each voxel, however, proved much more sensitive, with noticeable (and many more significant) differences between groups. These measurements showed both an age dependence and cohort dependence on scaled vorticity measurements. Greater differences between control and preterm subjects were observed for measurements during diastole, consistent with that noted in the qualitative streamline analysis.

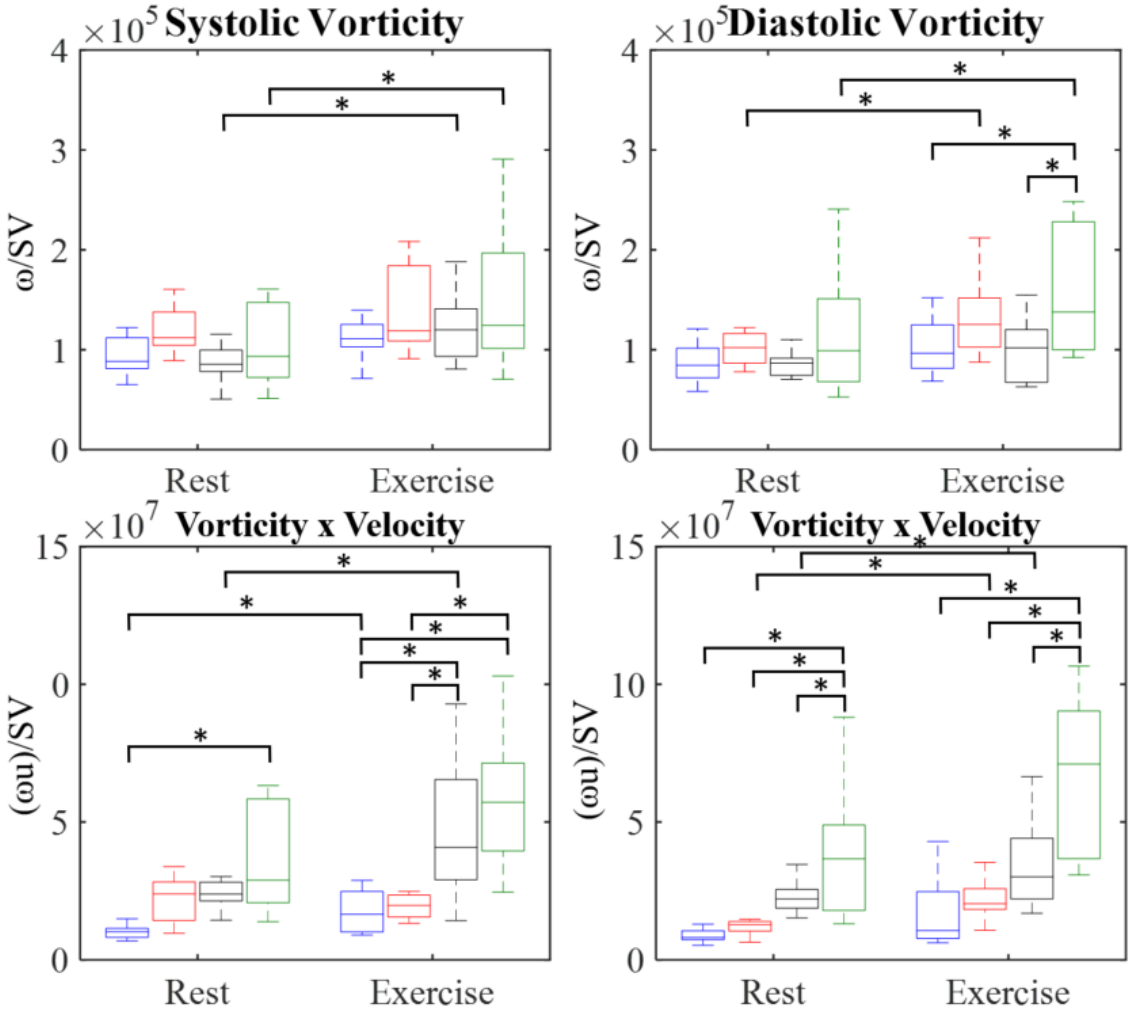

Figure 7-4: (Top row) Measurements of vorticity in the RV during systole and diastole. (Bottom row) Vorticity measurements during systole and diastole scaled by velocity magnitude in each voxel. From left to right, the boxplots represent adult controls (blue), adult preterm (red), child controls (black), and child preterm (green). A bracket between two boxplots denotes statistical significance.

7.4 Discussion

The high success rate of exercise imaging in this study continued to show the viability of exercise power corresponding to 70% VO_{2max} as an individualized metric that was feasible for subjects of all exercise capabilities. While such a protocol has yet to be tested in subject with prevalent cardiac disease and severely inhibited cardiac function, the previous feasibility of low exercise power exams demonstrated in patients with pulmonary hypertension (Chapter 4) suggests some level of exercise power may be sustainable in almost all patient populations. The drawback of using 70% VO_{2max} as a guideline for exercise power is it requires subjects to come in for two sessions – one to establish VO_{2max} and another to perform exercise imaging. This could prove prohibitively difficult for studies that aim to investigate patients who may have difficulty traveling due to limited cardiac capabilities or patients who must travel from far away to participate. In this study, the preterm subjects demonstrated consistently lower powers corresponding to 70% of their VO_{2mx}, the first indication they may have altered cardiac function relative to term controls.

The preterm subjects seemed more susceptible to corrupted ECG gating tracks than their age-matched term controls. Seven of ten preterm adults required gating correction, whereas none of the corresponding term controls required this. Likewise, twelve of sixteen preterm children that completed exercise imaging required gating correction as compared to only seven of eighteen in the healthy child controls. In the previous chapter is was suggested that compromised gating in the term child subjects was a result of their smaller body sizes and thus increased range of motion in the magnet bore. These results suggest preterm birth may also introduce some factors affecting gating fidelity. It is unclear if this is due to increased motion in the scanner from a greater perceived difficult of exercise challenges and discomfort, altered cardiac function, or something else. Overall, the gating correction algorithm was very effective in these subjects, able to correct all cases but one.

As demonstrated, the preterm subjects tended to show a different mechanisms for increasing their cardiac output in response to exercise. Rather than a balanced increase in both HR and SV, they relied almost entirely on HR increases. Many preterm subjects even had measured decreases in SV with exercise.

It is likely some of the blunted SV response is due to reduced changes in SV naturally associated with supine exercise [128]. Even with this consideration, however, preterm subject showed reduced changes relative to term controls. This reliance on increasing only HR to raise CO is concerning, as it consistent with that observed in many right-heart diseases, such as pulmonary hypertension [118], and suggests a reduced cardiac reserve in these subjects.

While KE was not an effective metric for identifying differences between term and preterm groups, KE efficiency (SV/KE) presented more noticeable differences. Normalizing KE against SV likely removed differences in ventricle size between subjects as a confounding factor. It is worth investigating in future studies if normalizing against end-diastolic and end-systolic ventricular volumes, rather than the SV integrated across the entire cardiac cycle, improves sensitivity. Such measurements are difficult to obtain from 4D flow MRI magnitude images, however, and may require registration of higher SNR bSSFP images for more accurate quantification.

The consistently lower KE efficiency measurements in preterm subjects relative to term controls again suggested fundamental differences in cardiac function between these two groups. This lower efficiency was consistent with that observed in strain measurements performed from bSSFP acquisitions in the same subjects [155]. These measurements are shown in Figure 7-4. The strain measurements showed increased circumferential strain and decreased strain efficiency (SV/strain) in the preterm adults as compared to the term controls. This indicates ventricular hyper-contractility, where preterm hearts are contracting more to achieve the same SV as in healthy controls. This inefficiency is in line with the decreased energy efficiency measured with PC VIPR. As shown in Figure 7-4c, preterm subjects also required increased time to reach end-systole and exhibited slower recovery during diastole. These results, coupled with the fact that diastolic KE efficiency measurements had the greatest disparity between term and preterm subjects, suggested these preterm subjects could have some underlying diastolic dysfunction.

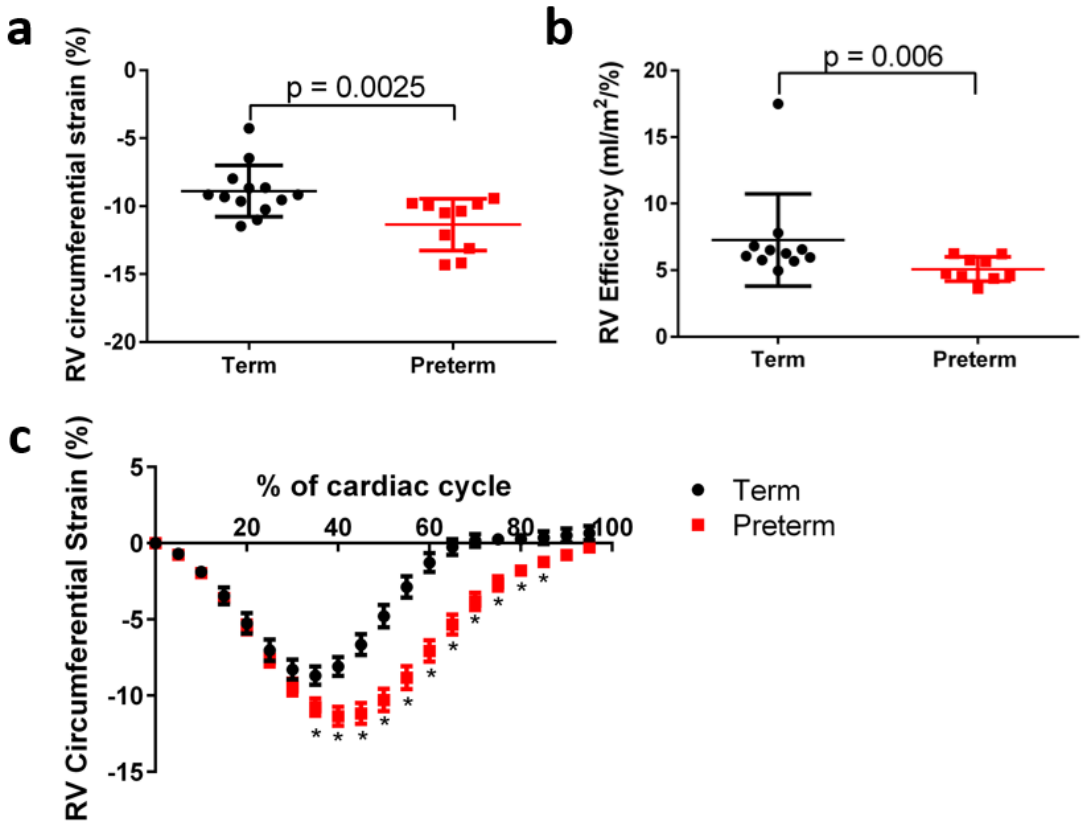

Figure 7-5: (a) RV circumferential strain, (b) RV strain efficiency (SV/strain), and (c) average strain profiles over the cardiac cycle for term and preterm adults. Plots courtesy Greg Barton.

The streamline analysis supported this hypothesis. While minimal differences were observed in LV streamlines between subject cohorts, preterm subjects had noticeably less structured diastolic filling vortices in their RV. This is a significant finding, as diastolic filling vortices have been hypothesized to be an important mechanism for dissipating excess KE from flow entering the ventricle. If this in-flowing KE is not properly dissipated, it may otherwise contribute to an inflow-impeding convective pressure rise in the ventricle [137]. Such a pressure increase could account for the increased strain and decreased energy efficiency observed in these subjects.

Vorticity scaled by velocity magnitude seemed to be an effective parameter for quantifying these differences in vortex behavior amongst cohorts, while vorticity alone had limited sensitivity and showed poor sensitivity to differences between groups. This was likely because the curl calculation inherent to

vorticity analysis was highly sensitive regions of low VNR, an issue compounded by the suboptimal VENC of this PC VIPR sequence for ventricular flow analysis. The scaled vorticity effectively minimized the impact of noise, by exaggerating the curl from voxels with high velocities less affected by noise. The drawback is that such a parameter is non-physical and results are thus harder to interpret on their own. A close alternative could be to calculate helicity, the dot product of velocity and vorticity, a better defined fluid mechanics parameter. More specific segmentation of only the region of the ventricle containing the vortex, rather than the entire ventricle, could also be employed to improve the sensitivity of vorticity measurements. The use of Lagrangian coherent structures to delineate vortex volumes, as pioneered in MRI by the Lund group [56], could be an effective means to isolate the vortex volume in the ventricle.

This study had a few limitations beyond the technical aspects reported on in the previous chapter. First of all, although there were striking differences in many hemodynamic parameters between term and preterm adults and children, the sample sizes are too small to draw definitive conclusions. In addition, the ventricular energy efficiency measurements may have reduced accuracy from segmentation on magnitude 4D flow images, which do not have good contrast between the myocardium and blood pool. Finally, looking only at 4D flow measurements and bSSFP strain measurements provides an incomplete picture of total cardiac function. There would be great value in future studies with quantitative T1 or T2 sequences to identify differences in myocardial structure between these subject groups.

7.5 Conclusions

This study demonstrated the feasibility of 4D flow MRI to better understand possible mechanisms for cardiac dysfunction in subjects born preterm and the potential of high-power exercise CMR as a tool for characterizing abnormal cardiac dynamics in patient populations. A mechanism for increasing cardiac output similar to that observed in many right-heart diseases was detected, and kinetic energy efficiency measurements in the ventricles showed decreased efficiency in preterm subjects relative to age-matched term subjects. Streamline analysis in the RV suggested this decreased efficiency may be the product of less structured diastolic filling vortices in preterm subjects. As of now, it is unclear if these altered vortices are

the result of previously reported increased ventricular strain and wall thickness [154] in these subjects or vice versa. Overall, it is very concerning that such striking differences were observed between term and preterm subjects, even in children, especially considering they were otherwise considered to be healthy. These results lend further credence to the hypothesis that these subjects may be at increased risk for cardiovascular disease later in life.

Chapter 8: Summary and Recommendations

8.1 Summary of Research Findings

4D flow MRI has been well-established as a powerful tool for characterizing and quantifying complex cardiovascular flow dynamics. These sequences have been validated in research and clinical settings for cardiac, cranial, hepatic, and renal applications, where motion can be well compensated for with respiratory and cardiac gating. Although 4D flow can offer enhanced flow information for a variety of pathologies, due to some limitations, Doppler US is still the clinical standard for many types of flow measurements, including pregnancy imaging and cardiac exercise stress imaging. The work presented in this thesis extended the utility of 4D flow MRI to these novel applications, with a special focus on imaging throughout early-life development. Specific contributions of this work include:

- Feasibility analysis of 4D flow MRI during pregnancy to quantify blood flow in the uteroplacental and fetal vessels in the rhesus macaque. The main uteroplacental vessels could be reliably imaged by the late 1st trimester of gestations, while the fetal vasculature could be visualized by the late 2nd trimester.
- Feasibility analysis of traditional MRI techniques for cardiac exercise studies. Breath-held sequences proved unreliable for imaging following exercise, given the difficulty of the breath holds in patient populations with limited cardiac capacity.
- Implementation of an MR-compatible stepper for high-power exercise challenges in pediatric and adult populations.
- Implementation of strenuous 4D flow MRI exercise exams in pediatric and adult populations during, rather than after, exercise. A custom-made gating-correction algorithm was required to improve gating signal fidelity due to decreased gating reliability from the increased motion inherent to exercise.
- Assessment of flow dynamics in the hearts of adults and children born preterm with 4D flow exercise CMR. Analysis in the ventricles showed decreased energy efficiency in preterm subjects,

possibly because of poorly structured diastolic filling vortices.

8.2 Innovations of this Work

The work presented in this dissertation involved a variety of innovations over that previously done in the field. Notable innovations are as follows:

- This was the first time 4D flow MRI was ever attempted to characterize uteroplacental and fetal flow during pregnancy. Only a few previous attempts with 2D PC techniques have been published and featured notable limitations. The PC VIPR sequence was able to overcome these limitations.
- The implemented Ergospect stepper for high-power exercise challenges was the first ever designed for GE scanners and the first ever in North America. This required a variety of unique adjustments and calibrations for the equipment not required in previous designs for Siemens systems.
- The feasibility of 4D flow MRI during strenuous exercise was proven for the first time in young adults and children through utilization of an inherently motion-robust PC VIPR acquisition. Previous attempts at exercise CMR were generally limited to imaging post-exercise (due to increased motion) at lower exercise powers (due to hardware constraints).
- A novel ECG gating correction algorithm was designed and implemented, which allows data associated with a poor gating signal to be salvaged and corrected, preserving image SNR.
- A unique 4D flow analysis of kinetic energy efficiency alongside streamlines in the ventricles during exercise was able to show previously unknown cardiac dysfunction with respect to diastolic filling vortices in subjects born preterm.

This research has been pioneering work at the forefront of two fields of MRI with rapidly growing interest. Since this work began, two MRI societies, ISMRM and SCMR, have created study groups devoted to placental and fetal imaging. Furthermore, Dr. Chris Francois, who collaborated and advised on much of this research, was welcomed to the 2018 SCMR Annual Meeting to give an invited lecture on our experiences with 4D flow MRI during exercise. ISMRM has also recognized abstracts on the exercise work with their magna cum laude and summa cum laude honors.

8.3 Recommendations for Future Work

The work presented in this thesis represents the first use of 4D flow MRI for two unique applications: uteroplacental/fetal imaging during pregnancy and cardiac imaging during exercise. The early results presented in this dissertation suggested great promise and utility of these techniques, but there were some notable limitations that should be the focus of future investigations.

Flow quantification in the uteroplacental vessels showed acceptable mean differences in flow between repeated measurements and different observers but featured large ranges corresponding to the 95% limit of agreement in measurements. This range was typically the same magnitude as the median flow measured in the vessels of interest. This is an important limitation for the proposed use of 4D flow to detect abnormal flow associated with pregnancy complications, as only systemic differences between groups larger than the limits of agreement can be reliably observed. Thus, the large limits of agreement in the rhesus macaque may suggest limited ability to detect flow abnormalities in this animal model, although this large range may be a function of the small sample size in this study. The recruitment of larger subject groups for future studies should improve statistical sensitivity differences between groups. Furthermore, uteroplacental flow normalized by maternal cardiac output or placental volume may offer a better representation of placental insufficiency which could improve the diagnostic potential of this technique. Poor agreement was also noted between flow measurements on consecutive days. Possible flow redistribution between imaging sessions due to fetal movement should be accounted for by assessing measurements of total uterine flow, rather than flow in individual vessels. Care should be taken to eliminate other confounding factors such as diurnal flow variations and altered hydration levels between imaging sessions, and the impact of these factors on measurement repeatability should be quantified. This is especially important for possible longitudinal studies, where these extraneous factors could obscure changes in flow from changes in placenta physiology. As this work translates to pilot studies in pregnant humans, work should focus on optimizing the scanning protocol and post-processing techniques to reduce measurement variability and the limits of agreement.

While the exercise imaging showed excellent repeatability in 4D flow measurements in the aorta and MPA, poor inter-observer and intra-observer agreement was observed for KE in the ventricles. Once again, large limits of agreement relative to the measured KE suggested poor clinical utility for identifying disease-altered dynamics with the current implementation of this analysis. Future work should focus on improvements for intra-ventricular flow analysis. This may be addressed through improved VNR via a courser spatial resolution, a detailed segmentation protocol to reduce differences in technique between observers, and approaches allowing for time-resolved ventricle segmentations (discussed in more detail below). Continued work with 4D flow exercise CMR should also investigate the prevalence of bulk subject motion during exercise and the impact on flow measurements and gating. Real-time coronal acquisitions with low spatial resolution could be used to characterize this motion. Subject motion could be correlated to gating quality.

Specific recommendations for advancing the investigated imaging techniques include:

8.3.1 Human Placenta Imaging

This work proved the feasibility of uteroplacental and fetal imaging in the pregnant rhesus macaque but benefited from sedation of both the mother and fetus during imaging. Such sedation will not be possible as this work is translated into human subjects. While it is anticipated that motion of the uteroplacental vessels can be limited through respiratory gating and coaching of the mother, such techniques are not possible with the fetus. Accelerated imaging or taking advantage of physiology (i.e. imaging when the fetus has relaxed following a maternal meal) may be required to adequately capture fetal flow. In addition to the recommendations summarized above, the use of protocols with optimized velocity-encoding and contrast (ferumoxytol) should be investigated to improve VNR and reduce variability in flow measurements.

8.3.2 Improved Physiologic Gating

Physiologic gating, especially ECG gating, proved unreliable during exercise imaging, presumably due to increased motion. Although the gating correction algorithm was effective at limiting the impact of poor gating, there were a few instances that could not be fixed. Thus, there seems to be a need for more robust

gating techniques during exercise imaging. Solutions could include alternative gating hardware designed for regions of the body less prone to motion, such as the ear gating used in many animal studies. Self-gating and self-navigation algorithms [146] could eliminate the need for gating hardware entirely if the algorithms can prove robust in the reduced SNR associated with exercise. Machine learning techniques may also provide an opportunity to acquire robust gating signals inherently from acquired image data.

8.3.3 Real-time Imaging during Exercise

The implementation of real-time PC imaging during exercise could both eliminate the need for physiologic gating while still allowing for free-breathing exams and provide valuable complementary information to that acquired with 4D flow techniques. Real-time flow imaging could quantify beat-to-beat variations in flow and quantify recovery to baseline following cessation of exercise, which could provide valuable diagnostic and prognostic information. A golden-angle radial trajectory would allow for motion robust acquisitions with variable temporal resolution reconstructions. Two reconstructions that hold promise for real-time PC imaging include the MOCCO algorithm [156] and a modified 2D STELLR approach [157].

8.3.4 Improved Ventricular Analysis Techniques

The sensitivity of the ventricular flow analysis in the exercise studies could likely be improved with a few modifications to the PC VIPR acquisition and post-processing. A reduced spatial resolution would still allow for good coverage of the ventricles and improve image SNR. Furthermore, the VENC of the 4D flow acquisitions in these studies was set to 200 cm/s to adequately characterize elevated aortic flow during exercise. This resulted in low VNR in the ventricles where flow was noticeably lower. Future studies with a lower VENC could improve VNR in the ventricles, while phase unwrapping algorithms [158] could correct aliased velocities in the great vessels if required. Further de-noising of ventricular flow could be achieved with divergence-free enforcement algorithms. Early results with a divergence-free wavelet transform [159] have shown promise in RV flow during exercise, as seen in Figure 8-1.

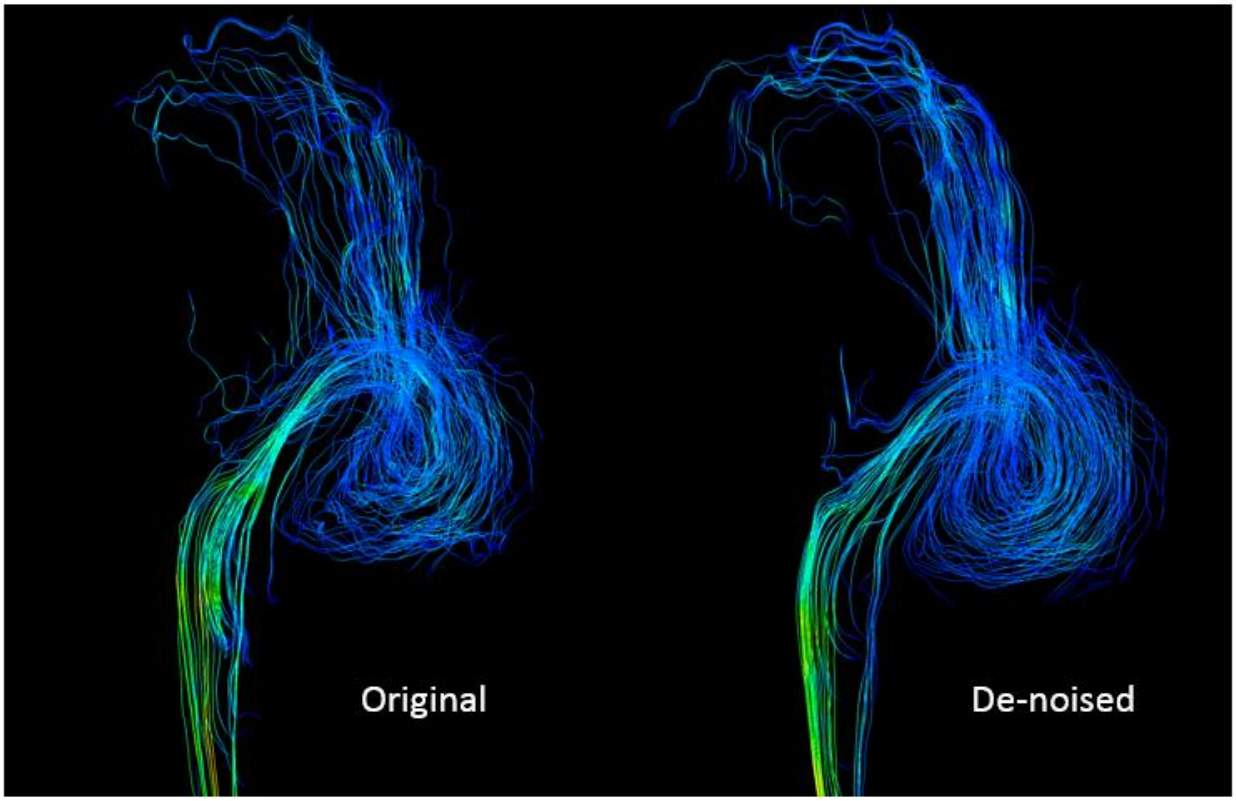

Figure 8-1: Application of a divergence-free wavelet transform to de-noise RV flow during exercise. The de-noised flow fields showed improved streamline quality in the diastolic filling vortex of the RV.

The time-resolved ventricular flow analysis could also be improved through the implementation of a time-resolved segmentation, rather than the time-averaged mask used in this work. The time-averaged mask was used out of necessity from poor image contrast when attempting to segment myocardial walls from time-resolved PC VIPR magnitude images. A significantly improved time-resolved segmentation could be achieved with bSSFP images, which feature exquisite myocardium/blood contrast, in the same subjects. If such a segmentation could be registered to time-resolved PC VIPR images, improved systolic and diastolic analysis could be completed. Others have also demonstrated that ferumoxytol-enhanced 4D flow imaging can provide the necessary SNR boost for accurate time-resolved segmentation of the ventricles [160].

References

[1] Luypaert R, Boujraf S, Sourbron S, Osteaux M. Diffusion and perfusion MRI: basic physics. Eur J Radiol 2001;38:19–27.

[2] Low G, Kruse SA, Lomas DJ. General review of magnetic resonance elastography. World J Radiol 2016;8:59. doi:10.4329/wjr.v8.i1.59.

[3] Nayak KS, Nielsen J-F, Bernstein MA, Markl M, D. Gatehouse P, M. Botnar R, et al. Cardiovascular magnetic resonance phase contrast imaging. J Cardiovasc Magn Reson 2015;17:71. doi:10.1186/s12968-015-0172-7.

[4] Taylor K, Burns P, Well P. Clinical applications of doppler ultrasound. 1987.

[5] Dyverfeldt P, Bissell M, Barker AJ, Bolger AF, Carlhäll C-J, Ebbers T, et al. 4D flow cardiovascular magnetic resonance consensus statement. J Cardiovasc Magn Reson 2015;17:72. doi:10.1186/s12968-015-0174-5.

[6] Markl M, Frydrychowicz A, Kozerke S, Hope M, Wieben O. 4D flow MRI. J Magn Reson Imaging 2012;36:1015–36. doi:10.1002/jmri.23632.

[7] Macdonald J, Skopos S, Johnson K, Ludwig K, Fain S, Reeder S, et al. Magnetic Resonance Imaging of Utero-Placental Vascular Flow and Tissue Perfusion in Pregnant Rhesus Macaques. Proc 2016 IFPA Annu Meet 2016.

[8] Macdonald J, Nguyen S, Johnson K, Corrado P, Fain S, Francois C, et al. Ferumoxytol Imaging at the Maternal-Fetal Interface. Proc 2017 SRI Annu Meet 2017.

[9] Macdonald J, Corrado P, Nguyen S, Johnson K, Francois C, Reeder S, et al. 4D Flow MRI in the Rhesus Macaque Fetus. Proc 25th Annu ISMRM Meet 2017.

[10] Macdonald J, Corrado P, Nguyen S, Francois C, Reeder S, Bird I, et al. Ferumoxytol MRA in the Pregnant Rhesus Macaque. Proc 25th Annu ISMRM Meet 2017.

[11] Macdonald J, Skopos S, Johnson K, Francois C, Reeder S, Bird I, et al. 4D Flow Imaging of the Placenta and Umbilical Cord in the Rhesus Macaque - Initial Experience. Proc 28th Annu SMRA Meet 2016.

[12] Macdonald J, Corrado P, Nguyen S, Johnson K, Francois C, Magness R, et al. Uteroplacental and Fetal 4D Flow MRI in the Pregnant Rhesus Macaque. J Magn Reson Imaging 2018.

[13] Macdonald J, Forouzan O, Warczytowa J, Wieben O, Chesler NC, Francois CJ. MRI Assessment of Cardiac Function in Response to Exercise. Proc 23rd ISMRM Annu Meet 2015.

[14] Macdonald J, Forouzan O, Warczytowa J, Wieben O, Francois CJ, Chesler NC. MRI assessment of aortic flow and pulse wave velocity in response to exercise. J Cardiovasc Magn Reson 2015;17:M2. doi:10.1186/1532-429X-17-S1-M2.

[15] Macdonald J, Forouzan O, Chesler N, Francois C, Wieben O. MRI assessment of aortic flow in

patients with pulmonary hypertension in response to exercise. Proc 24th Annu ISMRM Meet 2016.

[16] Macdonald J, Beshish A, Haraldsdottir K, Eldridge M, Francois C, Wieben O. 4D Flow Cardiovascular MRI during Exercise. Proc 20th Annu SCMR Sci Sess 2017.

[17] Macdonald J, Roberts G, Wieben O. ECG Characterization and Correction during Exercise Stress Imaging. Proc 26th Annu ISMRM Meet 2018.

[18] Macdonald J, Beshish A, Haraldsdottir K, Wieben O, Eldridge M, Francois C. 4D Flow MRI during Exercise in Prematurely Born Adults and Children. Proc 25th Annu ISMRM Meet 2017.

[19] Macdonald J, Barton G, Beshish A, Goss K, Eldridge M, Francois C, et al. Inefficient Right Heart Function in Preterm Adults as shown with 4D Flow MRI. Proc 26th Annu ISMRM Meet 2018.

[20] Haacke EM, Brown RW, Thompson MR, Venkatesan R. Magnetic Resonance Imaging: Physical Principles and Sequence Design. John Wiley & Sons, Inc; 1999.

[21] Bernstein MA, King KF, Zhou XJ. Handbook of MRI Pulse Sequences. Burlington, MA: Elsevier Academic Press; 2004.

[22] Hashemi RH, Bradley Jr. WG, Lisanti CJ. MRI: The Basics. 2nd ed. Philadelphia, PA: Lippincott Williams & Wilkins; 2004.

[23] Elster AD, Burdette JH. Questions and Answers in Magnetic Resonance Imaging. 2nd ed. Mosby; 2000.

[24] Hanson LG. Is Quantum Mechanics Necessary for Understanding Magnetic Resonance? Concepts Magn Reson 2008;32A. doi:10.1002/cmr.a.

[25] Wright GA. Magnetic resonance imaging. IEEE Signal Process Magizine 1997;14.

[26] Elster AD. Gradient-echo MR imaging: techniques and acronyms. Radiology 1993;186:1–8. doi:10.1148/radiology.186.1.8416546.

[27] Hahn EL. Spin Echoes. Phys Rev 1950;80:580–94. doi:10.1103/PhysRev.80.580.

[28] Edelstein WA, Hutchison JMS, Johnson G, Redpath T. Spin Warp {NMR} Imaging and Applications to Human Whole Body Imaging. Phys Med Biol 1980;25:751.

[29] Glover GH, Pauly JM. Projection Reconstruction Techniques for Reduction of Motion Effects in MRI. Magn Reson Med 1992;28:275–89. doi:10.1002/mrm.1910280209.

[30] Lauterbur PC. Image Formation by Induced Local Interactions. Examples employing nuclear magnetic resonance. 1973. Clin Orthop Relat Res 1985:3–6.

[31] Peters DC, Korosec FR, Grist TM, Block WF, Holden JE, Vigen KK, et al. Undersampled projection reconstruction applied to MR angiography. Magn Reson Med 2000;43:91–101. doi:10.1002/(SICI)1522-2594(200001)43:1<91::AID-MRM11>3.0.CO;2-4.

[32] Mezrich R. A perspective on k-space. Radiology 1995;195.

[33] Jackson JI, Meyer CH, Nishimura DG, Macovski A. Selection of a Convolution Function for Fourier Inversion Using Gridding. IEEE Trans Med Imaging 1991;10:473–8. doi:10.1109/42.97598.

[34] Smith TB, Nayak KS. MRI artifacts and correction strategies. Imaging Med 2010;2:445–57. doi:10.2217/iim.10.33.

[35] Lotz J, Meier C, Leppert A, Galanski M. Cardiovascular Flow Measurement with Phase-Contrast MR Imaging: Basic Facts and Implementation 1. RadioGraphics 2002;22.

[36] Gatehouse PD, Keegan J, Crowe LA, Masood S, Mohiaddin RH, Kreitner KF, et al. Applications of phase-contrast flow and velocity imaging in cardiovascular MRI. Eur Radiol 2005;15:2172–84. doi:10.1007/s00330-005-2829-3.

[37] Atkinson DJ, Edelman RR. Cineangiography of the heart in a single breath hold with a segmented turboFLASH sequence. Radiology 1991;178:357–60. doi:10.1148/radiology.178.2.1987592.

[38] Ibrahim E-SH, Johnson KR, Miller AB, Shaffer JM, White RD. Measuring aortic pulse wave velocity using high-field cardiovascular magnetic resonance: comparison of techniques. J Cardiovasc Magn Reson 2010;12:26. doi:10.1186/1532-429X-12-26.

[39] Johnson KM, Markl M. Improved SNR in phase contrast velocimetry with five-point balanced flow encoding. Magn Reson Med 2010;63:349–55. doi:10.1002/mrm.22202.

[40] Schrauben EM, Anderson AG, Johnson KM, Wieben O. Respiratory-induced venous blood flow effects using flexible retrospective double-gating. J Magn Reson Imaging 2015;42:211–6. doi:10.1002/jmri.24746.

[41] Schnell S, Markl M, Entezari P, Mahadewia RJ, Semaan E, Stankovic Z, et al. K-t GRAPPA accelerated four-dimensional flow MRI in the aorta: Effect on scan time, image quality, and quantification of flow and wall shear stress. Magn Reson Med 2014;72:522–33. doi:10.1002/mrm.24925.

[42] Liu J, Koskas L, Faraji F, Kao E, Wang Y, Haraldsson H, et al. Highly accelerated intracranial 4D flow MRI: evaluation of healthy volunteers and patients with intracranial aneurysms. Magn Reson Mater Physics, Biol Med 2018;31:295–307. doi:10.1007/s10334-017-0646-8.

[43] Gu T, Korosec FR, Block WF, Fain SB, Turk Q, Lum D, et al. PC VIPR: A high-speed 3D phase-contrast method for flow quantification and high-resolution angiography. Am J Neuroradiol 2005;26:743–9. doi:26/4/743 [pii].

[44] Johnson KM, Lum DP, Turski PA, Block WF, Mistretta CA, Ph D, et al. Improved 3D Phase Contrast MRI with Off-resonance Corrected Dual Echo VIPR. Magn Reson Med 2008;60:1329–36. doi:10.1002/mrm.21763.Improved.

[45] Srichai MB, Lim RP, Wong S, Lee VS. Cardiovascular applications of phase-contrast MRI. Am J Roentgenol 2009;192:662–75. doi:10.2214/AJR.07.3744.

[46] Silverman JM, Raissi S, Tyszka JM, Trento a, Herfkens RJ. Phase-contrast cine MR angiography detection of thoracic aortic dissection. Int J Card Imaging 2000;16:461–70.

[47] Vanninen RL, Manninen HI, Partanen PL, Vainio PA, Soimakallio S. Carotid artery stenosis:

clinical efficacy of MR phase-contrast flow quantification as an adjunct to MR angiography. Radiology 1995;194:459–67. doi:10.1148/radiology.194.2.7824727.

[48] Frydrychowicz A, Landgraf BR, Niespodzany E, Verma RW, Roldán-Alzate A, Johnson KM, et al. Four-dimensional velocity mapping of the hepatic and splanchnic vasculature with radial sampling at 3 Tesla: A feasibility study in portal hypertension. J Magn Reson Imaging 2011;34:577–84. doi:10.1002/jmri.22712.

[49] Francois CJ, Lum DP, Johnson KM, Landgraf BR, Bley TA, Reeder SB, et al. Renal Arteries: Isotropic, High-Spatial-Resolution, Unenhanced MR Angiography with Three-dimensional Radial Phase Contrast. Radiology 2011;258.

[50] Francois CJ, Srinivasan S, Schiebler ML, Reeder SB, Niespodzany E, Landgraf BR, et al. 4D cardiovascular magnetic resonance velocity mapping of alterations of right heart flow patterns and main pulmonary artery hemodynamics in tetralogy of Fallot. J Cardiovasc Magn Reson 2012;14:16. doi:10.1186/1532-429X-14-16.

[51] Joseph AA, Merboldt KD, Voit D, Zhang S, Uecker M, Lotz J, et al. Real-time phase-contrast MRI of cardiovascular blood flow using undersampled radial fast low-angle shot and nonlinear inverse reconstruction. NMR Biomed 2012;25:917–24. doi:10.1002/nbm.1812.

[52] Bieging ET, Frydrychowicz A, Wentland A, Landgraf BR, Johnson KM, Wieben O, et al. In vivo three-dimensional mr wall shear stress estimation in ascending aortic dilatation. J Magn Reson Imaging 2011;33:589–97. doi:10.1002/jmri.22485.

[53] Wentland AL, Wieben O, François CJ, Boncyk C, Munoz Del Rio A, Johnson KM, et al. Aortic pulse wave velocity measurements with undersampled 4D flow-sensitive MRI: Comparison with 2D and algorithm determination. J Magn Reson Imaging 2013;37:853–9. doi:10.1002/jmri.23877.

[54] Jeong D, Anagnostopoulos P V., Roldan-Alzate A, Srinivasan S, Schiebler ML, Wieben O, et al. Ventricular kinetic energy may provide a novel noninvasive way to assess ventricular performance in patients with repaired tetralogy of Fallot. J Thorac Cardiovasc Surg 2015;149:1339–47. doi:10.1016/j.jtcvs.2014.11.085.

[55] Eriksson J, Carlhall C, Dyverfeldt P, Engvall J, Bolger A, Ebbers T. Semi-automatic quantification of 4D left ventricular blood flow. J Cardiovasc Magn Reson 2010;12:1–10. doi:10.1186/1532-429X-12-9.

[56] Töger J, Kanski M, Carlsson M, Kovács SJ, Söderlind G, Arheden H, et al. Vortex Ring Formation in the Left Ventricle of the Heart: Analysis by 4D Flow MRI and Lagrangian Coherent Structures. Ann Biomed Eng 2012;40:2652–62. doi:10.1007/s10439-012-0615-3.

[57] Rutkowski DR, Reeder SB, Fernandez LA, Roldan-Alzate A. Surgical planning for living donor liver transplant using 4D flow MRI, computational fluid dynamics and in vitro experiments. Comput Methods Biomech Biomed Engin 2017.

[58] Anavekar NS, Oh JK. Doppler echocardiography: A contemporary review. J Cardiol 2009;54:347–58. doi:10.1016/J.JJCC.2009.10.001.

[59] Dickey RP. Doppler ultrasound investigation of uterine and ovarian blood flow in infertility and early pregnancy. Hum Reprod Update 1997;3:467–503. doi:10.1093/humupd/3.5.467.

[60] Abdallah Y, Naji O, Saso S, Pexsters A, Stalder C, Sur S, et al. Ultrasound assessment of the peri-implantation uterus: A review. Ultrasound Obstet Gynecol 2012;39:612–9. doi:10.1002/uog.10098.

[61] Alfirevic Z, Stampalija T, Gyte GML, Neilson JP. Fetal and umbilical Doppler ultrasound in high-risk pregnancies. Cochrane Database Syst Rev 2009:1–137. doi:10.1002/14651858.CD007529.

[62] Gudmundsson S, Marsal K. Blood Velocity Waveforms in the Fetal Aorta and Umbilical Artery as Predictors of Fetal Outcome: A Comparison. Am J Perinatol 1991;8:1–6.

[63] Gill R. Measurement of blood flow by ultrasound: accuracy and sources of error. Ultrasound Med Biol 1985;11:625–41.

[64] Miller TD. The exercise treadmill test: Estimating cardiovascular prognosis. Cleve Clin J Med 2008;75:424–30. doi:10.3949/ccjm.75.6.424.

[65] Pina IL, Balady GJ, Hanson P, Labovitz AJ, Madonna DW, Myers J. Guidelines for Clinical Exercise Testing Laboratories : A Statement for Healthcare Professionals From the Committee on Exercise and Cardiac Rehabilitation, American Heart Association. Circulation 1995;91:912–21. doi:10.1161/01.CIR.91.3.912.

[66] Bruce R. Exercise testing of patients with coronary heart disease: Principles and normal standards for evaluation. Ann Clin Res 1971;3:323–32.

[67] Fletcher GF, Balady GJ, Amsterdam EA, Chaitman B, Eckel R, Fleg J, et al. Exercise Standards for Testing and Training: A Statement for Healthcare Professionals From the American Heart Association. Circulation 2001;104:1694–740. doi:10.1161/hc3901.095960.

[68] Lang RM, Bierig M, Devereux RB, Flachskampf F a., Foster E, Pellikka P a., et al. Recommendations for chamber quantification: A report from the American Society of Echocardiography's guidelines and standards committee and the Chamber Quantification Writing Group, developed in conjunction with the European Association of Echocardiograph. J Am Soc Echocardiogr 2005;18:1440–63. doi:10.1016/j.echo.2005.10.005.

[69] Armstrong WF, Zoghbi W a. Stress echocardiography: Current methodology and clinical applications. J Am Coll Cardiol 2005;45:1739–47. doi:10.1016/j.jacc.2004.12.078.

[70] Hsiao A, Lustig M, Alley M, Murphy M, Vasanawaia S. Evaluation of Valvular Insufficiency and SHunts with Parallel-imaging Compressed-sensing 4D Phase-contrast MR Imaging. Radiology 2012;265:87–95.

[71] Dilorenzo MP, Bhatt SM, Mercer-Rosa L. How best to assess right ventricular function by echocardiography. Cardiol Young 2015;25:1473–81. doi:10.1017/S1047951115002255.

[72] Gagnon R. Placental insufficiency and its consequences. Eur J Obstet Gynecol Reprod Biol 2003;110:99–107. doi:10.1016/S0301-2115(03)00179-9.

[73] Lang U, Baker RS, Braems G, Zygmunt M, Künzel W, Clark KE. Uterine blood flow--a determinant of fetal growth. Eur J Obstet Gynecol Reprod Biol 2003;110 Suppl:S55–61. doi:10.1016/S0301-2115(03)00173-8.

[74] Bewley S, Cooper D, Campbell S. Doppler investigation of uteroplacental blood flow resistance in the second trimester: a screening study for pre-eclampsia and intrauterine growth retardation. BJOG An Int J Obstet Gynaecol 1991;98:871–9. doi:10.1111/j.1471-0528.1991.tb13508.x.

[75] Goldenberg RL, Culhane JF, Iams JD, Romero R. Epidemiology and causes of preterm birth. Lancet 2008;371:75–84. doi:10.1016/S0140-6736(08)60074-4.

[76] Habara T, Nakatsuka M, Konishi H, Asagiri K, Noguchi S, Kudo T. Elevated blood flow resistance in uterine arteries of women with unexplained recurrent pregnancy loss. Hum Reprod 2002;17:190–4. doi:10.1093/HUMREP/17.1.190.

[77] Guttmacher AE, Maddox YT, Spong CY. The Human Placenta Project: Placental structure, development, and function in real time. Placenta 2014;35:303–4. doi:10.1016/j.placenta.2014.02.012.

[78] Schiff E, Mashiach S. The Use of Low Dose Aspirin in Pregnancy. Am J Reprod Immunol 1992;28:153–6.

[79] Cunningham FG, Leveno K, Bloom SL, Spong CY, Dashe JS, Hoffman BL, et al. Williams Obstetrics. 2014.

[80] Degner K, Magness RR, Shah DM. Establishment of the Human Uteroplacental Circulation: A Historical Perspective. Reprod Sci 2017;24:753–61. doi:10.1177/1933719116669056.

[81] Sourbron SP, Buckley DL. Tracer kinetic modelling in MRI: estimating perfusion and capillary permeability. Phys Med Biol 2011;57:R1–33. doi:10.1088/0031-9155/57/2/R1.

[82] Utz W, Jordan J, Niendorf T, Stoffels M, Luft FC, Dietz R, et al. Blood oxygen level-dependent MRI of tissue oxygenation: Relation to endothelium-dependent and endothelium-independent blood flow changes. Arterioscler Thromb Vasc Biol 2005;25:1408–13. doi:10.1161/01.ATV.0000170131.13683.d7.

[83] Israel GM, Malguria N, McCarthy S, Copel J, Weinreb J. MRI vs. ultrasound for suspected appendicitis during pregnancy. J Magn Reson Imaging 2008;28:428–33. doi:10.1002/jmri.21456.

[84] Patenaude Y, Pugash D, Lim K, Morin L, Bly S, Butt K, et al. The Use of Magnetic Resonance Imaging in the Obstetric Patient. J Obstet Gynaecol Canada 2014;36:349–55. doi:10.1016/S1701-2163(15)30612-5.

[85] Dill T. Contraindications to magnetic resonance imaging. Heart 2008;94:943–8. doi:10.1136/hrt.2007.125039.

[86] Pates JA, Hatab MR, McIntire DD, Cunningham FG, Twickler DM. Determining uterine blood flow in pregnancy with magnetic resonance imaging. Magn Reson Imaging 2010;28:507–10. doi:10.1016/j.mri.2009.12.009.

[87] Hawkes RA, Patterson AJ, Priest AN, Harrison G, Hunter S, Pinney J, et al. Uterine artery pulsatility and resistivity indices in pregnancy: Comparison of MRI and Doppler US. Placenta 2016;43:35–40. doi:10.1016/j.placenta.2016.04.002.

[88] Francois CJ, Srinivasan S, Schiebler ML, Reeder SB, Niespodzany E, Landgraf BR, et al. 4D

cardiovascular magnetic resonance velocity mapping of alterations of right heart flow patterns and main pulmonary artery hemodynamics in tetralogy of Fallot. J Cardiovasc Magn Reson 2012;14:16. doi:10.1186/1532-429X-14-16.

[89] Ansari SA, Schnell S, Carroll T, Vakil P, Hurley MC, Wu C, et al. Intracranial 4D flow MRI: Toward individualized assessment of arteriovenous malformation hemodynamics and treatment-induced changes. Am J Neuroradiol 2013;34:1922–8. doi:10.3174/ajnr.A3537.

[90] Dambaeva S V., Durning M, Rozner AE, Golos TG. Immunophenotype and Cytokine Profiles of Rhesus Monkey CD56bright and CD56dim Decidual Natural Killer Cells. Biol Reprod 2012;86:1–10. doi:10.1095/biolreprod.111.094383.

[91] Golos TG, Bondarenko GI, Dambaeva S V., Breburda EE, Durning M. On the role of placental major histocompatibility complex and decidual leukocytes in implantation and pregnancy success using non-human primate models. Int J Dev Biol 2010;54:431–43. doi:10.1387/ijdb.082797tg.

[92] Silk J, Short J, Roberts J, Kusnitz J. Gestation length in rhesus macaques (Macaca mulatta). Int J Primatol 1993;14:95–104. doi:10.1007/BF02196505.

[93] Dumoulin C, Souza S, Walker M, Wagle W. Three-Dimensional Phase Contrast Angiography. Magn Reson Med 1989;149:139–49.

[94] Johnson KM, Fain SB, Schiebler ML, Nagle S. Optimized 3D ultrashort echo time pulmonary MRI. Magn Reson Med 2013;70:1241–50. doi:10.1002/mrm.24570.

[95] Wehrenberg W, Chaichareon D, Dierschke D, Rankin J, Ginther O. Vascular Dynamics of the Reproductive Tract in the Female Rhesus Monkey: Relative Contributions of Ovarian and Uterine Arteries. Biol Reprod 1977;17:148–53.

[96] Schrauben E, Johnson K, Huston J, del Rio A, Reeder S, Field A, et al. Reproducibility of Cerebrospinal Venous Blood Flow and Vessel Anatomy with the Use of Phase Contrast – Vastly Undersampled Isotropic Projection Reconstruction and Contrast-Enhanced MRA. Am J Neuroradiol 2014;35:999–1006.

[97] Bailey IK, Griffith LS, Rouleau J, Strauss HW, Pitt B. Thallium-201 Myocardial Perfusion Imaging at Rest and during Exercise: Comparative Sensitivity to Electrocardiography in Coronary Artery Disease. Circulation 1977;55:79–87.

[98] Darr C, Paul D, Thomas DP. Effects of age and training status on heart rate recovery after peak exercise 1988:340–3.

[99] Picano E, Pibarot P, Lancellotti P, Monin JL, Bonow RO. The Emerging Role of Exercise Testing and Stress Echocardiography in Valvular Heart Disease. JAC 2009;54:2251–60. doi:10.1016/j.jacc.2009.07.046.

[100] Foster EL, Arnold JW, Jekic M, Bender J, Balasubramanian V, Thavendiranathan P, et al. An MR-Compatible Treadmill for Exercise Stress Cardiac Magnetic Resonance Imaging. Magn Reson Med 2013;67:880–9. doi:10.1002/mrm.23059.An.

[101] Thavendiranathan P, Dickerson J a., Scandling D, Balasubramanian V, Pennell ML, Hinton A, et al. Comparison of treadmill exercise stress cardiac MRI to stress echocardiography in healthy

volunteers for adequacy of left ventricular endocardial wall visualization: A pilot study. J Magn Reson Imaging 2014;39:1146–52. doi:10.1002/jmri.24263.

[102] Globits S, Sakuma H, Shimakawa a, Foo TK, Higgins CB. Measurement of coronary blood flow velocity during handgrip exercise using breath-hold velocity encoded cine magnetic resonance imaging. Am J Cardiol 1997;79:234–7. doi:10.1016/S0002-9149(97)89291-0.

[103] Von Knobelsdorff-Brenkenhoff F, Dieringer M a., Fuchs K, Hezel F, Niendorf T, Schulz-Menger J. Isometric handgrip exercise during cardiovascular magnetic resonance imaging: Set-up and cardiovascular effects. J Magn Reson Imaging 2013;37:1342–50. doi:10.1002/jmri.23924.

[104] Gusso S, Salvador C, Hofman P, Cutfield W, Baldi JC, Taberner A, et al. Design and testing of an MRI-compatible cycle ergometer for non-invasive cardiac assessments during exercise. Biomed Eng Online 2012;11:13. doi:10.1186/1475-925X-11-13.

[105] Forouzan O, Flink E, Warczytowa J, Thate N, Hanske A, Lee T, et al. Low Cost Magnetic Resonance Imaging-Compatible Stepper Exercise Device for Use in Cardiac Stress Tests. J Med Device 2014;8:21–8. doi:10.1115/1.4027343.

[106] Arena R, Lavie CJ, Milani R V, Myers J, Guazzi M. Cardiopulmonary exercise testing in patients with pulmonary arterial hypertension: an evidence-based review. J Heart Lung Transplant 2010;29:159–73. doi:10.1016/j.healun.2009.09.003.

[107] Argiento P, Chesler N, Mule M, D'Alto M, Bossone E, Unger P, et al. Exercise stress echocardiography for the study of the pulmonary circulation. Eur Respir J Off J Eur Soc Clin Respir Physiol 2010;35:1273–8. doi:10.1183/09031936.00076009.

[108] Naeije R, Chesler N. Pulmonary Circulation at Exercise. Compr Physiol 2012;2:711–41. doi:10.1002/cphy.c100091.PULMONARY.

[109] Galie N, Hoeper MM, Humbert M, Torbicki A, Vachiery JL, Barbera JA, et al. Guidelines for the diagnosis and treatment of pulmonary hypertension. Eur Respir J 2009;34:1219–63. doi:10.1183/09031936.00139009.

[110] Reuben SR. Compliance of the Human Pulmonary Arterial System in Disease. Circ Res 1971;29:40–50. doi:10.1161/01.res.29.1.40.

[111] Kiefer TL, Bashore TM. Pulmonary hypertension related to left-sided cardiac pathology 2011;2011. doi:10.1155/2011/381787.

[112] Ungerer RG, Tashkin DP, Furst D, Clements PJ, Gong H, Bein M, et al. Prevalence and Clinical Correlates of Pulmonary Arterial Hypertension in Progressive Systemic Sclerosis. Am J Med 1983;75:65–74.

[113] King ME, Braun H, Goldblatt a, Liberthson R, Weyman a E. Interventricular septal configuration as a predictor of right ventricular systolic hypertension in children: a cross-sectional echocardiographic study. Circulation 1983;68:68–75. doi:10.1161/01.CIR.68.1.68.

[114] Jessup M, Sutton MS, Weber KT, Janicki JS. The effect of chronic pulmonary hypertension on left ventricular size, function, and interventricular septal motion. Am Heart J 1987;113:1114–22. doi:10.1016/0002-8703(87)90921-5.

[115] Roeleveld RJ, Marcus JT, Faes TJC, Gan T-J, Boonstra A, Postmus PE, et al. Interventricular Septal Configuration at MR Imaging and Pulmonary Arterial Pressure in Pulmonary Hypertension. Radiology 2005;234:710–7.

[116] Ley S, Mereles D, Puderbach M, Gruenig E, Schöck H, Eichinger M, et al. Value of MR phase-contrast flow measurements for functional assessment of pulmonary arterial hypertension. Eur Radiol 2007;17:1892–7. doi:10.1007/s00330-006-0559-9.

[117] Jeong D, Schiebler ML, Lai P, Wang K, Vigen KK, Francois CJ. Single breath hold 3D cardiac cine MRI using kat-ARC: preliminary results at 1.5T. Int J Cardiovasc Imaging 2015;31:851–7. doi:10.1007/s10554-015-0615-0.

[118] Laskey WK, Ferrari VA, Palevsky HI, Kussmaul WG. Pulmonary artery hemodynamics in primary pulmonary hypertension. J Am Coll Cardiol 1993;21:406–12. doi:10.1016/0735-1097(93)90682-Q.

[119] Szekanecz Z, Szücs G. Systemic Sclerosis Increased Arterial Stiffness as the Marker of Vascular Involvement in Systemic Sclerosis. J Rheumatol 2008;35:1329–33.

[120] Ergospect. Cardio Step Module n.d. http://ergospect.com/products-detail-ergospect-medical-equipment,pid,3,bid,1285225342,lid,en,eid,1364308426.html (accessed March 28, 2016).

[121] McDowell M, Fryar C, Ogden C, Flegal K. Anthropometric reference data for children and adults: United States, 2003-2006. Natl Health Stat Report 2008:2003–6.

[122] Prec O, Katz L, Sennett L, Rosenman R, Fishman A, Hwang W. Determination of Kinetic Energy of the Heart in Man. Am J Physiol 1949;159:483–91.

[123] Singh B. ECG Artifacts and Poincaré Plot based Heart Rate Variability. Int J Biol Med Res 2016;7:5350–3.

[124] Liu J, Spincemaille P, Codella NCF, Nguyen TD, Prince MR, Wang Y. Respiratory and cardiac self-gated free-breathing cardiac CINE imaging with multiecho 3D hybrid radial SSFP acquisition. Magn Reson Med 2010;63:1230–7. doi:10.1002/mrm.22306.

[125] Dietrich O, Raya JG, Reeder SB, Reiser MF, Schoenberg SO. Measurement of signal-to-noise ratios in MR images: Influence of multichannel coils, parallel imaging, and reconstruction filters. J Magn Reson Imaging 2007;26:375–85. doi:10.1002/jmri.20969.

[126] Stalder AF, Russe MF, Frydrychowicz A, Bock J, Hennig J, Markl M. Quantitative 2D and 3D phase contrast MRI: Optimized analysis of blood flow and vessel wall parameters. Magn Reson Med 2008;60:1218–31. doi:10.1002/mrm.21778.

[127] Hussaini SF, Roldán-Alzate A, Francois CJ. Left and right ventricular kinetic energy using time-resolved versus time-average ventricular volumes. J Cardiovasc Magn Reson 2015;17:1–8. doi:10.1002/jmri.25416.

[128] Spodick DH, Quarry-Pigott VM. Effects of posture on exercise performance: Measurement by systolic time intervals. Circulation 1973;48:74–8. doi:10.1161/01.CIR.48.1.74.

[129] Dyverfeldt P, Ebbers T, Länne T. Pulse wave velocity with 4D flow MRI: Systematic differences

and age-related regional vascular stiffness. Magn Reson Imaging 2014;32:1266–71. doi:10.1016/j.mri.2014.08.021.

[130] Frydrychowicz A, Wieben O, Niespodzany E, Reeder SB, Johnson KM, François CJ. Quantification of Thoracic Blood Flow Using Volumetric Magnetic Resonance Imaging With Radial Velocity Encoding. Invest Radiol 2013;48:819–25. doi:10.1097/RLI.0b013e31829a4f2f.

[131] Hanneman K, Sivagnanam M, Nguyen ET, Wald R, Greiser A, Crean AM, et al. Magnetic Resonance Assessment of Pulmonary (Qp) to Systemic (Qs) Flows Using 4D Phase-contrast Imaging: Pilot Study Comparison with Standard Through-plane 2D Phase-contrast Imaging. Acad Radiol 2014;21:1002–8.

[132] Carlsson M, Töger J, Kanski M, Bloch KM, Ståhlberg F, Heiberg E, et al. Quantification and visualization of cardiovascular 4D velocity mapping accelerated with parallel imaging or k-t BLAST: Head to head comparison and validation at 1.5 T and 3 T. J Cardiovasc Magn Reson 2011;13:1–7. doi:10.1186/1532-429X-13-55.

[133] Westenberg JJM, Roes SD, Ajmone Marsan N, Binnendijk NMJ, Doornbos J, Bax JJ, et al. Mitral Valve and Tricuspid Valve Blood Flow: Accurate Quantification with 3D Velocity-encoded MR Imaging with Retrospective Valve Tracking. Radiology 2008;249:792–800. doi:10.1148/radiol.2492080146.

[134] Carlsson M, Heiberg E, Toger J, Arheden H. Quantification of left and right ventricular kinetic energy using four-dimensional intracardiac magnetic resonance imaging flow measurements. AJP Hear Circ Physiol 2012;302:H893–900. doi:10.1152/ajpheart.00942.2011.

[135] Hussaini SF, Rutkowski DR, Roldan-Alzate A, Francois CJ. Left and right ventricular kinetic energy using time-resolved versus time-average ventricular volumes. J Magn Reson Imaging 2017;45:821–8.

[136] Elbaz MSM, Calkoen EE, Westenberg JJM, Lelieveldt BPF, Roest AAW, van der Geest RJ. Vortex flow during early and late left ventricular filling in normal subjects: quantitative characterization using retrospectively-gated 4D flow cardiovascular magnetic resonance and three-dimensional vortex core analysis. J Cardiovasc Magn Reson 2014;16:78. doi:10.1186/s12968-014-0078-9.

[137] Pasipoularides A, Shu M, Shah A, Womack MS, Glower DD. Diastolic right ventricular filling vortex in normal and volume overload states. Am J Physiol - Hear Circ Physiol 2003;284:H1064–72. doi:10.1152/ajpheart.00804.2002.

[138] Forouzan O, Warczytowa J, Wieben O, François CJ, Chesler NC. Non-invasive measurement using cardiovascular magnetic resonance of changes in pulmonary artery stiffness with exercise. J Cardiovasc Magn Reson 2015;17:109. doi:10.1186/s12968-015-0213-2.

[139] Joseph A, Kowallick JT, Merboldt KD, Voit D, Schaetz S, Zhang S, et al. Real-time flow MRI of the aorta at a resolution of 40 msec. J Magn Reson Imaging 2014;40:206–13. doi:10.1002/jmri.24328.

[140] Nixon PA, Orenstein DM, Kelsey SF, Doershuk CF. The Prognostic Value of Exercise Testing in Patients with Cystic Fibrosis. N Engl J Med 1992;327:1785–8.

[141] Rhodes J, Tikkanen AU, Jenkins KJ. Exercise testing and training in children with congenital heart

disease. Circulation 2010;122:1957–67. doi:10.1161/CIRCULATIONAHA.110.958025.

[142] Reybrouck T, Rogers R, Weymans M, Dumoulin M, Vanhove M, Daenen W, et al. Serial cardiorespiratory exercise testing in patients with congenital heart disease. Eur J Pediatr 1995;154:801–6. doi:10.1007/BF01959785.

[143] Jekic M, Ding Y, Dzwonczyk R, Burns P, Raman S V., Simonetti OP. Magnetic field threshold for accurate electrocardiography in the MRI environment. Magn Reson Med 2010;64:1586–91. doi:10.1002/mrm.22419.

[144] Finley JP, Nugent ST. Heart rate variability in infants, children and young adults. J Auton Nerv Syst 1995;51:103–8. doi:10.1016/0165-1838(94)00117-3.

[145] Krug JW, Rose G. Magnetohydrodynamic distortions of the ECG in different MR scanner configurations. Comput Cardiol 2011:769–72.

[146] Larson AC, White RD, Laub G, McVeigh ER, Li D, Simonetti OP. Self-Gated Cardiac Cine MRI. Magn Reson Med 2004;51:93–102. doi:10.1002/mrm.10664.

[147] Paul J, Divkovic E, Wundrak S, Bernhardt P, Rottbauer W, Neumann H, et al. High-resolution respiratory self-gated golden angle cardiac MRI: Comparison of self-gating Methods in combination with k-T SPARSE SENSE. Magn Reson Med 2015;73:292–8. doi:10.1002/mrm.25102.

[148] Glass H, Costarino A, Stayer S, Brett C, Cladis F, Davis P. Outcomes for extremely premature infants. vol. 120. 2015. doi:10.1213/ANE.0000000000000705.Outcomes.

[149] Tin W, Gupta S. Optimum oxygen therapy in preterm babies. Arch Dis Child Fetal Neonatal Ed 2007;92:143–7. doi:10.1136/adc.2005.092726.

[150] Stenmark KR, Abman SH. Lung Vascular Development: Implications for the Pathogenesis of Bronchopulmonary Dysplasia. Annu Rev Physiol 2005;67:623–61. doi:10.1146/annurev.physiol.67.040403.102229.

[151] Thébaud B, Abman SH. Bronchopulmonary dysplasia: Where have all the vessels gone? Roles of angiogenic growth factors in chronic lung disease. Am J Respir Crit Care Med 2007;175:978–85. doi:10.1164/rccm.200611-1660PP.

[152] Palta M, Sadek-Badawi M, Madden K, Green C. Pulmonary testing using peak flow meters of very low birth weight children born in the perisurfactant era and school controls at age 10 years. Pediatr Pulmonol 2007;42:819–28. doi:10.1002/ppul.20662.

[153] Kerkhof GF, Breukhoven PE, Leunissen RWJ, Willemsen RH, Hokken-Koelega ACS. Does Preterm Birth Influence Cardiovascular Risk in Early Adulthood? J Pediatr 2012;161:390–396.e1. doi:10.1016/J.JPEDS.2012.03.048.

[154] Lewandowski AJ, Bradlow WM, Augustine D, Davis EF, Francis J, Singhal A, et al. Right ventricular systolic dysfunction in young adults born preterm. Circulation 2013;128:713–20. doi:10.1161/CIRCULATIONAHA.113.002583.

[155] Barton G, Beshish A, Macdonald J, Haraldsdottir K, Goss K, Francois C, et al. Adults born preterm exhibit bi-ventricular hypercontractility and inefficiency. FASEB J 2018;32.

[156] Velikina J V, Samsonov A a. Reconstruction of dynamic image series from undersampled MRI data using data-driven model consistency condition (MOCCO). Magn Reson Med 2014;00:1–12. doi:10.1002/mrm.25513.

[157] Jimenez JE, Strigel RM, Johnson KM, Henze Bancroft LC, Reeder SB, Block WF. Feasibility of high spatiotemporal resolution for an abbreviated 3D radial breast MRI protocol. Magn Reson Med 2018:1–15. doi:10.1002/mrm.27137.

[158] Loecher M, Schrauben E, Johnson KM, Wieben O. Phase unwrapping in 4D MR flow with a 4D single-step laplacian algorithm. J Magn Reson Imaging 2016;43:833–42. doi:10.1002/jmri.25045.

[159] Ong F, Uecker M, Tariq U, Hsiao A, Alley MT, Vasanawala SS, et al. Robust 4D flow denoising using divergence-free wavelet transform. Magn Reson Med 2015;73:828–42. doi:10.1002/mrm.25176.

[160] Hanneman K, Kino A, Cheng JY, Alley MT, Vasanawala SS. Assessment of the precision and reproducibility of ventricular volume, function, and mass measurements with ferumoxytol-enhanced 4D flow MRI. J Magn Reson Imaging 2016;44:383–92. doi:10.1002/jmri.25180.